

# **CVD growth control and solar cell application of single-walled carbon nanotubes**

(単層カーボンナノチューブの CVD 合成制御と太陽電池応用)

崔 可航



Doctoral Dissertation

**CVD Growth Control and Solar Cell Application of  
Single-Walled Carbon Nanotubes**

by

**Kehang CUI**

Presented to  
GRADUATE SCHOOL OF ENGINEERING, THE UNIVERSITY OF TOKYO  
in Partial Fulfillment of the Requirements for the Degree of

**Doctoral of Philosophy**  
in the Field of Mechanical Engineering

©2014



# Abstract

Single-walled carbon nanotubes (SWNTs) possess excellent optical, electrical, mechanical and thermal properties as well as chemical stability. Specifically, for the light harvesting application, SWNTs have the superiorities in terms of the wide spectrum of absorption ranging from near-infrared to visible wavelength, high electrical conductivity at high transparency as well as the multiple exciton generation. Combined with earth abundance and chemical stability, the SWNT is supposed to be a very promising candidate for next-generation solar cell applications. However, three main challenges have hindering the full exploitation of SWNTs for the solar cell applications: (1) The SWNTs synthesized on substrates or by floating catalysts have too large diameter. The reduction of the diameter of SWNTs from 2 nm to 1 nm would lead to the increase of the band gap from 0.5 eV to 1.2 eV which is possible for the applications of solar cells. However, this has not been achieved so far and is still a challenge at the nanoscale. (2) The one-dimensional SWNTs do not grow into a three-dimensional bulk like conventional semiconductors. The gap between the properties of SWNT assemblies and the individual SWNTs is the challenge at the microscale. (3) Before the first two challenges are solved, the technique of amounting SWNTs to photovoltaic devices needs further investigation and understanding, which could be categorized into the challenge at the macroscale. This thesis has been trying to answer the challenges of the SWNT for the applications of solar cells at the macroscale, microscale and nanoscale level.

At the macroscale lever, a milestone progress toward the practical application of SWNT/Si solar cell has been realized. This thesis has demonstrated the air-stable SWNT/Si solar cells with power conversion efficiency (PCE) approaching 11% for the first time. The PCE of the solar cell slightly increases after 10-month ambient

exposure. Compared with previously reported results, the fabricated solar cells show a significantly higher stability. The experimental results are well fitted by the  $p-n$  diode equation model, and the mechanisms of the improved performance of the SWNT/Si solar cells are discussed accordingly. The full exploitation of the superior electrical, optical and chemical properties of SWNTs is very promising for the next-generation photovoltaic devices.

At the microscale lever, this thesis has proposed and realized self-assembled micro-honeycomb networks of SWNTs for solar cells for the first time. The hierarchical micro-honeycomb consists of dense walls and a buckypaper bottom, which simultaneously increases the optical transmittance and decreases the sheet resistance. The microhoneycomb structure is formed by the breath figure mechanism. Applying  $\mu$ -HN to the SWNT-Si solar cell results in both high PCE and high fill factor. Note that the achieved PCE is obtained with only 35.0% transparency and without any efforts made to optimize the SWNT chirality, diameter or length. We believe the hierarchical  $\mu$ -HN is very promising for applications of SWNT-Si solar cells.

At the nanoscale level, we have grown the SWNTs with sub-nm diameter directly on the substrate for the first time by using the Co/Cu bimetallic catalysts. At the temperature of 650 °C, the as-synthesized SWNTs have very high quality with the major chirality of (6,5) and (7,5), which makes the average diameter of SWNTs only 0.8 nm. The direct application of the SWNTs with such a narrowly-distributed small diameter to solar cells is expected to have very promising performance.

# Publications Resulting from this Research

## (a) Peer-Reviewed Journals

- 1 Kehang Cui et al, “Growth of Vertically-Aligned Single-Walled Carbon Nanotubes with sub-nm Diameter on Substrates”, in preparation
- 2 Kehang Cui et al, “Three-Dimensional Single-Walled Carbon Nanotube Architecture by Breath Figure”, in preparation
- 3 Kehang Cui and S. Maruyama, “Carbon Nanotube-Si Heterojunction Solar Cells” *Journal of Materials Chemistry A (Invited Feature Article)*, in preparation
- 4 Kehang Cui, A. Anisimov, T. Chiba, S. Fujii, H. Kataura, A. Nasibulin, S. Chiashi, E. Kauppinen and S. Maruyama, “Air-Stable High-Efficiency Solar Cells Using Dry-Transferred Single-Walled Carbon Nanotube Films”, *Journal of Materials Chemistry A*, 2014, 2, 11311-11318
- 5 Kehang Cui, T. Chiba, X. Chen, S. Chiashi and S. Maruyama, “Structured Single-Walled Carbon Nanotube and Graphene for Solar Cells”, *Journal of Nanoscience and Nanotechnology*, 2014, accepted, in press
- 6 Kehang Cui, T. Chiba, S. Omiya, P. Zhao, T. Thurakitserree, S. Fujii, H. Kataura, S. Chiashi and S. Maruyama, “Self-Assembled Microhoneycomb Network of Single-Walled Carbon Nanotubes for Solar Cells”, *Journal of Physical Chemistry Letters*, 2013, 4, 2571-2576 (**ISI Cited Times: 7**)

## (b) Patent

S. Maruyama, Kehang Cui and S. Chiashi, “Method for fabricating Honeycomb Networked Single-Walled Carbon Nanotube Films and Honeycomb Networked Single-Walled Carbon Nanotube Films”, approved by The University of Tokyo

## (c) Plenary, Keynote and Invited Speeches at International Conferences

- 1 (**Plenary**) S. Maruyama, Kehang Cui, T. Chiba, S. Chiashi, “Carbon Nanotube-Si Heterojunction Solar Cells”, **The 8<sup>th</sup> US-Japan Joint Conference on Nanoscale Transport Phenomena: Science and Engineering**, Santa Cruz, CA, USA, July 13-16, 2014
- 2 (**Invited**) S. Maruyama, Kehang Cui, T. Chiba, O. Reynaud, S. Fujii, A. Nasibulin, S. Chiashi, H.

- Kataura and E. Kauppinen, “*Heterojunction Solar Cell with Structured Single-Walled Carbon Nanotubes*”, **The 225<sup>th</sup> Electrochemistry Society Meeting**, Orlando, FL, USA, May 11-16, 2014
- 3 **(Keynote)** S. Maruyama, Kehang Cui, E. Einarsson and S. Chiashi, "*Self-Assembled Micro-Honeycomb Network of Single-Walled Carbon Nanotubes for Heterojunction Solar Cells*", **The 5<sup>th</sup> International Conference on Nanoscience & Technology**, Beijing, China, Sept. 5-7, 2013
  - 4 **(Invited)** S. Maruyama, Kehang Cui, T. Chiba, E. Einarsson and S. Chiashi, "*Self-Organized Micro-Honeycomb Network Structure of Single-Walled Carbon Nanotubes for Photovoltaic Devices*", **ASME 2013 Summer Heat Transfer Conference**, Minneapolis, USA, July 14-19, 2013
  - 5 **(Invited)** Kehang Cui, T. Chiba, T. Thurakitseree, X. Chen, H. Kinoshita, P. Zhao, T. Inoue, E. Einarsson, S. Chiashi and S. Maruyama, "*Structured SWNTs and Graphene for Photovoltaic devices*", **The 5<sup>th</sup> Workshop on Nanotube Optics and Nanospectroscopy (WONTON)**, Los Alamos National Laboratory, USA, June 16-20, 2013
  - 6 **(Invited)** Kehang Cui, T. Chiba, H. Kinoshita, P. Zhao, T. Thurakitseree, T. Inoue, E. Einarsson, S. Chiashi and S. Maruyama, "*Micro-Honeycomb Network Structure of SWNTs for Heterojunction Solar Cell*", **The 223<sup>rd</sup> Electrochemistry Society Meeting**, Toronto, Canada, May 12-16, 2013
  - 7 **(Invited)** S. Maruyama, Kehang Cui, T. Chiba, E. Einarsson and S. Chiashi, "*CVD Growth of Self-Organized Micro-Honeycomb Network Structure of Single-Walled Carbon Nanotubes for Photovoltaic Devices*", **The 27<sup>th</sup> International Winterschool on Electronic Properties of Novel Materials (IWEPM 2013)**, Kirchberg in Tirol, Austria, March 3-9, 2013

#### **(d) Contributed Talks at International Conferences**

- 1 S. Maruyama, Kehang Cui, T. Chiba, H. An, R. Xiang, S. Chiashi, Y. Matsuo, A. G. Nasibulin, E. I. Kauppinen, “*Controlled CVD Growth and Solar Cell Applications of Single-Walled Carbon Nanotubes*”, **Materials Research Society Fall Meeting and Exhibition 2014**, Boston, MA, USA, Nov. 30 – Dec. 5, 2014
- 2 Kehang Cui, R. Xiang, S. Chiashi, S. Maruyama, “*Tuning Microstructure and Nanostructure of Single-Walled Carbon Nanotubes for Solar Cells Applications*”, **The 3<sup>rd</sup> JSAP-OSA Joint Symposia**, Sapporo, Hokkaido, Japan, Sept. 16-20, 2014
- 3 Kehang Cui, T. Chiba, S. Chiashi, E. Kauppinen and S. Maruyama, “*Single-Walled Carbon Nanotubes for Heterojunction Solar Cells*”, **The 15<sup>th</sup> International Heat Transfer Conference**, Kyoto, Japan, August 11-14, 2014
- 4 S. Maruyama, Kehang Cui, S. Chiashi, A. G. Nasibulin, E. I. Kauppinen, “*Controlled Growth of Single-Walled Carbon Nanotubes and Application to CNT-Si Solar Cells*”, **The 15<sup>th</sup> International Conference on the Science and Application of Nanotubes (NT14)**, Los Angeles, CA, USA, June 2<sup>nd</sup> – 6<sup>th</sup> 2014



- 5 Kehang Cui, T. Chiba, E. Einarsson, S. Chiashi and S. Maruyama, “*Self-Assembled Micro-honeycomb Network of Single-Walled Carbon Nanotubes for Heterojunction Solar Cells*”, **JSAP-MRS Joint Symposia**, Kyoto, Japan, September 16-20, 2013
- 6 Kehang Cui, T. Chiba, X. Chen, S. Chiashi and S. Maruyama, “*Structured SWNTs and Graphene for Solar Cells*”, **The 4<sup>th</sup> International Symposium on Micro and Nano Technology**, Shanghai, China, October 8-12, 2013
- 7 S. Maruyama, Kehang Cui, T. Chiba, E. Einarsson and S. Chiashi, “*Self-Assembled Micro-Honeycomb Network of Single-Walled Carbon Nanotubes for Heterojunction Solar Cell*”, **The 14<sup>th</sup> International Conference on the Science and Application of Nanotubes (NT13)**, Espoo, Finland, and **The 1<sup>st</sup> Carbon Nanotube Thin Film Applications Symposium**, Tallinn, Estonia, June 23-29, 2013
- 8 Kehang Cui, S. Omiya, P. Zhao, S. Aikawa, S. Chiashi and S. Maruyama, “*Single-Walled Carbon Nanotube/Silicon Heterojunction Photovoltaic Cells*”, **Materials Research Society 2012 Fall Meetings**, Boston, MA, USA, November 25-December 1, 2012
- 9 Kehang Cui, S. Omiya, P. Zhao, S. Chiashi and S. Maruyama, “*Optimization of Single-Walled Carbon Nanotube/Silicon Heterojunction Solar Cells*”, **JSAP-OSA Joint Symposia**, Matsuyama, Japan, September 11-14, 2012
- 10 Kehang Cui, K. Ishikawa, T. Thurakiseree, J. Shiomi and S. Maruyama, “*Thermal Conduction and Thermoelectrics of Nitrogen-doped Single-Walled Carbon Nanotubes*”, **2012 GMSI International Workshop on Numerical Simulation of Fluid/Thermal Systems**, Stockholm, Sweden and Delft, The Netherland, March, 2012

### (e) Poster Presentations at International Conferences

- 1 Kehang Cui, S. Chiashi, E. I. Kauppinen, S. Maruyama, “*Single-Walled Carbon Nanotubes for Solar Cells*,” **The 28<sup>th</sup> International Winterschool on Electronic Materials of Novel Materials**, Kirchberg in Tirol, Austria, March 8-15, 2014
- 2 Kehang Cui, T. Chiba, S. Chiashi, E. I. Kauppinen, S. Maruyama, “*Single-Walled Carbon Nanotube Assemblies for Photovoltaic Devices*,” **The 4<sup>th</sup> A3 Symposium on Emerging Materials: Nanomaterial for Energy and Electronics**, Jeju Island, Korea, November 10-14, 2013
- 3 Kehang Cui, O. Reynaud, T. Chiba, E. Einarsson, A. G. Nasibulin, S. Chiashi, E. I. Kauppinen, S. Maruyama, “*Air-Stable High-Efficiency Nanotube-Si Heterojunction Solar Cells*”, **The 45<sup>th</sup> Fullerene, Nanotube and Graphene General Symposium**, Osaka, Japan, August 5-7, 2013
- 4 Kehang Cui, T. Chiba, E. Einarsson, S. Chiashi, S. Maruyama, “*Self-Assembled Micro-Honeycomb Network of Single-Walled Carbon Nanotubes for Heterojunction Solar Cells*”, **The 14th International Conference on the Science and**

**Application of Nanotubes (NT13)**, Espoo, Finland, June 24-28, 2013, and **The 7<sup>th</sup> International Workshop on Metrology, Standardization and Industrial Quality of Nanotubes (MSIN13)**, Tallinn, Estonia, June 29, 2013

- 5 Kehang Cui, E. Einarsson, S. Chiashi, S. Maruyama,  
"Self-Assembled Micro-Honeycomb Network of Single-Walled Carbon Nanotubes for Solar Cells,"  
**International Conference on Frontiers of Nanochemistry**, Beijing, China, June 6-7, 2013
- 6 Kehang Cui, S. Yamanaka, S. Omiya, S. Chiashi, S. Maruyama, "Single-Walled Carbon Nanotubes as Building Blocks for Solar Energy Conversion", **The 4<sup>th</sup> GMSI International Symposium**, Tokyo, Japan, March 2, 2012

# Contents

<b>Abstract .....</b>	<b>i</b>
<b>Publications Resulting from this Research.....</b>	<b>iii</b>
(a) Peer-Reviewed Journals .....	iii
(b) Patent .....	iii
(c) Plenary, Keynote and Invited Speeches at International Conferences.....	iii
(d) Contributed Talks at International Conferences .....	iv
(e) Poster Presentations at International Conferences .....	v
<b>Contents.....</b>	<b>vii</b>
<b>List of Figures .....</b>	<b>xi</b>
<b>List of Tables .....</b>	<b>xvii</b>
<b>Nomenclature .....</b>	<b>xix</b>
<b>Preface .....</b>	<b>1</b>
<b>Chapter 1 Introduction.....</b>	<b>5</b>
1.1 Physics of Carbon Nanotubes .....	6
1.1.1 Atomic Structure of Graphene and SWNTs.....	6
1.1.2 Structure-Related Properties of Graphene and SWNTs.....	10
1.2 Metrology of Carbon Nanotubes.....	13
1.2.1 Electron Microscopy .....	14
1.2.2 Raman Spectroscopy.....	15
1.2.3 UV-vis-NIR Absorption Spectroscopy.....	18
1.2.4 Optical and Electrical Properties of SWNT Assemblies .....	20
<b>Chapter 2 Motivation, Challenges and Organization of the Thesis.....</b>	<b>23</b>
2.1 What Does SWNT Have to Do with Solar Cells .....	23
2.2 Challenges of Applying Carbon Nanotubes in Solar Cells .....	25
2.3 Organization of the Thesis .....	26

**Chapter 3 High-Efficiency Air-Stable SWNT-Silicon Heterojunction Solar Cells 27**

3.1 Research Background and Literature Review ..... 27

3.2 Materials and Methods ..... 29

    3.2.1 Synthesis of SWNT Films ..... 29

    3.2.2 Fabrication of SWNT/Si Solar Cells..... 29

3.3 Air-Stable SWNT/Si Solar Cells with Record-High Efficiency ..... 33

    3.3.1 Current Density-Voltage Characteristics ..... 33

    3.3.2 Characterization of Stability in the Ambient Environment..... 35

    3.3.3 Performance Fluctuation of the Solar Cells Fabricated in Different Batches..... 37

3.4 Mechanism Discussion of High-Efficiency SWNT/Si Solar Cells..... 38

    3.4.1 Impact of Light Intensity: Experiment and Modeling ..... 38

    3.4.2 Impact of Interfacial Oxide Layer..... 42

3.5 Summary..... 46

**Chapter 4 Microstructure Control of SWNTs for Solar Cell Applications..... 47**

4.1 Research Background and Literature Review ..... 49

4.2 Self-Assembly of Vertically Aligned SWNTs ..... 51

    4.2.1 CVD Growth of Vertically Aligned SWNTs ..... 51

    4.2.2 Formation of Micro-Honeycomb Networked SWNT Film..... 53

    4.2.3 Cell Size Control of the Micro-Honeycomb Networked SWNT Film ..... 53

    4.2.4 Breath Figure Mechanism of the Micro-Honeycomb Network ..... 59

4.3 Spectroscopy Characterization of Micro-Honeycomb Networked SWNT Film..... 62

    4.3.1 Raman Spectroscopy of the Micro-Honeycomb Networked SWNT Film ..... 62

    4.3.2 UV-vis-NIR Spectroscopy of the Micro-Honeycomb Networked SWNT Film ..... 64

4.4 Micro-Honeycomb Networked SWNT Film for Solar Cells ..... 66

    4.4.1 Performance Characterization of Pristine SWNT/Si Solar Cells ..... 66

    4.4.2 Performance Characterization of Acid-Doped SWNT/Si Solar Cells ..... 72

    4.4.3 Wavelength dependence of photocurrent generation ..... 73

4.5 Mechanism of Performance Improvement by Micro-Honeycomb Network..... 74

4.6 Summary..... 77

**Chapter 5 CVD Controlled Growth of SWNT films for Solar Cell Applications 79**

5.1 State of the Art of CVD Growth Control of SWNTs..... 80

5.2 Literature Review..... 84

    5.2.1 Alcohol Catalytic Chemical Vapor Deposition..... 84

    5.2.2 CVD Growth on Cu-based Catalysts ..... 87

5.3 Synthesis of Sub-Nanometer-Diameter SWNT Films directly on Surface ..... 88

5.3.1 Experimental Design.....	88
5.3.2 Low-Temperature ACCVD Synthesis of SWNTs with sub-nm Diameter .....	90
5.4 Exploration of Thermodynamic Parameters for CVD Growth Control.....	94
5.4.1 Effect of Temperature on Chiral Distribution of SWNTs.....	94
5.4.2 Effect of Pressure on Chiral Distribution of SWNTs .....	96
5.4.3 Effect of CVD Time on the Yield of SWNTs.....	99
5.5 Summary .....	106
<b>Chapter 6 Conclusions .....</b>	<b>107</b>
6.1 Contributions to the Research of SWNTs at Macroscale Level .....	108
6.2 Contributions to the Research of SWNTs at Microscale Level.....	110
6.3 Contributions to the Research of SWNTs at Nanoscale Level.....	111
6.4 Summary .....	112
<b>Bibliography .....</b>	<b>113</b>
<b>Acknowledgement.....</b>	<b>123</b>
<b>Curriculum Vitae.....</b>	<b>125</b>



# List of Figures

<i>Figure 0- 1 The variety of carbon allotropes: diamond and graphite are 3-dimensional; graphene, carbon nanotubes and fullerene are two-, one- and zero-dimensional, respectively. This artwork is adopted from the website of this laboratory: Shigeo Maruyama’s Carbon Nanotube Site – <a href="http://photon.t.u-tokyo.ac.jp">http://photon.t.u-tokyo.ac.jp</a> .....</i>	<i>3</i>
<i>Figure 0- 2 Number of papers published and indexed by Web of Science as of March 2014. Key words: (carbon nanotube*).....</i>	<i>3</i>
<i>Figure 1- 1 Unit cell of graphene in (a) real space, with the red line rhombus showing unit cell, and (b) momentum space, with the shaded hexagon showing the Brillouin zone and red dashed line showing the symmetry point.....</i>	<i>7</i>
<i>Figure 1- 2 The chiral vector <math>C_h</math> for an <math>(n,m) = (4,2)</math> SWNT. The chiral angle is shown by <math>\theta</math> .....</i>	<i>9</i>
<i>Figure 1- 3 The Brillouin zone of a <math>(4,2)</math> SWNT in the reciprocal lattice. ....</i>	<i>10</i>
<i>Figure 1- 4 (a) Three-dimensional band structure of graphene. Adoped with permission from Prof. Shigeo Maruyama’s Carbon Nanotube Site (b) Three-dimensional band structure of SWNT. Reprinted from [8], Copyright 2005, with permission from Elsevier.....</i>	<i>11</i>
<i>Figure 1- 5 Electronic density of states of SWNTs with different chiralities. From top to bottom: <math>(4,2)</math> SWNT, <math>(6,5)</math> SWNT and <math>(10,10)</math> SWNT. Data source from <a href="http://www.photon.t.u-tokyo.ac.jp">www.photon.t.u-tokyo.ac.jp</a>..</i>	<i>12</i>
<i>Figure 1- 6 SWNT <math>(n,m)</math> indices. Here, a red solid point represents metallic nanotube and a black open circle represents semiconductor nanotubes. The condition for the metallic nanotube is: <math>2n+m=3q</math> (<math>q</math>: integer), or <math>(n-m)/3</math> is integer. This artwork is adopted from the website of this laboratory: Prof. Shigeo Maruyama’s Carbon Nanotube Site – <a href="http://photon.t.u-tokyo.ac.jp">http://photon.t.u-tokyo.ac.jp</a>.....</i>	<i>13</i>
<i>Figure 1- 7 Typical SEM images of vertical-aligned SWNTs synthesized by the ACCVD method with Co and Mo as catalyts.....</i>	<i>14</i>
<i>Figure 1- 8 Typical TEM images of high-quality SWNTs synthesized by ACCVD method with Fe and Co as catalyts. Reprinted from [7], Copyright (2002), with permission from Elsevier.....</i>	<i>15</i>
<i>Figure 1- 9 A typical Raman spectrum of SWNTs synthesized by ACCVD method.....</i>	<i>16</i>
<i>Figure 1- 10 Kataura plot of single-walled carbon nanotubes with laser excitation energy.....</i>	<i>17</i>
<i>Figure 1- 11 Position of G- and the separation of G+ and G- for SWNT of different chiralities: the G-Kataura plot. Reprinted with permission from [9]. Copyright (2012) American Chemical Society.....</i>	<i>17</i>

<i>Figure 1- 12 (a) Schematic of the measurement of absorption of SWNT solution. (b) Absorption spectrum of CoMoCAT SWNT dispersion in water.....</i>	<i>19</i>
<i>Figure 1- 13 (a) Schematic of the measurement of absorption of as-synthesized SWNT on quartz. (b) Absorption spectrum of as-synthesized SWNTs by ACCVD method. ....</i>	<i>19</i>
<i>Figure 1- 14 Four-point probe measurement. (a) Resistance at the contact between the probe and material. (b) Schematic of four-point probe setup. (c) Schematic of van de Pauw four-point measurement for random-shaped thin film.....</i>	<i>20</i>
<i>Figure 1- 15 Transmittance spectra of vertically aligned SWNT (VA-SWNT) films with different thicknesses. ....</i>	<i>21</i>
<i>Figure 2- 1 Schematic of tandem solar cell.....</i>	<i>24</i>
<i>Figure 2- 2 The ultimate architecture of tandem SWNT solar cells. ....</i>	<i>25</i>
<i>Figure 3- 1 (a) An SWNT film on the fused quartz substrate after the dry-transfer process. (b) The SEM images at the low and high magnifications of the SWNT film from (a). (c) Raman spectra of the SWNT film under the laser excitation with the wavelength of 488 nm, 532 nm, 633 nm and 785 nm. (d) Transmission spectra of the TCF70, TCF80 and TCF90 SWNT films over the wavelength range of 200 nm to 3200 nm, with AM1.5G irradiance spectrum.....</i>	<i>31</i>
<i>Figure 3- 2 (a) Fabrication process of the n-type Si substrate for the SWNT/Si solar cell. (b) Schematic of the SWNT/Si solar cell with dimensional parameters. (c) Magnified SEM image of contact window edge of the SWNT/Si solar cell. A region of the SWNT film with the width of 300 nm was suspended between the Si substrate and the Pt electrode. ....</i>	<i>32</i>
<i>Figure 3- 3 (a) Representative J-V characteristics of the SWNT/Si solar cells with the TCF70, TCF80 and TCF90 films under 100 mW/cm<sup>2</sup> AM1.5G illumination. (b) J-V characteristics of the SWNT/Si solar cells under the dark condition. (c) Reproducibility of J-V characteristics of four solar cell samples with the TCF80 films fabricated in the same batch. ....</i>	<i>34</i>
<i>Figure 3- 4 (a) J-V characteristics of the SWNT/Si solar cell using TCF90 film measured immediately as well as after 1, 6 and 10 months exposed in the ambient condition. (b) The changes of PCE and Voc values of the SWNT/Si solar cell using TCF90 film during 10-month ambient exposure.....</i>	<i>36</i>
<i>Figure 3- 5 Resonance Raman spectra of the as-synthesized SWNTs and the SWNTs exposed in air for six months: (a) RBM and (b) G band and D band. The inset of (b) shows the normalized G band. All spectra were measured with a 488 nm excitation laser incident normal to the substrate.....</i>	<i>37</i>
<i>Figure 3- 6 More than two hundred J-V curves of the SWNT/Si solar cell samples fabricated in different batches. ....</i>	<i>38</i>
<i>Figure 3- 7 (a) The dependency of open-circuit voltage on light intensity. The line is the modeling result of this dependency. The inset is the equivalent circuit of the SWNT/Si solar cells.</i>	



<p>(b) <i>J-V characteristics of the SWNT/Si solar cells under different light intensities. The symbols denote the experimental results, while the lines represent the modeling results by the p-n diode equation. (c) The curve fitting of the J-V characteristics of the SWNT/Si solar cells using the TCF70, TCF80 and TCF90 films. (d) Hysteresis of the forward and reverse scans for the OxideTCF70 and TCF70 samples which respectively have the oxide layers with the thicknesses of around 15 Å and 7 Å between the SWNT film and Si substrate.....</i></p>	41
<p><b>Figure 3- 8 Possible mechanisms for the SWNT-Si solar cell: (a) metallic SWNTs and (b) semiconducting SWNTs. ....</b></p>	44
<p><b>Figure 3- 9 X-ray photoelectron spectrum of the Si substrate used in the SWNT/Si solar cell. ....</b></p>	45
<p><b>Figure 4- 1 SEM image of self-assembled polymeric nanobristle by evaporating liquid. From Ref. [52]. Reprinted with permission from AAAS.....</b></p>	49
<p><b>Figure 4- 2 Mechanism and SEM images of self-assembled multiwalled carbon nanotubes induced by capillary forces. Copyright © 2010 WILEY-VCH Verlag GmbH &amp; Co. KGaA, Weinheim. ....</b></p>	50
<p><b>Figure 4- 3 SEM image (a) and mechanism (b) of collapsing VA-SWNTs induced by capillary forces. Reprinted by permission from Macmillan Publishers Ltd: Nature Materials [57], copyright (2006) .....</b></p>	50
<p><b>Figure 4- 4 Protocol of CVD growth of vertically aligned SWNTs from alcohol on substrate. ....</b></p>	52
<p><b>Figure 4- 5 (a) Growth curve of the VA-SWNTs in the ACCVD process by the in-situ laser absorption technique. (b) SEM image of the corresponding VA-SWNTs.....</b></p>	52
<p><b>Figure 4- 6 (a) The schematic of the water vapor treatment. (b) The schematic of the as-synthesized uniform VA-SWNT array before water vapor treatment. (c) The schematic of the stable <math>\mu</math>-HN formed after 20 ~ 30 iterations of the water vapor treatment. (d) The SEM image of a dense SWNT wall of an individual honeycomb cell. (e)The magnified image of the three-dimensional hierarchical <math>\mu</math>-HN with dense SWNT wall and randomly oriented bottom. ....</b></p>	55
<p><b>Figure 4- 7 Water vapor treatment of the VA-SWNT array into a <math>\mu</math>-HN. (a) Schematic of the water vapor treatment process. (b) As-synthesized high-quality VA-SWNT with a uniform top surface. (c) Intermediate stage of the <math>\mu</math>-HN formation after the first iteration. (d) Stable <math>\mu</math>-HN formed after 30 times iteration of the water vapor treatment. ....</b></p>	56
<p><b>Figure 4- 8 100 <math>\mu</math>m-scale gaps obtained by applying a 10 <math>\mu</math>L water droplet to the surface at RT under (a) low magnification and (b) high magnification.....</b></p>	56
<p><b>Figure 4- 9 (a-c) Morphologies obtained by exposure to 50 °C, 70 °C and 80 °C water reservoirs, respectively. The vapor exposure time for each vapor treatment step is 5 s.....</b></p>	57
<p><b>Figure 4- 10 (a-c) Morphologies obtained with vapor exposure times of 2 s, 5 s and 15 s for each</b></p>	

iteration, respectively. Reservoir temperature was 80 °C. ....	58
Figure 4- 11 Flow chart of ex-situ SEM observation of the honeycomb formation process. ....	59
Figure 4- 12 ex-situ observation of the evolution of the honeycomb structure formation. The left-hand side is the morphology of SWNTs after the first repeat of water vapor treatment and the right-hand side is the morphology of the SWNTs after the second repeat of water vapor treatment.....	59
Figure 4- 13 ex-situ observation of the evolution of the honeycomb structure formation. The left-hand side is the morphology of SWNTs after the four-time repeat of water vapor treatment and the right-hand side is the morphology of the SWNTs after the eight-time repeat of water vapor treatment. ....	60
Figure 4- 14 The captured stochastic process of the formation of microhoneycomb structure, which is resulted from the capillary force of water vapor.....	60
Figure 4- 15 Magnified SEM image of the hexagonal structure of SWNTs formed by water vapor treatment. ....	60
Figure 4- 16 Resonance Raman spectra of SWNTs before and after water vapor treatment: spectrum 1 corresponds to as-synthesized VA-SWNTs. Spectra 2 and 3 correspond to the wall and bottom of the micro-honeycomb structure, respectively. All spectra were measured with a 488 nm excitation laser incident normal to the substrate. ....	63
Figure 4- 17 Raman spectra of pristine and nitric acid treated samples. Spectra of the treated samples were measured immediately after the samples were completely dried.....	63
Figure 4- 18 (a) UV-vis-NIR absorption spectra of pristine and nitric acid doped SWNTs with micro-honeycomb networked structure. (b) UV-vis-NIR absorption spectra of pristine and nitric acid doped random-oriented SWNTs. ....	64
Figure 4- 19 UV-vis-NIR absorption spectra of pristine VASWNT and its change after different times of nitric acid treatment. The absorption spectrum of VASWNT is restored after DI water and IPA rinse followed by Ar anneal. ....	65
Figure 4- 20 Absorption spectra measured at different gate voltage for (a) metallic SWNTs and (b) semiconducting SWNTs. © 2014 WILEY-VCH Verlag GmbH & Co. KGaA, Weinheim...	65
Figure 4- 21 Transfer process of the self-assembled SWNT films onto the Si substrate for the fabrication of SWNT-Si solar cells and schematic of the fabricated solar cell.....	67
Figure 4- 22 Photos of fabricated SWNT-Si solar cells. The left one has microhoneycomb networked SWNT film on top and the right one has random-oriented SWNT film on top. ....	67
Figure 4- 23 (a) Schematic of SWNT-Si solar cell. (b-d) Three selected assemblies for the fabrication of solar cells and the photovoltaic performance of the fabricated solar cells. (b) $\mu$ -HN. (c) Collapsed HN. (d) Porous HN. (e) J-V characteristics of SWNT-Si solar cells with $\mu$ -HN, collapsed HN and porous HN measured under AM1.5G 100mW/cm <sup>2</sup> . The dashed line and solid line denote the J-V curve of the solar cells within three hours (immediate) and after	

<i>three weeks after fabrication, respectively.....</i>	68
<i>Figure 4- 24 (a) J-V characteristics of a micro-honeycomb structured SWNT-Si solar cell measured three hours and 21 days after device fabrication (shown in red), as well as 1 h and 12 h after dilute nitric acid doping (shown in green). (b) UV-vis-NIR transmittance spectra of <math>\mu</math>-HN, collapsed HN and porous HN for pristine (solid) and doped (dashed) conditions (left y axis) with AM1.5G spectrum (right y axis). (c) Sheet resistance of <math>\mu</math>-HN, collapsed HN and porous HN structures before and after acid doping. ....</i>	69
<i>Figure 4- 25 SEM images the <math>\mu</math>-HN after acid doping. (a) Long-range morphology. (b) Magnified image of the wall in the <math>\mu</math>-HN. ....</i>	72
<i>Figure 4- 26 External quantum efficiency of the SWNT-Si solar cell and Si solar cell (left y axis), as well as the absorption spectrum of the SWNT therein (right y axis) .....</i>	73
<i>Figure 4- 27 (a) J-V characteristics of the SWNT-Si solar cells with the <math>\mu</math>-HN, collapsed HN and porous HN SWNT films measured under dark and light conditions. (b) J-V characteristics of the SWNT-Si solar cells with the pristine <math>\mu</math>-HN, doped <math>\mu</math>-HN and pristine TCF90 films measured under dark and light conditions.....</i>	75
<i>Figure 4- 28 Experimental and modeling results of the J-V characteristics of the SWNT-Si solar cells with the pristine <math>\mu</math>-HN, the doped <math>\mu</math>-HN and the pristine TCF90 films. ....</i>	75
<i>Figure 4- 29 The relationship between the <math>R_s</math> and FF of the eleven solar cell samples: pristine and doped <math>\mu</math>-HN, collapsed HN, porous HN, four ill-formed honeycomb networked SWNT films and randomly oriented SWNT films with 70% (TCF70), 80% (TCF80) and 90% (TCF90) transparency.....</i>	76
<i>Figure 5- 1 Absorption spectrum of dispersed commercial CoMoCAT SWNT (left) and commercial ACCVD SWNT samples.....</i>	83
<i>Figure 5- 2 SEM image of the cross-sectional view of the as-synthesized VA-SWNT mat by ACCVD process. The 2 min CVD process yield 12 <math>\mu</math>m-thick VA-SWNT mat. ....</i>	85
<i>Figure 5- 3 Raman spectroscopy of the as-synthesized VA-SWNT mat by ACCVD proces. (a) RBM and (b) G band and D band. ....</i>	86
<i>Figure 5- 4 Comparison of Raman spectra of SWNTs synthesized from Co/Cu and Co/Mo at different temperatures. The laser excitation energy is 2.54 eV.....</i>	91
<i>Figure 5- 5 Comparison of Raman spectra of SWNTs synthesized from Co/Cu and Co/Mo at different temperatures. The laser excitation energy is 2.33 eV.....</i>	91
<i>Figure 5- 6 Comparison of Raman spectra of SWNTs synthesized from Co/Cu and Co/Mo at different temperatures. The laser excitation energy is 1.96 eV.....</i>	92
<i>Figure 5- 7 Comparison of Raman spectra of SWNTs synthesized from Co/Cu and Co/Mo at different temperatures. The laser excitation energy is 1.58 eV.....</i>	92
<i>Figure 5- 8 Comparison of absorption spectra of the conventional VA-SWNT synthesized by CoMo catalysts and 0.9-nm-diameter VA-SWNT synthesized by CoCu catalysts.....</i>	93

<i>Figure 5- 9 TEM images of SWNTs grown on Co/Cu catalysts. ....</i>	<i>93</i>
<i>Figure 5- 10 Raman spectra of the as-synthesized random-oriented SWNT films using Co/Cu catalysts under different CVD temperatures. The laser excitation energy is 2.54 eV. ....</i>	<i>95</i>
<i>Figure 5- 11 Raman spectra of the as-synthesized random-oriented SWNT films using Co/Cu catalysts under different CVD temperatures. The laser excitation energy is 1.96 eV. ....</i>	<i>95</i>
<i>Figure 5- 12 Absorption spectra of the as-synthesized random-oriented SWNT films using Co/Cu catalysts under different CVD temperatures. ....</i>	<i>96</i>
<i>Figure 5- 13 RBM of SWNTs grown on Co/Cu catalysts at different total pressure. ....</i>	<i>97</i>
<i>Figure 5- 14 Raman spectra of SWNTs grown by Co/Cu catalysts at different total pressure. ....</i>	<i>98</i>
<i>Figure 5- 15 SEM images of SWNTs grown by Co/Cu catalysts at different total pressure. ....</i>	<i>98</i>
<i>Figure 5- 16 Morphologies of the as-synthesized random-oriented SWNT films using Co/Mo catalysts by different CVD Time. ....</i>	<i>101</i>
<i>Figure 5- 17 Transmittance of as-synthesized random-oriented SWNT films using Co/Mo catalysts by different CVD Time. ....</i>	<i>101</i>
<i>Figure 5- 18 Raman spectra of the as-synthesized random-oriented and vertical-aligned SWNT films using Co/Mo catalysts. ....</i>	<i>102</i>
<i>Figure 5- 19 (a)-(f) Morphologies of the as-synthesized Vertically Aligned SWNT films using Co/Mo catalysts by different CVD Time. (g) Magnified SEM image of (f). ....</i>	<i>102</i>
<i>Figure 5- 20 Morphologies of the as-synthesized vertically aligned SWNT films using Co/Mo catalysts by different CVD Time with the ethanol flow rate of 50 sccm. ....</i>	<i>103</i>
<i>Figure 5- 21 Comparison of the morphology of the as-synthesized VA-SWNTs by different catalysts combination at the same temperature using SEM. ....</i>	<i>103</i>
<i>Figure 5- 22 Comparison of Raman spectra of SWNTs synthesized from Co/Cu, Co0.1/Cu and Co/Mo at different temperatures. The laser excitation energy is 2.54 eV. ....</i>	<i>105</i>
<i>Figure 5- 23 (a) Absorption spectra of SWNTs synthesized by different catalysts and temperature. (b-d) SEM images of corresponding SWNTs. ....</i>	<i>105</i>
<i>Figure 6- 1 Air-stable high-efficiency solar cells with dry-transferred SWNTs. ....</i>	<i>109</i>
<i>Figure 6- 2 Self-assembled microhoneycomb network of SWNTs for solar cells. ....</i>	<i>111</i>
<i>Figure 6- 3 Growth of sub-nanometer-diameter SWNTs films directly on substrate. ....</i>	<i>112</i>

# List of Tables

<i>Table 3- 1 Optical transmittance (at the wavelength of 550 nm) and sheet resistance (averaged values) of TCF70, TCF80 and TCF90 samples. ....</i>	<i>33</i>
<i>Table 3- 2 The power conversion efficiency (PCE), fill factor (FF), short-circuit current (<math>J_{sc}</math>) and open-circuit voltage (<math>V_{oc}</math>) of the SWNT/Si solar cells with the TCF70, TCF80 and TCF90 films measured immediately after fabrication, and those of the solar cell with TCF90 film measured 10 months after fabrication, as well as the series resistance (<math>R_s</math>), the shunt resistance (<math>R_{SH}</math>) and dark saturation current (<math>I_0</math>) through p-n diode equation modeling. ....</i>	<i>45</i>
<i>Table 4- 1 Optical transmittance (over the AM1.5G spectrum) and average sheet resistance of <math>\mu</math>-HN, collapsed HN and porous HN, and the photovoltaic performance of the fabricated solar cells – FF, short-circuit current (<math>J_{sc}</math>) and open-circuit voltage (<math>V_{oc}</math>) – for SWNT-Si solar cells under AM1.5G and 100 mW/cm<sup>2</sup> illumination. ....</i>	<i>70</i>
<i>Table 5- 1 Strategic directions of the growth control of SWNTs. ....</i>	<i>82</i>
<i>Table 5- 2 Experimental design for the effect of pressure on chiral distribution. ....</i>	<i>97</i>



# Nomenclature

SWNT	single-walled carbon nanotube
$a_1, a_2$	basic vectors of SWNTs in real space
$b_1, b_2$	basic vectors of SWNTs in momentum space
$C_h, T$	chiral vector and translational vector in the real space
$K_1, K_2$	chiral vector and translational vector in the momentum space
$d_t$	diameter of SWNTs
CVD	chemical vapor deposition
ACCVD	alcohol catalytic chemical vapor deposition
$\mu$ HN	micro honeycomb network
$J$ - $V$ characteristic	current density voltage characteristic
$V_{oc}$	open-circuit voltage
$J_{sc}$	short-circuit current
FF	fill factor
$R_s$	serial resistance
$R_{sh}$	shunt resistance
RBM	radial breathing mode
TCF	transparent conductive film
AM	air mass
VA-SWNT	vertically aligned single-walled carbon nanotube
P-CVD	growth on supported particles
S-CVD	growth on substrate
FC-CVD	floating catalysts





# Preface

All life on Earth is based on carbon. The discovery of carbon is as old as the history of human being, while the discovery of fullerene which is an allotrope of carbon gave birth to the advent of the new era of nanoscience and nanotechnology in the last decade. Carbon is also a material with extreme properties: Diamond, one of the allotropes of carbon, is the hardest material on earth known to date; graphite, which is also one of the allotropes of carbon, is so soft that could be used for writing and drawing. The discovery of two new allotropes of carbon, fullerene [1] and graphene [2, 3], have won two Nobel Prizes recently, the Nobel Prize in Chemistry 1996 (Robert F. Curl Jr., Sir Harold W. Kroto and Richard E. Smalley) and Nobel Prize in Physics 2010 (Andrei Geim and Konstantin Novoselov), respectively.

Before we start our amazing voyage further into the world of carbon, let us have a look at definition of carbon. Carbon is a normal element in the periodical table. It is a member of group 14 on the periodic table together with silicon (Si), germanium (Ge), tin (Sn) and lead (Pb). It has six protons and neutrons inside nucleus and two electrons revolving around nucleus in the  $1s$  orbital while other four electrons rotating in the next energetic orbital ( $2s$ ,  $2p$ ). Carbon takes many forms in nature and has a wide range of allotropes in different dimensions, as shown in Figure 0-1. The most

well-known allotropes are the aforementioned graphite and diamond, both of which are bulk forms of carbon, illustrated in Figure 0-1. The diamond is composed of  $sp^3$  hybridized carbon atoms with a tetrahedral structure, sharing a bond with neighboring atoms. The graphite is composed of stacked layers of graphene, which is a single-layered  $sp^2$  hybridized carbon atoms. Although the theoretical prediction of the existence of graphene dates back to the 1960, the experimental discovery was realized until 2004 by Andrei Geim and Konstantin Novoselov, both of whom won the Nobel Physics Prize in 2010.

By rolling graphene up seamlessly, a single-walled carbon nanotube can be obtained. The amazing aspect of single-walled carbon nanotubes (SWNTs) is that depending on the way the graphene is rolled up, *i.e.*, the rolling direction and diameter of tubes, carbon nanotubes could either metallic or semiconducting, with the band gap up ranging from 0.5 eV to 2 eV. This means that essentially most of the semiconductors in use currently, *e.g.*, Si, SiGe, GaAs, other III-V, II-VI *etc.*, could be replaced with SWNTs. Additionally, SWNTs also exhibits excellent mechanical and thermal properties. The strength of carbon nanotubes is so strong that theoretically, it is possible to build up a moon elevator by carbon nanotubes. SWNT is one of the materials that have the highest thermal conductivities to date. Over 100,000 papers have been published and indexed by ISI Web of Science<sup>TM</sup> since the discovery of multi-wall carbon nanotubes and SWNTs by Iijima in 1991 [4] and 1993 [5], respectively. The number is still increasing rapidly as shown in Figure 0-2.

One fullerene molecule consists of sixty carbon atoms completely bonded with icosahedron symmetry to form a sphere, a zero-dimensional carbon allotrope was discovered by H. Kroto, J.R. Heath, S.C. O'Brien, R.F. Curl, and R. Smalley in 1985. The most successful application of fullerene is PC<sub>60</sub>BM and PC<sub>70</sub>BM which are used for organic solar cells.

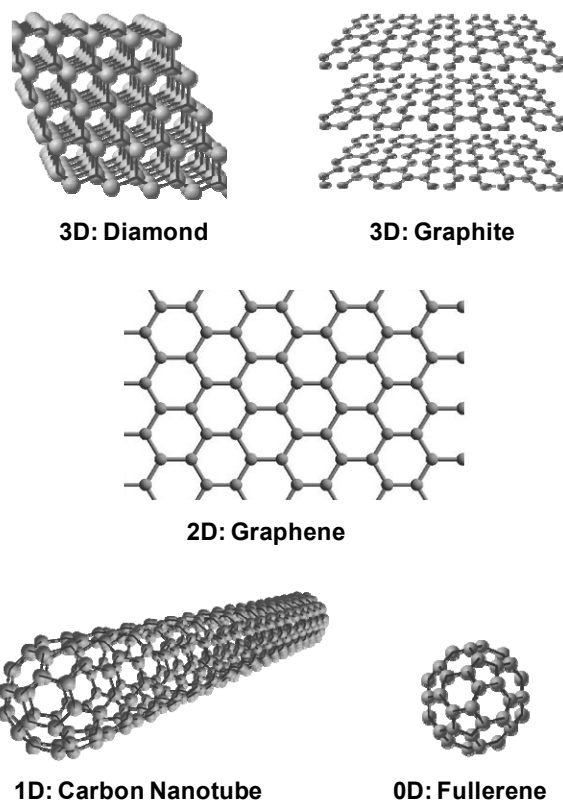


**Figure 0- 1** The variety of carbon allotropes: diamond and graphite are 3-dimensional; graphene, carbon nanotubes and fullerene are two-, one- and zero-dimensional, respectively. This artwork is adopted from the website of this laboratory: Shigeo Maruyama’s Carbon Nanotube Site – <http://photon.t.u-tokyo.ac.jp>

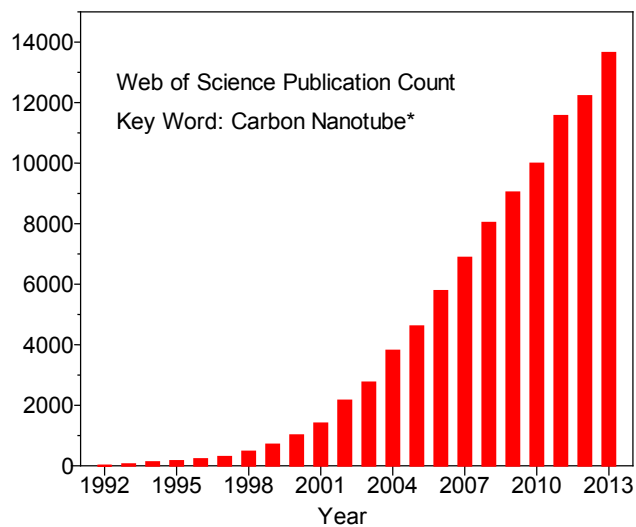


**Figure 0- 2** Number of papers published and indexed by Web of Science as of March 2014. Key words: (carbon nanotube\*)

As we discussed above, carbon nanotubes are one of the most intensively investigated materials so far, owing to their amazing and promising properties as well as the flexible tunability. The knowledge and understanding of carbon nanotubes have become quite deep and wide. However, these knowledge and understanding are far from systematic and cause even more unknowns. There is still a long way to go for the real applications of carbon nanotubes.

# Chapter 1

## Introduction

*"If I have seen further it is by standing on the shoulders of giants."*

— *Sir Isaac Newton*

---

After more than 20-year efforts of world-wide scientists, various accomplishments have been achieved and some of the knowledge is commonly acknowledged and widely used. This chapter will discuss the fundamental physics and metrology of carbon nanotubes and review the state of the art of the solar cell applications, upon which the motivation of this PhD project presented in this whole dissertation is built.

Carbon nanotube is a family of materials. In a general sense, carbon nanotubes are divided into single-walled carbon nanotubes (SWNTs) and multi-wall carbon nanotubes (MWNTs). Single-walled carbon nanotubes are single atomic layered cylinder of  $sp^2$  hybridized carbon atoms. Depending on the way the graphene sheet is rolled up, SWNTs can be either metallic or semiconducting, with the band gap ranging from 0.5 eV to 2 eV. This chapter will first define the atomic architecture of SWNTs and explain the structure-related electronic and optical properties at first. Then the characterization methods of SWNTs, including electron microscopy, resonance Raman spectroscopy, optical absorption spectroscopy and the four-point probe method for the measurement of the sheet resistance of thin films will be introduced. Last but not the least, the possible contribution of SWNTs to solar cells is discussed, before which the basic science and state of the art of solar cells are provided.

## 1.1 Physics of Carbon Nanotubes

### 1.1.1 Atomic Structure of Graphene and SWNTs

A SWNT can be described as a single atomic layer of a graphite sheet (*i.e.* graphene) rolled up into a seamless cylinder. It is necessary to describe graphene before the introduction of SWNTs. **Figure 1- 1 (a)** and **(b)** show the unit cell of graphene in real space (lattice) and the momentum space (reciprocal lattice), respectively. In the Cartesian  $x$ - $y$  coordinate, the basic vectors  $\mathbf{a}_1$  and  $\mathbf{a}_2$  in real space are expressed as

$$\mathbf{a}_1 = (\sqrt{3}a/2, a/2), \mathbf{a}_2 = (\sqrt{3}a/2, -a/2) \quad (1-1)$$

where

$$a = |a_1| = |a_2| = 1.42 \times \sqrt{3} = 2.46 \text{ \AA} \quad (1-2)$$

is the lattice constant of a graphene. In the  $kx$ - $ky$  coordinate system, the corresponding basic vectors in the reciprocal lattice  $\mathbf{b}_1$  and  $\mathbf{b}_2$  is defined as

$$\mathbf{b}_1 = \left( 2\pi / \sqrt{3}a, 2\pi / a \right), \mathbf{b}_2 = \left( 2\pi / \sqrt{3}a, -2\pi / a \right) \quad (1-3)$$

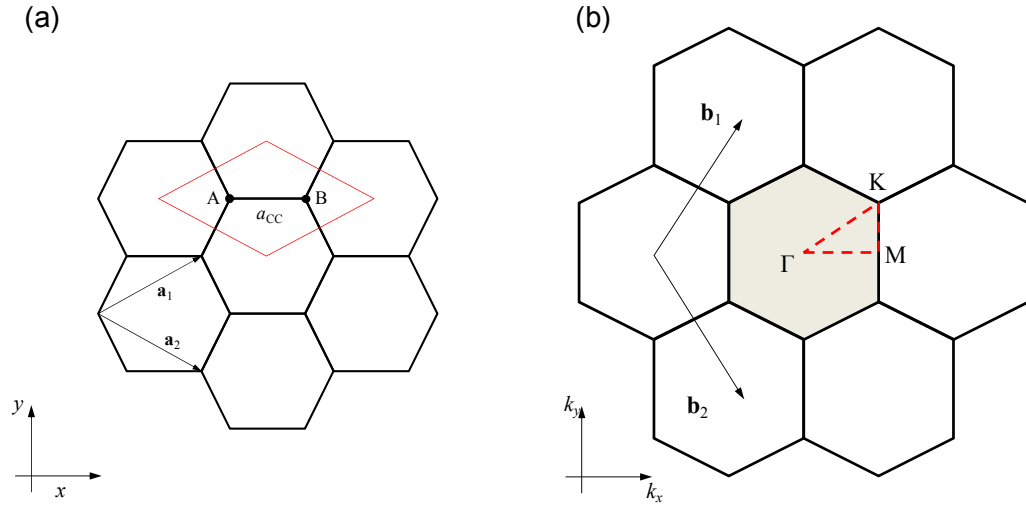


**Figure 1- 1** Unit cell of graphene in (a) real space, with the red line rhombus showing unit cell, and (b) momentum space, with the shaded hexagon showing the Brillouin zone and red dashed line showing the symmetry point.

The shaded hexagon in **Figure 1- 1 (b)** is the Brillouin zone of graphene. The three high symmetry points,  $\Gamma$ ,  $K$  and  $M$  of the Brillouin zone denote the center, the corner, and the center of the edge, respectively. Compared with graphene, SWNT has a chiral vector  $C_h$  that defines the way graphene is rolled up, *i.e.*, the structure of the SWNT,

$$\mathbf{C}_h = n\mathbf{a}_1 + m\mathbf{a}_2 \equiv (n, m) \quad (1-4)$$

which is often described by the pair of indices  $(n, m)$  that denote the number of unit vectors in the hexagonal honeycomb lattice contained in the vector  $\mathbf{C}_h$ . The nanotube diameter  $d_t$  can be written in terms of the integers  $(n, m)$  as

$$d_t = C_h / \pi = \sqrt{3}a_{CC}(m^2 + mn + n^2)^{\frac{1}{2}} / \pi \quad (1-5)$$

where  $a_{CC}$  is the nearest-neighbor C–C distance (1.421 Å in graphite), and  $C_h$  is the length of the chiral vector  $\mathbf{C}_h$ . As shown in **Figure 1- 2**, the angle between the chiral vector  $\mathbf{C}_h$  and  $\mathbf{a}_1$  is named as the chiral angle. The chiral angle  $\theta$  is given by

$$\theta = \tan^{-1} \left[ \sqrt{3}m / (m + 2n) \right] \quad (1-6)$$

For armchair SWNT,  $\theta$  equals to  $30^\circ$ , while for zigzag SWNT,  $\theta$  is  $0^\circ$ . The chiral angle for chiral tubes is between  $0^\circ$  and  $30^\circ$ . So far, the atomic structure of an SWNT is described by its unit cell OBB'A. The other unit vector which is vertical to the chiral vector  $\mathbf{C}_h$  in the unit cell is labeled as translational vector  $\mathbf{T}$ . The translational vector  $\mathbf{T}$  is the shortest repeat distance along the SWNT axis and is described as

$$\mathbf{T} = t_1 \mathbf{a}_1 + t_2 \mathbf{a}_2 \equiv (t_1, t_2) \quad (1-7)$$

where  $(t_1, t_2)$  correlates to  $(n, m)$  as

$$t_1 = (2m + n) / d_R, \quad t_2 = -(2n + m) / d_R \quad (1-8)$$

where  $d_R$  is the greatest common divisor of  $(2n+m, 2m+n)$

$$d_R = \begin{cases} d & \text{if } n - m \text{ is not a multiple of } 3d \\ 3d & \text{if } n - m \text{ is a multiple of } 3d \end{cases} \quad (1-9)$$

where  $d$  is the greatest common divisor of  $(n, m)$ . In the real space, the unit cell of a SWNT is larger than that of graphene due to the existence of chiral and translational vectors  $\mathbf{C}_h$  and  $\mathbf{T}$ . The number of the hexagons contained in one unit cell of SWNT is given as

$$N = \frac{|\mathbf{C}_h \times \mathbf{T}|}{|\mathbf{a}_1 \times \mathbf{a}_2|} = \frac{2(n^2 + m^2 + nm)}{d_R} \quad (1-10)$$



Correspondingly, in the momentum space (reciprocal lattice), the unit space of a SWNT is much smaller, as shown in **Figure 1- 3**. The Brillouin zone of a SWNT is the cutting lines on reciprocal lattice of graphene. As the chiral vector  $\mathbf{C}_h$  and translational vector  $\mathbf{T}$  define the unit cell of a SWNT in the real space, in the momentum space, the vector  $\mathbf{K}_1$  in the circumferential direction and  $\mathbf{K}_2$  along the nanotube axis direction define the Brillouin zone.  $\mathbf{K}_1$  and  $\mathbf{K}_2$  are related with  $\mathbf{C}_h$  and  $\mathbf{T}$

$$\mathbf{C}_h \cdot \mathbf{K}_1 = 2\pi, \quad \mathbf{T} \cdot \mathbf{K}_1 = 0, \quad \mathbf{C}_h \cdot \mathbf{K}_2 = 0, \quad \mathbf{T} \cdot \mathbf{K}_2 = 2\pi. \quad (1-11)$$

Therefore,  $\mathbf{K}_1$  and  $\mathbf{K}_2$  are given as

$$\mathbf{K}_1 = \frac{1}{N}(-t_2 \mathbf{b}_1 + t_1 \mathbf{b}_2), \quad \mathbf{K}_2 = \frac{1}{N}(-m \mathbf{b}_1 - n \mathbf{b}_2) \quad (1-12)$$

The  $N$  cutting lines on the momentum space are resulted from  $N$  wave vectors  $\mu \mathbf{K}_1$  ( $\mu=1-N/2, \dots, N/2$ ). Each cutting line gives one  $\pi$ -  $\pi^*$  band, which will be discussed in the following sections.

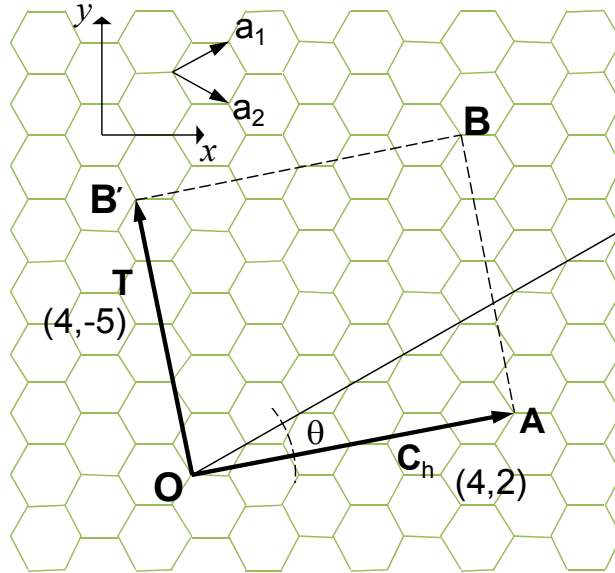


**Figure 1- 2** The chiral vector  $\mathbf{C}_h$  for an  $(n,m) = (4,2)$  SWNT. The chiral angle is shown by  $\theta$ .

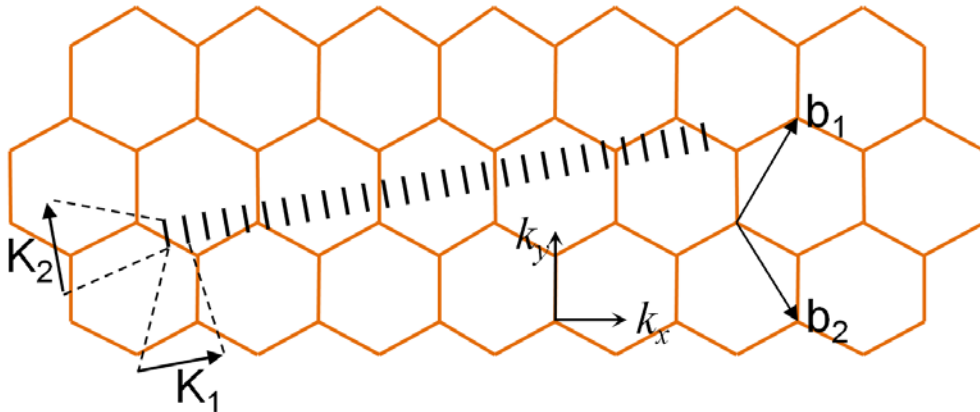


Figure 1- 3 The Brillouin zone of a (4,2) SWNT in the reciprocal lattice.

### 1.1.2 Structure-Related Properties of Graphene and SWNTs

Through tight-binding method, the three dimensional band structures can be calculated as shown in **Figure 1- 4 (a)**. The detailed calculation can be found in Ref. [6]. The  $\pi$  band and the  $\pi^*$  band of graphene are touching each other at the K point, demonstrating the quasi-metallic properties. Owing to the chiral vector of SWNTs, the band structure of SWNTs is the discrete cutting lines on that of graphene, as shown in **Figure 1- 4 (b)**. And depending on the chiral vectors or chiralities of SWNTs, the cutting lines may or may not come across the K point. If the cutting lines happen to come across the K point, then the SWNT is metallic; if not, then the SWNT is semiconducting.

The electronic density of states can then be calculated from the tight-binding theory. **Figure 1- 5** shows the eDOS of SWNTs with three different chiralities, of the which the data source is from the website of this group. The sharp peaks in the eDOS is called van Hove singularities (vHS), which is induced by the one-dimensional quantum confinement. The energy separation between the first vHS can be considered

as band gap. The (4,2) SWNT is the smallest nanotube that can be synthesized so far, with the theoretical band gap of 2 eV; the (6,5) SWNT has the band gap of 1.4 eV experimentally, and 1.1 eV theoretically; the (10,10) SWNT has continuous band structure and the resulting metallic properties. Generally, the band gap of SWNTs ranges from 2 eV to 0.5 eV.

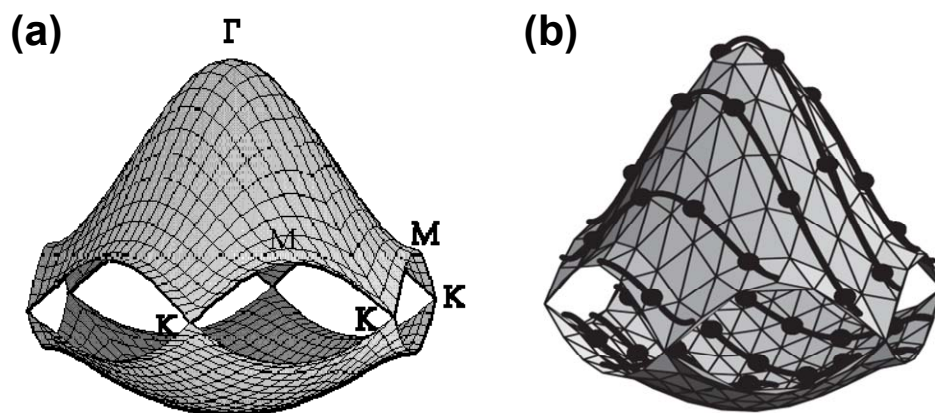


**Figure 1- 4 (a) Three-dimensional band structure of graphene. Adoped with permission from Prof. Shigeo Maruyama’s Carbon Nanotube Site (b) Three-dimensional band structure of SWNT. Reprinted from [8], Copyright 2005, with permission from Elsevier.**

The variety of the band structure is one of the advantages of SWNTs, making SWNTs capable for multipurpose applications. Based on the electronic structure of SWNTs, the periodic table of SWNTs can be drawn. **Figure 1- 6** gives the periodic table. If the chiral index  $n - m$  is divisible by 3, then the SWNT is metallic; if not, the SWNT is semiconducting. The structure-dependent properties of SWNTs are one of the most scientifically interesting part, on which a large part of the SWNT research is focused. The idea of application of SWNTs for solar cells is also originated from it.

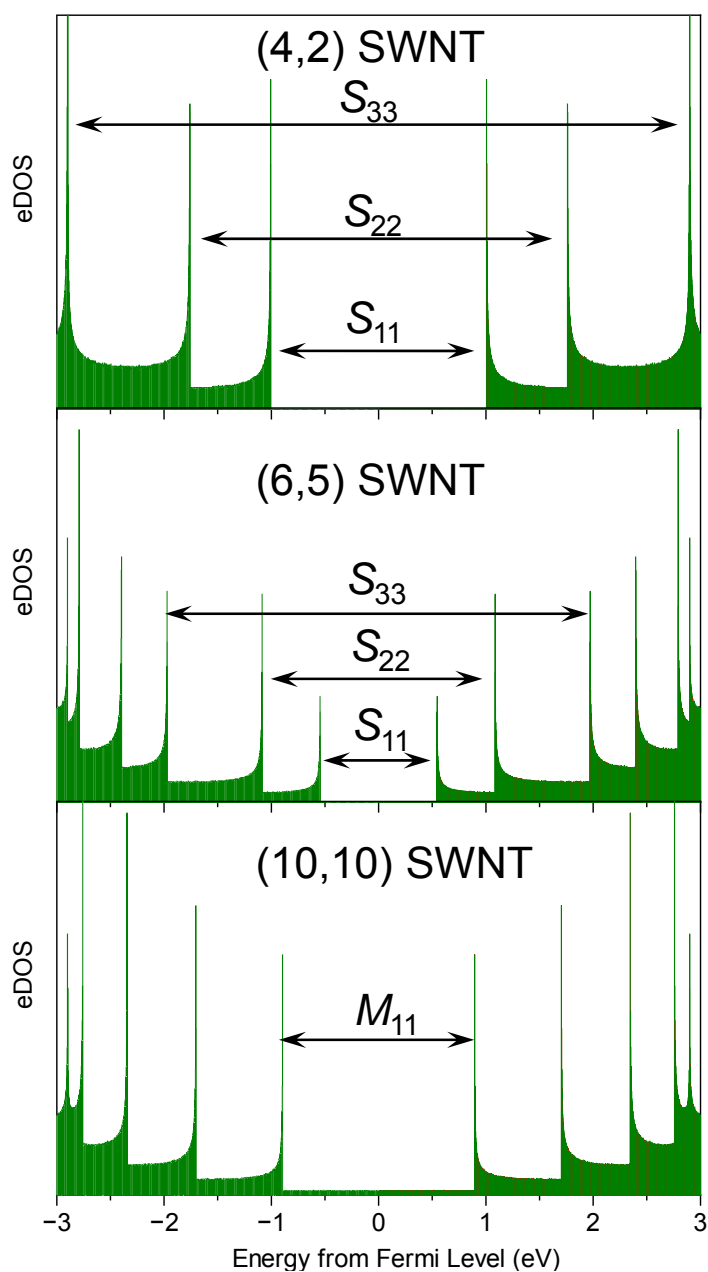


**Figure 1- 5** Electronic density of states of SWNTs with different chiralities. From top to bottom: (4,2) SWNT, (6,5) SWNT and (10,10) SWNT. Data source from [www.photon.t.u-tokyo.ac.jp](http://www.photon.t.u-tokyo.ac.jp)

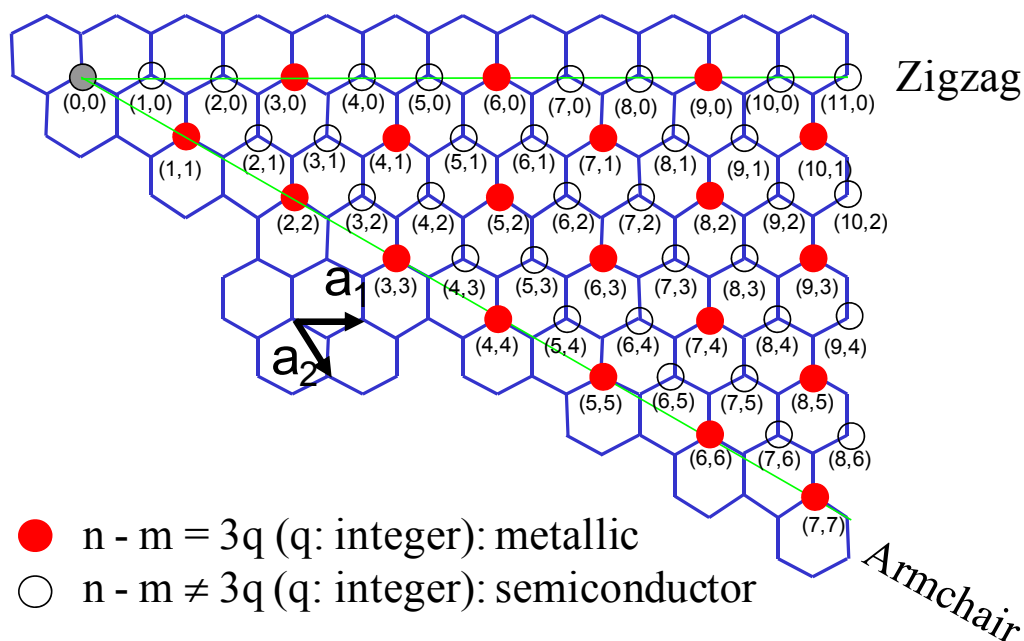


**Figure 1- 6 SWNT (n,m) indices.** Here, a red solid point represents metallic nanotube and a black open circle represents semiconductor nanotubes. The condition for the metallic nanotube is:  $2n+m=3q$  ( $q$ : integer), or  $(n-m)/3$  is integer. This artwork is adopted from the website of this laboratory: Prof. Shigeo Maruyama's Carbon Nanotube Site – <http://photon.t.u-tokyo.ac.jp>

## 1.2 Metrology of Carbon Nanotubes

After the explanation of the atomic and electronic structures of SWNTs as well as the theoretical properties, Chapter 1.2 deals with the experimental characterization of SWNTs. The diameters for SWNTs range from 1 to 3 nm, which is two orders of magnitude smaller than the wavelength of visible light (390 ~ 700 nm). The resolution of visible light cannot reach the level of SWNTs even with most precise optical microscope. To 'see' an SWNT, electron microscope and spectroscopy are employed to obtain enough information. This part of the thesis will explain four most frequently used techniques, *i.e.*, scanning electron microscopy (SEM), transmission electron microscopy (TEM), Raman spectroscopy and absorption spectroscopy for the characterization. The four-point probe measurement will also be introduced.

### 1.2.1 Electron Microscopy

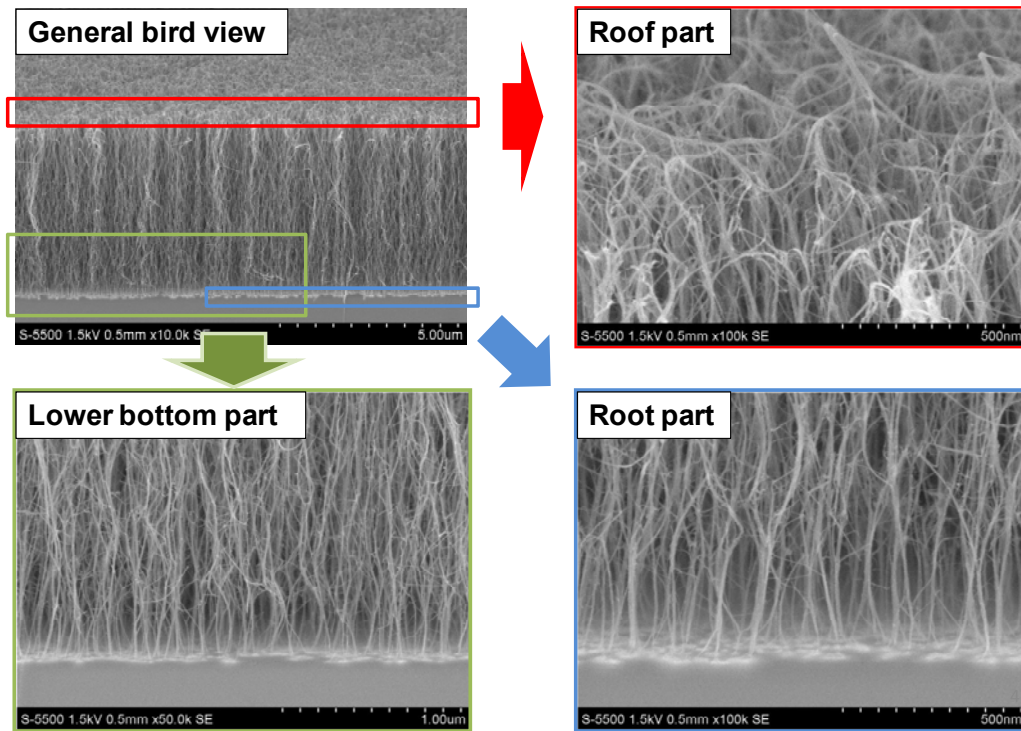


**Figure 1- 7 Typical SEM images of vertical-aligned SWNTs synthesized by the ACCVD method with Co and Mo as catalysts.**

The resolution of optical microscopy is approximately the wavelength of visible light, which is 500 ~ 800 nm. Electron microscopy is used when the resolution of optical microscopy is not enough. Owing to the wave-particle duality, the electrons with accelerated voltage have shorter wavelength than visible light, hence much higher resolution. At very high voltage, *e.g.*, several keV as used in scanning electron microscopy (SEM) and 200 keV as used in transmission electron microscopy (TEM), the speed of the electrons is approaching light speed and the wavelength of electrons is much smaller than X-ray, which is at hundreds picometer ( $10^{-12}$  m). Over 100, 000 times magnification can be achieved. The difference between SEM and TEM not only lies in the acceleration voltage but also the electrons detected. In SEM, the beams of electrons scan on the surface of the sample. The scattered secondary electrons are

detected to obtain the image. While in TEM, the electrons are sufficiently accelerated so much that they transmit through the sample and reach the CCD below the sample. **Figure 1- 7** and **Figure 1- 8** show the typical SEM and TEM images of SWNTs, respectively.

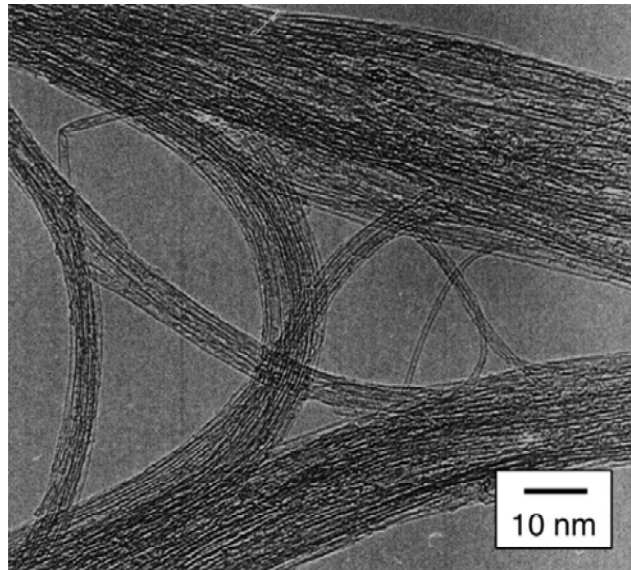


**Figure 1- 8** Typical TEM images of high-quality SWNTs synthesized by ACCVD method with Fe and Co as catalysts. Reprinted from [7], Copyright (2002), with permission from Elsevier.

### 1.2.2 Raman Spectroscopy

The Raman spectroscopy uses the inelastic scattering with the lattice to read information of the structure of the matter. The inelastic scattering includes three processes: an electron is excited by absorbing the energy from a photon; the excited electron is scattered and emits (or absorb) a phonon; the electron relaxes back to valence band and emits a photon. In general, the photon travels through the lattice and loses or obtains the energy of a phonon. The Raman spectrum is basically the energy difference between the incident and released photon. Raman spectroscopy is a very

useful tool to characterize SWNTs. On the other hand, the special and abundant features of SWNT structure also provide a good platform for the study of Raman spectroscopy.

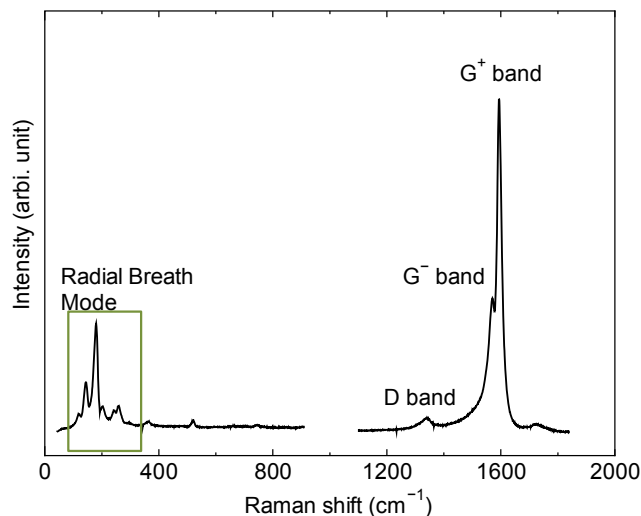


**Figure 1-9** A typical Raman spectrum of SWNTs synthesized by ACCVD method.

The detail discussion on Raman process which can be found in various literatures, *e.g.* [6, 8]. Here only the main Raman features of carbon nanotubes are discussed. **Figure 1-9** shows the typical Raman spectrum of the as-synthesized vertically aligned SWNTs by ACCVD method. The low-frequency feature, *i.e.* radial breath mode (RBM) can only be observed in SWNTs, and is resulted from bond stretching of the coherent lattice out-of-plane movement in the radial direction. The RBM is related with the chirality of the SWNT. The Kataura plot (**Figure 1-10**) is the theoretical relation between the RBM Raman shift with the chiralities of SWNTs, and has been proved experimentally. Another strong feature is G-band, which is the in-plane vibrational mode. The separation of  $G^+$  and  $G^-$  modes can be used to characterize the diameter of SWNTs, as shown in **Figure 1-11** [9]. The position of G-band can be used to investigate the charge transfer of SWNTs.



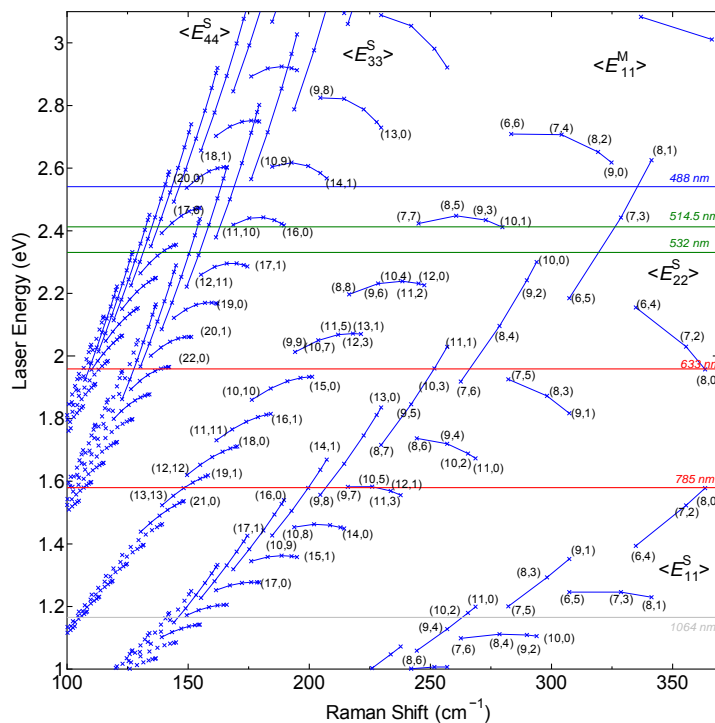


Figure 1- 10 Kataura plot of single-walled carbon nanotubes with laser excitation energy.

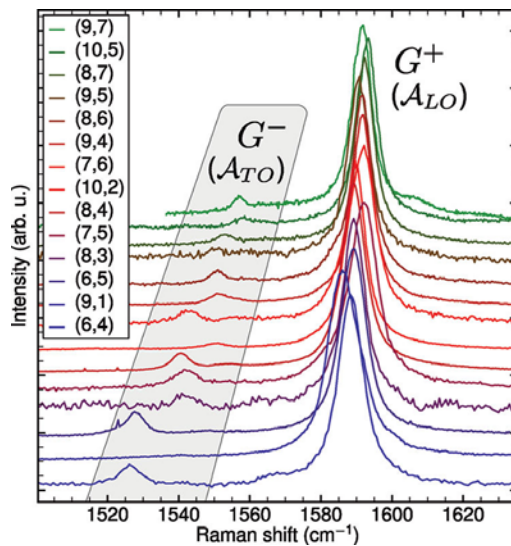
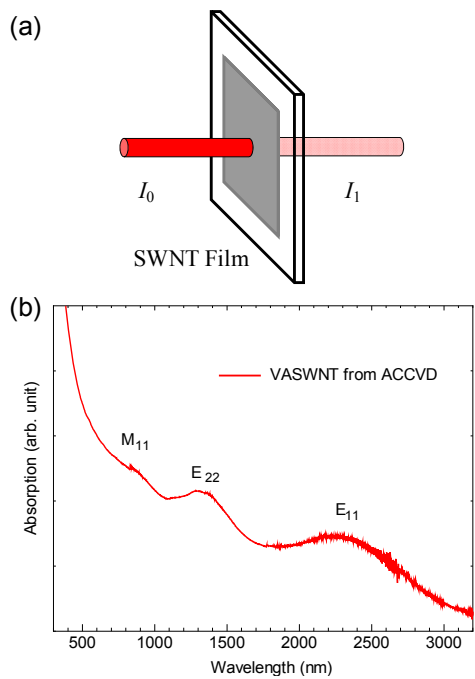
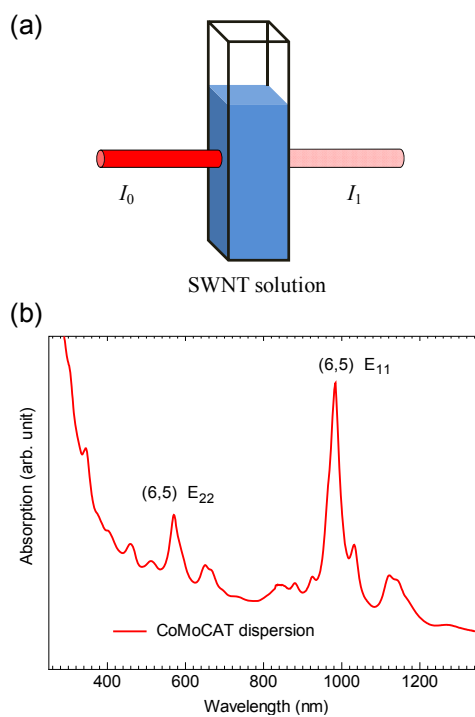


Figure 1- 11 Position of G- and the separation of G+ and G- for SWNT of different chiralities: the G- Kataura plot. Reprinted with permission from [9]. Copyright (2012) American Chemical Society.

### 1.2.3 UV-vis-NIR Absorption Spectroscopy

Light has wave-particle duality. From the perspective of wave, light can travel through matter, with their intensity decrease exponentially by the Beer's law. From the perspective of particle, when a photon hits an atom, its energy can be absorbed by electrons in the atom at a certain probability. In the SWNTs, when photon energy matches the vHS, the probability of the photon being absorbed will increase significantly. This results a peak in the absorption spectrum. The electronic energy transition of the first vHS is called  $E_{11}$ . When the photon energy is as high as the energy transition of the second vHS, absorbance could also happen. The resulted peak is named as  $E_{22}$ . Although with a continuous band structure, metallic SWNTs also have very weak absorbance, which is usually named as  $M_{11}$ . Combining the first and second energy transition obtained from the absorption spectra would provide enough information to recognize the chirality of an SWNT.

**Figure 1- 12 (a)** shows the schematic of the absorption spectroscopy measured in liquid state. The absorption spectrum of CoMoCAT SWNTs dispersed in water is shown in **Figure 1- 12 (b)**. As the SWNTs are isolated with each other by surfactant, their absorbance is very strong compared with that measured in solid state. The quenching induced by bundles could substantially weaken the absorbance shown in **Figure 1- 13**. The spectrum obtained from solid-state measurement could range from ultraviolet (below 350 nm) up to several micrometer wavelength, while for liquid-state measurement, the wavelength could only cover up to 1600 nm wavelength due to the significant noise from water.



### 1.2.4 Optical and Electrical Properties of SWNT Assemblies

This part discusses the application of carbon nanotubes as a transparent conductive film. The current most popular material for transparent conductive film is indium tin oxide (ITO), which has rare earth metal indium. The SWNTs are expected to be one of the most promising materials to replace ITO serving as the next-generation transparent conductive film, owing to the ballistic transport of individual SWNTs. The sheet resistance of the SWNT films can be measured by a four-point probe method as shown in **Figure 1- 14**. The contact resistance between the probe and the materials as well as the spreading resistance can be eliminated by applying voltage at the central two probes and measuring the current at the outer two probes.

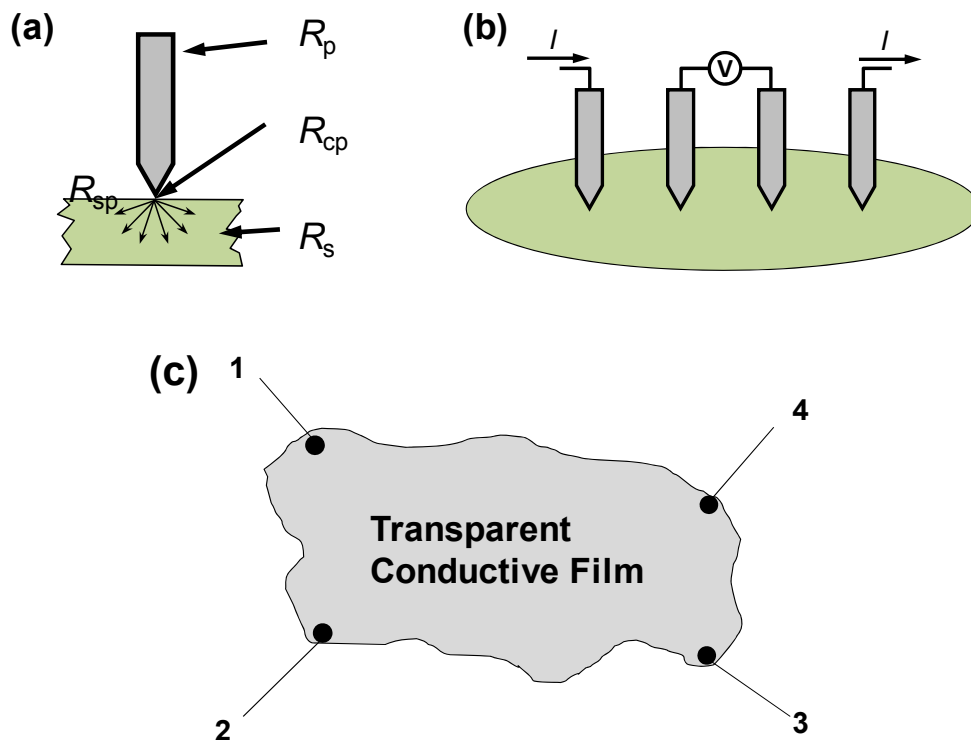


**Figure 1- 14** Four-point probe measurement. (a) Resistance at the contact between the probe and material. (b) Schematic of four-point probe setup. (c) Schematic of van de Pauw four-point measurement for random-shaped thin film.

The van de Pauw method as shown in **Figure 1- 14 (c)** is for a random-shaped film, which requires twice measurement: applying voltage at probe 1 and 2, and measuring the current at probe 3 and 4; applying voltage at probe 1 and 3, and measuring the current at probe 2 and 4. The sheet resistance is an averaged value between the twice measurement with a correction factor. The correction factor is dependent on the difference between the twice measurement.

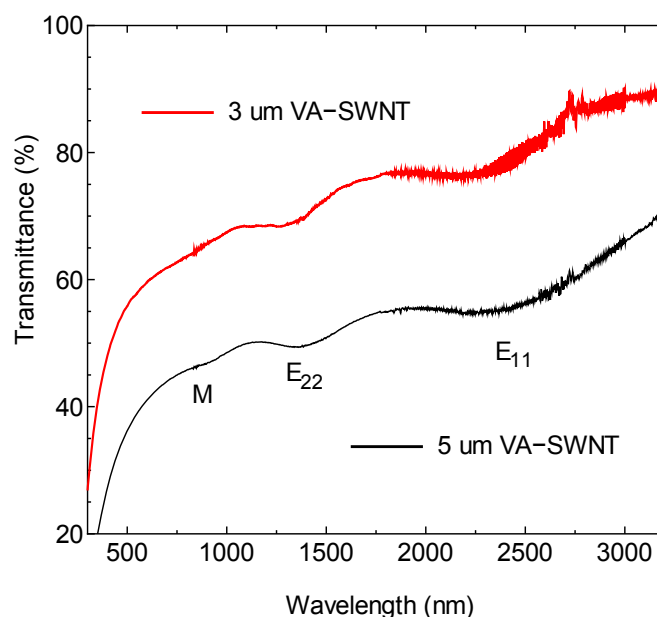


**Figure 1- 15** Transmittance spectra of vertically aligned SWNT (VA-SWNT) films with different thicknesses.

The transmittance of SWNTs can be measured by the same equipment as in UV-vis-NIR spectroscopy. Typical transmittance spectra are shown in **Figure 1- 15**. Usually the transparency of the SWNT films is defined at the transmittance at the wavelength of 550 nm, and denoted as  $T_{550}$  afterwards. In this thesis, a new transparency for the application of solar cell is defined as  $T_{AM1.5G}$ , which is the spatial-average transparency over the AM1.5G. In the following chapters, the difference between the  $T_{550}$  and  $T_{AM1.5G}$  would be very clear, especially when the doping of SWNTs is involved.



# Chapter 2

## Motivation, Challenges and Organization of the Thesis

### 2.1 What Does SWNT Have to Do with Solar Cells

The research topic of the highest scientific importance for solar cell scientists is how to break the Shockley – Queisser limit [10]. The Shockley – Queisser limit is derived from the second law of thermodynamics using the temperature of the sun and temperature of solar cells, based on two assumptions. These two assumptions are (1) Photons with energy larger than the band gap could be absorbed, and (2) One photon could generate one exciton, both of which are not applicable for SWNTs naturally. Owing to the quantum confinement, the electronic density of states of SWNTs is composed of van Hove singularities. Therefore, the photons with energy larger than the energy transition of SWNTs cannot be absorbed. Moreover, the multiple exciton generation phenomenon has been experimentally observed and theoretically explained. Therefore, the second assumption cannot be applied to SWNTs. The breakdown of

Shockley – Queisser limit for SWNTs makes it possible for high-performance SWNT-based solar cells beyond the Shockley – Queisser limit.

The quantum structure of SWNTs also provides other appealing properties for the applications of solar cells. SWNTs have tunable band gap ranging from 2 eV to 0.5 eV, which makes it possible for the applications of tandem cells. A typical tandem cell is shown in **Figure 2- 1**, composed of GaInP with band gap of 1.8 eV, GaInAs with the band gap of 1.4 eV and Ge with band gap of 0.7 eV. The three layers absorb different spectrum of solar irradiance, which makes the efficiency of solar cell higher than 50% [11]. **Figure 2- 2** shows a possible structure of the SWNT tandem cell. Each layer of SWNTs could absorb a certain spectrum to maximize the total efficiency.

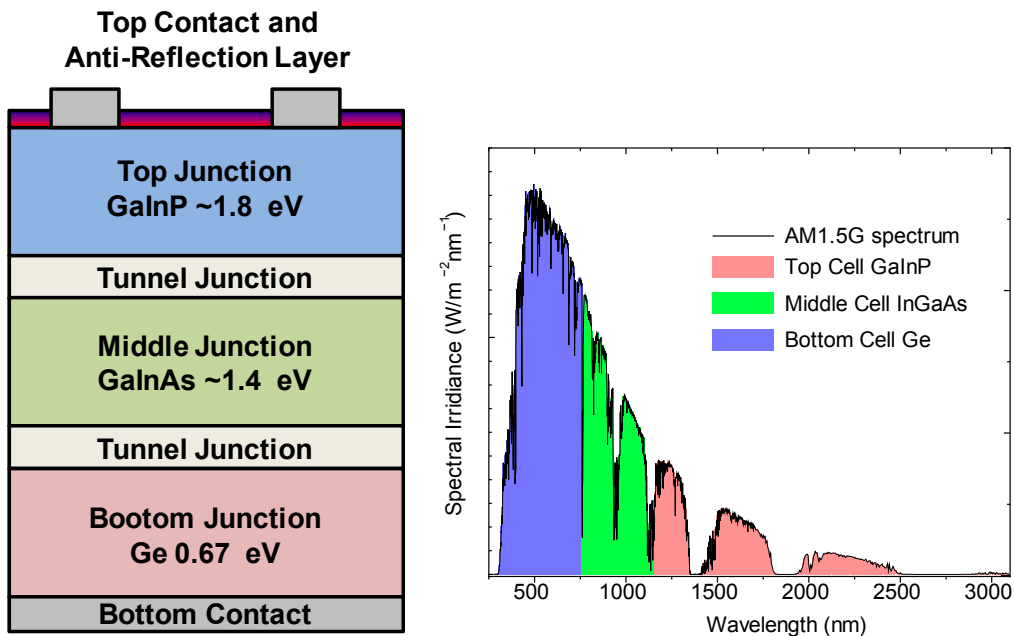


**Figure 2- 1 Schematic of tandem solar cell**

Moreover, high electron mobility of SWNTs would facilitate the charge transport inside the solar cell. Last but not the least, SWNT is one of the strongest materials in the world. Many flexible devices has been fabricated and reported based on SWNTs.



It can be expected to fabricate flexible solar cells using SWNTs. The above-mentioned advantages make the SWNT one of the most promising materials for solar cells applications.

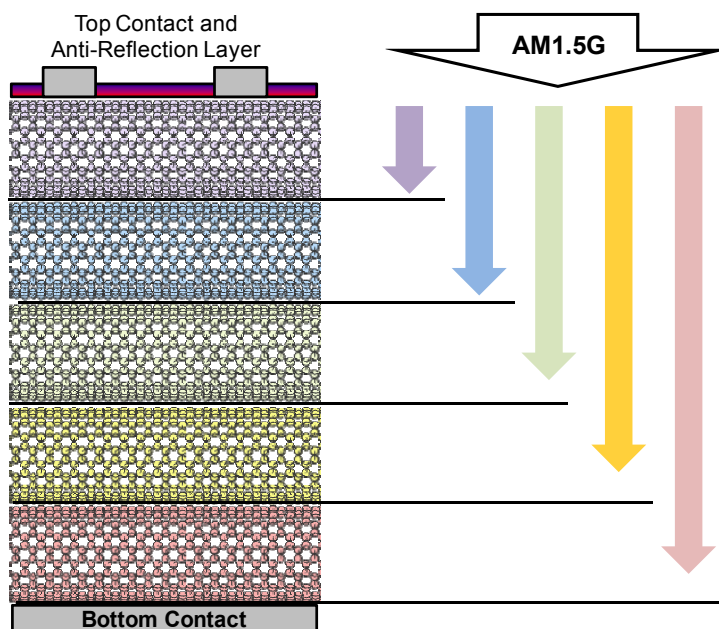


Figure 2- 2 The ultimate architecture of tandem SWNT solar cells.

## 2.2 Challenges of Applying Carbon Nanotubes in Solar Cells

With all the advantages discussed in Chapter 1, the highest efficiency of solar cells using the band gaps of SWNTs has been reported as 1%. The three main challenges have hindering the full exploitation of SWNTs for the solar cell applications: (1) The SWNTs synthesized on substrates or by floating catalysts have too large diameter. The reduction of the diameter of SWNTs from 2 nm to 1 nm would lead to the increase of the band gap from 0.5 eV to 1.2 eV which is possible for the applications of solar cells. However, this has not been achieved so far. This is the challenge at the nanoscale. (2) The one-dimensional SWNTs do not grow into a three-dimensional bulk like conventional semiconductors. The gap between the properties of SWNT assemblies and the individual SWNTs is the challenge at the

microscale. (3) Before the first two challenges are solved, the technique of amounting SWNTs to photovoltaic devices needs further investigation and understanding, which could be categorized into the challenge at the macroscale. This doctoral thesis aims at controlling the structures and properties of single-walled carbon nanotube (SWNTs) at the macroscale, microscale and nanoscale levels for the applications of high-performance solar cells.

As a mechanical engineer, I am motivated at answering the challenges of SWNTs for the application of solar cells systematically in all three levels and bridging the amazing nanomaterial to the real world applications.

### **2.3 Organization of the Thesis**

The organization of research in the Thesis is based on the three challenges described in Chapter 2.2. The research in Chapter 3 is for answering the macroscale challenge. The discussion of the solar cell application is on the device level and focuses on the real-world applications. The performance of the solar cell is further improved in Chapter 4 by the micro-honeycomb network of SWNTs induced from breath figure of water vapor. In Chapter 5, the research goes deeper to the nanoscale level. The diameter of the SWNTs is tuned from 2 nm to 0.8 nm, which is a great step towards the direct application of SWNT to solar cells. Finally, the thesis is summarized by the contributions to the whole research community.

# Chapter 3

## High-Efficiency Air-Stable SWNT-Silicon Heterojunction Solar Cells

### 3.1 Research Background and Literature Review

Single-walled carbon nanotubes (SWNTs) possess excellent optical [12], electrical [13], mechanical and thermal properties [14] as well as chemical stability. Specifically, for the light harvesting application, SWNTs have the superiorities in terms of the wide spectrum of absorption ranging from near-infrared to visible wavelength, high electrical conductivity at high transparency [15-17] as well as the multiple exciton generation [18, 19]. Combined with earth abundance and chemical stability, the SWNT is supposed to be a very promising candidate for next-generation solar cell applications [20, 21].

Recently, the SWNT/Si solar cells are drawing emerging attentions owing to their simple and efficient structure [22-32]. The power conversion efficiencies (PCEs) of SWNT/Si solar cells have been improved an order of magnitude during last five years. However, the so-far-reported peak PCEs of the SWNT/Si solar cells were all suffered from degradation, which is hindering their further applications. The SWNT/Si solar cells could lose almost 50% PCE after hours in air, and even with protection, the PCE still degraded by 20%. This could be attributed to that the peak PCEs were boosted by nitric acid or gold salt doping or ionic liquid which were very instable. Another issue remained controversial is the working mechanism of the SWNT/Si solar cells. Initially, the SWNT/Si solar cell was proposed as a  $p$ - $n$  heterojunction by Jia *et al.* [23] Based on this hypothesis, (6,5) enriched SWNTs were used to further increase the built-in potential [33]. However, the incident photon conversion efficiency (IPCE) spectrum showed no obvious relationship between the SWNT absorption and the solar cell external quantum efficiency. In addition, the efficiency of graphene/Si solar cell [34, 35] became comparable with that of the SWNT/Si solar cell. The SWNT/Si solar cells were considered as a Schottky-barrier junction. One characteristic that could distinguish the  $p$ - $n$  junction and the Schottky-barrier junction is the effect of the interfacial oxide layer. For a conventional Schottky-barrier junction, inserting an interfacial oxide layer between the metal electrode and semiconductor would eliminate the pinning of Fermi level and thus improve the PCE, while the opposite case applies for a  $p$ - $n$  junction. Until now, both significant improvement [36] and degradation [27] of the PCEs were obtained after the removal of the interfacial oxide layer. These controversial results call with high necessity for more solid experimental proof for the further understanding of the SWNT/Si solar cells.

## 3.2 Materials and Methods

### 3.2.1 Synthesis of SWNT Films

The randomly oriented SWNT films with high purity and long nanotube bundle length were synthesized by the aerosol CVD method [15, 16]. The floating catalyst aerosol CVD was carried out in a scaled-up reaction tube with the diameter of 150 mm. Ferrocene vapor was thermally decomposed in the gas phase in the aerosol CVD reactor at the temperature of 880 °C. The CO gas was supplied at 4 L/min and decomposed on the iron nanoparticles, which resulted in the growth of SWNTs. The floating catalysts have three dimensional freedom which leads to the long bundle length. The as-synthesized SWNTs were collected by passing the flow through microporous filters at the downstream of the reactor. The transparency of the SWNT films was controlled by changing the collection time. The collected SWNT films can be transferred to arbitrary substrates through the dry transfer method, a sonication- and surfactant-free process that could retain the excellent properties of SWNTs.

### 3.2.2 Fabrication of SWNT/Si Solar Cells

The as-synthesized SWNT films collected on the filter were subsequently dry-transferred to fused quartz substrates and densified by drop-casting approximately 20  $\mu$ L of ethanol and drying in the ambient environment. From the optical image shown in **Figure 3- 1 (a)**, it can be observed that the SWNT film is highly transparent and uniform. The SEM (Hitachi S-4800) images of the corresponding SWNT films at low and high magnifications are shown in **Figure 3- 1 (b)**. The SWNT films are well percolated with predominately Y-junction inter-tube contact, which would facilitate the carrier transport between SWNTs [37]. Different from the films prepared by

filtration method, the SWNTs used in this study has very long bundle length averaged 9.4  $\mu\text{m}$ . The Raman spectra were measured on a thicker SWNT film to obtain stronger signals. As shown by the Raman spectra (Renishaw inVia) in **Figure 3- 1 (c)**, the SWNT films have very high crystallinity with the G/D ratio over 30. The radial breathing modes (RBMs) of the Raman spectra under the excitation laser wavelength of 488, 532, 633 and 785 nm are also shown in **Figure 3- 1 (c)**. The peak RBM intensity positions locate at ca. 120  $\text{cm}^{-1}$  to 130  $\text{cm}^{-1}$  for all the laser excitation, thus the mean diameter of the SWNTs is estimated as 2.0 nm  $\sim$  2.1 nm. The mean diameter is further confirmed by the  $E_{11}$  position ( $\sim$ 2400 nm) from the transmittance spectrum in **Figure 3- 1 (d)**.

Because no surfactant was used nor sonication process was involved during the film preparation, the high crystallinity, good inter-tube contact and very long bundle length of the SWNTs are well retained. This leads to the high optical transparency and electrical conductivity of the SWNT films as well as the good contact with other materials simultaneously. The sheet resistance (Agilent 4156C; Kyowa-Riken K89PS) and the transmittance (Shimadzu UV-3150) measured at the wavelength of 550 nm (550 nm is the wavelength that has the highest spectral irradiance over the AM1.5G spectrum shown in **Figure 3- 1 (d)**) for all the pristine SWNT films are listed in Table 3-1. The TCF samples with the transmittance of around 70%, 80% and 90% are labeled as TCF70, TCF80 and TCF90, respectively. The sheet resistance was measured by a four-point probe method, and calculated by averaging the values measured from -0.5 V to 0.5 V with a measurement step of 5 mV. Table 3-1 shows that, among the randomly oriented pristine SWNT films reported so far [13, 17, 38], the SWNT films used in this study possess the best transparency and conductivity with very high SWNT crystallinity.

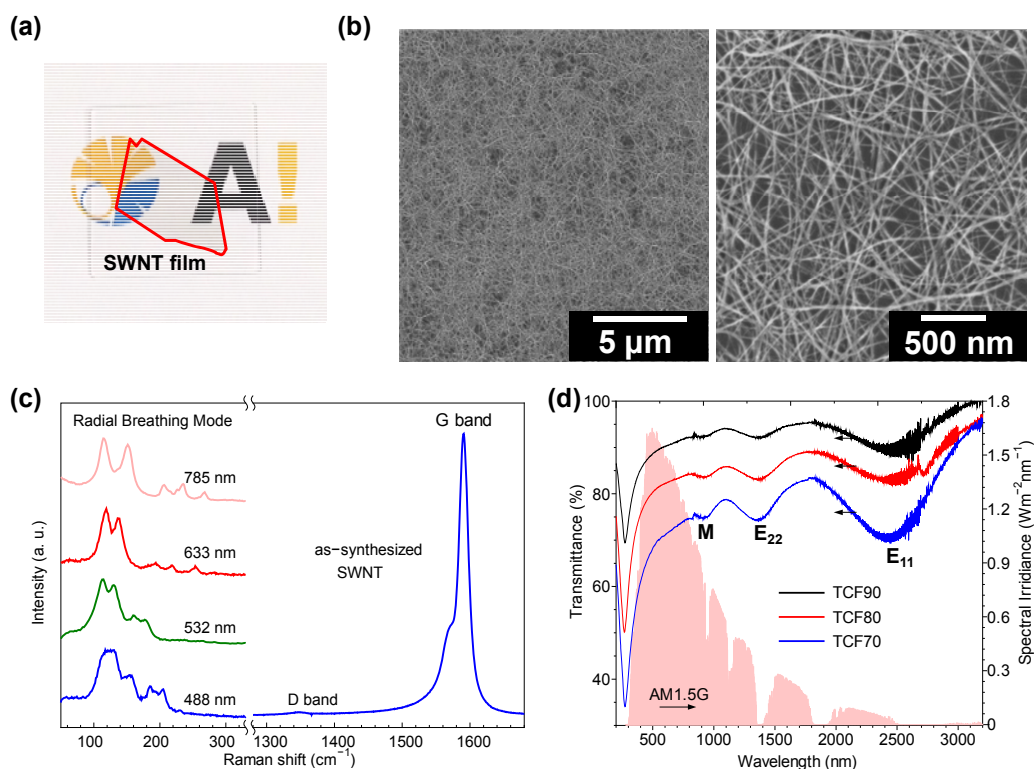


**Figure 3- 1** (a) An SWNT film on the fused quartz substrate after the dry-transfer process. (b) The SEM images at the low and high magnifications of the SWNT film from (a). (c) Raman spectra of the SWNT film under the laser excitation with the wavelength of 488 nm, 532 nm, 633 nm and 785 nm. (d) Transmission spectra of the TCF70, TCF80 and TCF90 SWNT films over the wavelength range of 200 nm to 3200 nm, with AM1.5G irradiance spectrum.

Each SWNT/Si solar cell was fabricated by transferring the SWNT film onto a designed substrate, which was composed of a 3 mm × 3 mm n-type Si contact window and surrounding electrodes. The n-type Si (SUMCO Inc.) has the series resistance of  $10 \pm 2.5 \Omega/\text{cm}$  with the dopants concentration of  $\sim 10^{15} \text{ m}^{-3}$ . The fabrication process of the Si substrate for the SWNT/Si solar cell is given in **Figure 3- 2 (a)**. Before the metal deposition, the n-type Si substrate was consequentially treated with RCA1 ( $\text{H}_2\text{O} : \text{NH}_4\text{OH} : \text{H}_2\text{O}_2 = 5 : 1 : 1$ ), 5 M NaOH and RCA2 ( $\text{H}_2\text{O} : \text{HCl} : \text{H}_2\text{O}_2 = 5 : 1 : 1$ ) solution for 10 min, 40 min and 5 s, respectively, for the removal of organics, oxide layer and impurity metals. After the cleaning treatment, a very thin

oxide layer was formed with the thickness of  $6 \text{ \AA} \sim 7 \text{ \AA}$ , according to the Si  $2p$  spectrum measured by the X-ray photoelectron spectroscopy (XPS, PHI 5000 VersaProbe). The  $3 \text{ mm} \times 3 \text{ mm}$  physical masks were patterned on the top surface of the Si substrate before the metal deposition. A 200-nm-thick  $\text{SiO}_2$  insulator layer and a 50-nm-thick Pt electrode were subsequently RF-sputtered (ULVAC-RIKO, Inc.) on the top surface of the Si substrate. Ti with the thickness of 10 nm was selected as the back electrode for the lineup of the band structure. The SWNT films were transferred using a dry-transfer method onto the top surface of Si substrate after the removal of the physical masks. The schematic of the fabricated SWNT/Si solar cell with dimensional parameters is shown in **Figure 3- 2 (b)**. Part of the SWNT film with the width of 300 nm was suspended between the Pt electrode and the Si substrate, as shown in **Figure 3- 2 (c)**, owing to the stair formed by the  $\text{SiO}_2$  insulator and the Pt electrode layers. The size of the suspended region can be ignored in comparison with that of the SWNT/Si contact window.

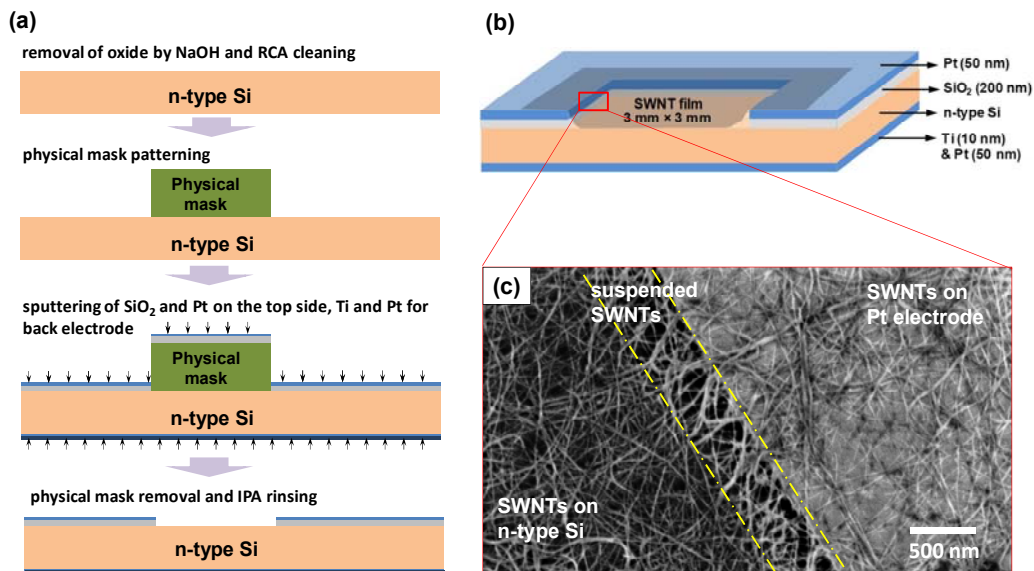


**Figure 3- 2 (a)** Fabrication process of the *n*-type Si substrate for the SWNT/Si solar cell. **(b)** Schematic of the SWNT/Si solar cell with dimensional parameters. **(c)** Magnified SEM image of contact window edge of the SWNT/Si solar cell. A region of the SWNT film with the width of 300 nm was suspended between the Si substrate and the Pt electrode.



**Table 3- 1 Optical transmittance (at the wavelength of 550 nm) and sheet resistance (averaged values) of TCF70, TCF80 and TCF90 samples.**

<i>SWNT films</i>	<i>Transmittance (%)</i>	<i>Sheet Resistance (<math>\Omega/sq.</math>)</i>
TCF70	70.0	85
TCF80	81.5	134
TCF90	88.8	417

### 3.3 Air-Stable SWNT/Si Solar Cells with Record-High Efficiency

#### 3.3.1 Current Density-Voltage Characteristics

The current density-voltage ( $J$ - $V$ ) characteristics of the SWNT/Si solar cells using the TCF70, TCF80 and TCF90 films were measured under AM1.5G 100 mW/cm<sup>2</sup> illumination (PEC-L01, Peccell Technologies, Inc.) as shown in **Figure 3- 3 (a)**. The obtained peak PCE values for the solar cells with the TCF70, TCF80 and TCF90 SWNT films are 9.2%, 10.8% and 10.1%, respectively. The PCE of the solar cell using the TCF80 film is the highest among the pristine SWNT/Si solar cells reported so far, and is comparable to the SWNT/Si solar cells doped with nitric acid and/or gold salt in the previous literatures [25, 27, 33, 39, 40]. The superiority of PCE over the previous reports is attributed to the well-retained high crystallinity, long tube length of the SWNTs as well as the sound inter-SWNT and SWNT-Si contact. The open-circuit photovoltage ( $V_{oc}$ ), short-circuit photocurrent ( $J_{sc}$ ), fill factor (FF) and PCE values of the fabricated solar cells are listed in Table 3-2. The  $J_{sc}$  values of the solar cell samples with the TCF70, TCF80 and TCF90 films were 25.7, 29.7 and 30.9 mA/cm<sup>2</sup>, respectively. Theoretically, higher transmittance would allow more solar irradiation on the SWNT/Si interface, hence the higher photocurrent. However, the photocurrents of the fabricated solar cells do not vary linearly with the transparency of the SWNT films. This could be attributed to the less contribution from the SWNTs part, owing to the decreased light absorbance of SWNTs. In addition, the energy loss

from the light reflection of the mirror-like Si surface becomes notable and increases with the the increase of the transparency of the SWNT film.

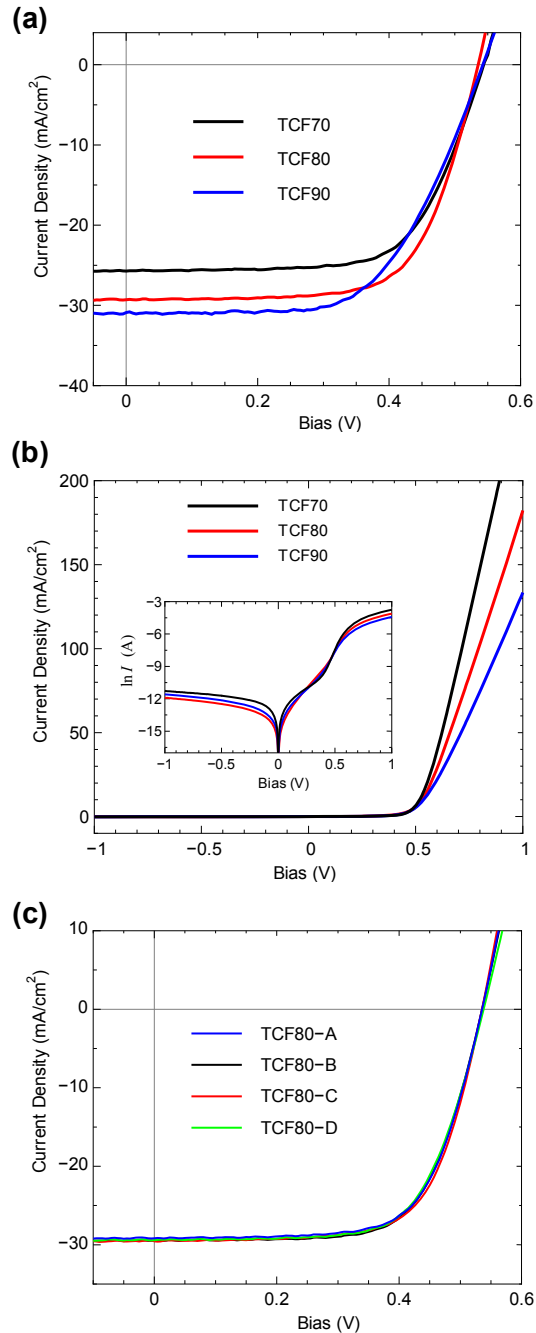


**Figure 3- 3 (a) Representative J-V characteristics of the SWNT/Si solar cells with the TCF70, TCF80 and TCF90 films under 100 mW/cm<sup>2</sup> AM1.5G illumination. (b) J-V characteristics of the SWNT/Si solar cells under the dark condition. (c) Reproducibility of J-V characteristics of four solar cell samples with the TCF80 films fabricated in the same batch.**

The  $J$ - $V$  characteristics of the SWNT/Si solar cells under the dark condition are shown in **Figure 3- 3 (b)**. The rectification ratio of 1 V to -1 V is more than  $\sim 2 \times 10^3$ , which demonstrates the excellent diode behavior of the SWNT/Si junction. As shown in the inset of **Figure 3- 3 (b)**, the ideality factors are calculated as the slopes of the  $J$ - $V$  curves in the logarithm scale ranging from 0.4 V to 0.6V, which are 1.7, 2.1 and 2.2 of the solar cells using the TCF70, TCF80 and TCF90 films, respectively. Moreover, in order to test the reproducibility of the fabricated solar cell, four solar cell samples using the TCF80 films, *i.e.*, TCF80-A, TCF80-B, TCF80-C and TCF80-D, were compared in **Figure 3- 3 (c)**. The uncertainties of the  $V_{oc}$ ,  $J_{sc}$ , FF and PCE are within 2.5 mV, 0.2 mA/cm<sup>2</sup>, 0.005 and 0.15%, respectively, demonstrating the high reproducibility of the solar cell performance. The four above-mentioned solar cell samples used for the comparison are from the same batch. The experimental fluctuations among different batches of fabrication are discussed in Chapter 3.3.3. The high reproducibility of the fabricated SWNT/Si solar cells makes it possible for practical applications.

### 3.3.2 Characterization of Stability in the Ambient Environment

Besides the PCE value, the stability is an important issue for evaluating an emerging solar cell. In this research, we rendered the outstanding chemical stability of the pristine SWNTs to realize a steady and highly efficient solar cell output without any external protection. As shown in **Figure 3- 4 (a)**, the  $J$ - $V$  characteristics underwent almost no change in the ten-month duration in the ambient. Actually, the  $V_{oc}$  values were increased by 13 mV to 550 mV as shown in **Figure 3- 4 (b)**. This can be attributed to the oxygen modification to the SWNT films, which would *p*-dope SWNTs and shift the Fermi level downwards. This would further enlarge the built-in voltage, leading to the increase of  $V_{oc}$ . The charge transfer of the SWNTs and Fermi

level change was confirmed by the weakening of the RBM and the blue shift of G band in the Raman spectra **Figure 3- 5 (a) and (b)**, respectively. In previous literatures, the  $V_{oc}$  value of 550 mV could only be achieved by strong and versatile oxidizing agent, *e.g.* nitric acid, hydrogen peroxide, *etc.*, the doping effect of which last for only few hours. In our study, the mild and stable doping effect from the ambient environment to SWNT films is very suitable for practical applications. This is the only stable over-10%-PCE SWNT/Si solar cell reported so far. The high-quality pristine SWNTs used in the present study are inherently much more stable than sealing techniques such as PDMS coating. Moreover, applying the TiO<sub>2</sub> antireflection layer could harvest up to 30% solar energy which was reflected by the mirror-like Si surface [34, 35]. It is worth mentioning that no external techniques have been employed so far. We believe that a stable and even higher peak PCE would be achieved by utilizing TiO<sub>2</sub> coating technique to the current SWNT/Si solar cells.

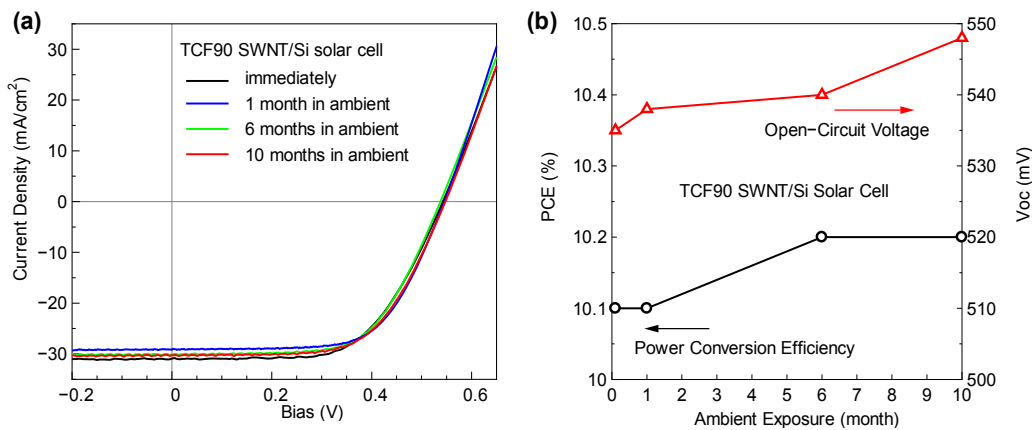


**Figure 3- 4 (a)  $J$ - $V$  characteristics of the SWNT/Si solar cell using TCF90 film measured immediately as well as after 1, 6 and 10 months exposed in the ambient condition. (b) The changes of PCE and  $V_{oc}$  values of the SWNT/Si solar cell using TCF90 film during 10-month ambient exposure.**

Resonance Raman spectra were measured to characterize and compare the as-synthesized SWNTs and the SWNTs exposed in air for six months. The spectra were measured with a 488 nm excitation laser incident normal to the substrate. The

as-synthesized SWNTs have a very high crystallinity with the G/D ratio over 30. After the six-month exposure in air, the intensity of G band of the initial SWNTs was weakened and the peak position of G band was blue-shifted by  $2.1 \text{ cm}^{-1}$  from  $1590.9 \text{ cm}^{-1}$  to  $1593.0 \text{ cm}^{-1}$ , as shown in the inset of **Figure 3- 5 (b)**. This may be attributed to the charge transfer induced by the oxygen exposure during the six months.

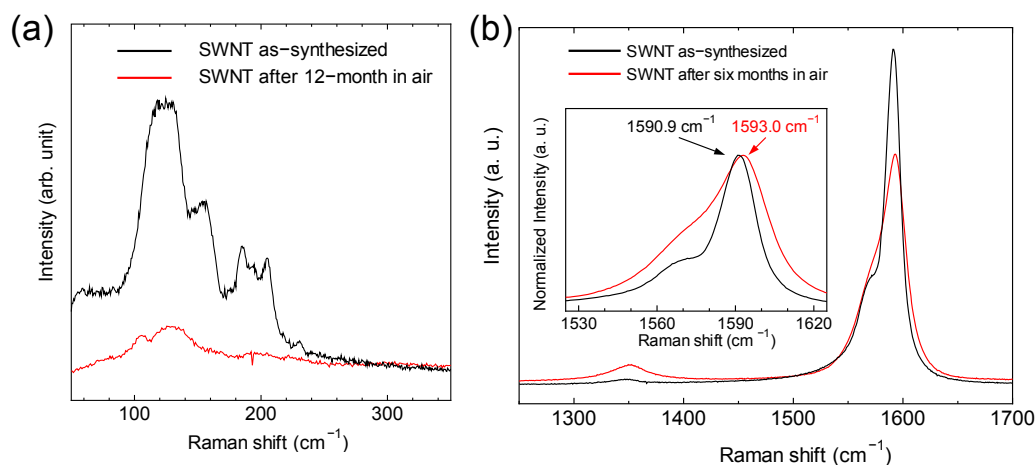


**Figure 3- 5** Resonance Raman spectra of the as-synthesized SWNTs and the SWNTs exposed in air for six months: (a) RBM and (b) G band and D band. The inset of (b) shows the normalized G band. All spectra were measured with a 488 nm excitation laser incident normal to the substrate.

### 3.3.3 Performance Fluctuation of the Solar Cells Fabricated in Different Batches

In the experiments, the experimental uncertainties and fluctuations are inevitable. **Figure 3- 6** shows more than two hundred  $J$ - $V$  curves of the fabricated SWNT/Si solar cells. The stable fabrication process and the uniformity of the SWNT film limit the experimental fluctuations in a very low level. The occurrence probability of the low-quality SWNT/Si solar cells is very small (lower than 10%). Such a high reproducibility is very beneficial for the practical applications of the SWNT/Si solar cells.

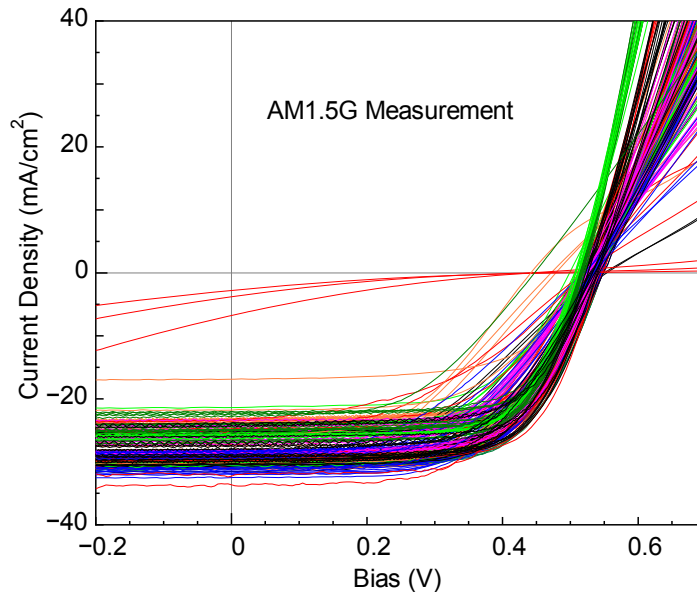


**Figure 3- 6** More than two hundred  $J$ - $V$  curves of the SWNT/Si solar cell samples fabricated in different batches.

## 3.4 Mechanism Discussion of High-Efficiency SWNT/Si Solar Cells

### 3.4.1 Impact of Light Intensity: Experiment and Modeling

In practical applications, the light intensity varies by many factors and is usually lower than  $100 \text{ mW/cm}^2$  used in the standard solar test. The decrease of the light intensity would result in the decreases of  $J_{sc}$  and  $V_{oc}$ . The  $J_{sc}$  varies proportionally to the light intensity and thus will not actually affect the PCE. However, the degradation of  $V_{oc}$  resulted from the decrease of the light intensity will reduce the PCE. Therefore, the  $V_{oc}$  of the solar cell under the light intensity of lower than  $100 \text{ mW/cm}^2$  is another important parameter characterizing the quality of the solar cell. In this research, the dependency of the  $V_{oc}$  of the SWNT/Si solar cells using the TCF90 films on the light intensities was examined. As shown in **Figure 3- 7 (a)**, the  $V_{oc}$  experienced only a

10% drop from 540 to 460 mV (measurement uncertainty was 2.5 mV) when the light intensity decreased from 100 to 10 mW/cm<sup>2</sup>. **Figure 3- 7 (b)** shows the  $J$ - $V$  characteristics of the SWNT/Si solar cell using the TCF90 film measured under the illuminations of 100, 78, 50 and 20 mW/cm<sup>2</sup>. The PCE value of the solar cell only decreased slightly with the decrease of the light intensity, making it suitable for the applications under low light intensities.

The curve fitting to the experimental  $J$ - $V$  characteristics of the solar cells is an insightful method for the in-depth investigation of the solar cell performance. In this research, the equivalent circuit shown in the inset of **Figure 3- 7 (a)** was used to model the  $J$ - $V$  characteristics of the SWNT/Si solar cells. The corresponding  $p$ - $n$  diode equation is expressed as

$$I = I_{sc} - I_0 \exp\left[\frac{q(V + IR_S)}{nkT}\right] - \frac{V + IR_S}{R_{SH}} \quad (3-1)$$

where  $n$  is the ideality factor,  $I_0$  is the dark saturation current which is discussed in Supporting Information S4,  $kT/q$  is the thermal voltage,  $I_{sc}$  is the short-circuit current,  $R_S$  is the series resistance and  $R_{SH}$  is the shunt resistance. When the current  $I$  in the Equation (1) equals zero, the  $V_{oc}$  can be obtained as

$$V_{oc} = \frac{nkT}{q} \ln\left[\frac{I_{sc} - \left(\frac{V_{oc}}{R_{SH}}\right)}{I_0}\right] \quad (3-2)$$

when  $R_{SH}$  is comparable to the  $V_{oc}/I_{sc}$ , an additional loss of the  $V_{oc}$  would be induced under low light intensity. If the  $R_{SH}$  in the Equation (2) is sufficiently large, the ideal  $V_{oc}$  model can be approximated as

$$V_{oc} = \frac{nkT}{q} \ln\left[\frac{I_{sc}}{I_0}\right] \quad (3-3)$$

As shown in **Figure 3- 7 (a)**, the experimental dependency of  $V_{oc}$  on the light

intensities can be well fitted by the ideal  $V_{oc}$  model, which demonstrates that the  $R_{SH}$  of the solar cell is large enough for the light intensities ranging from 100 to 10 mW/cm<sup>2</sup>. Therefore, the SWNT/Si solar cells in this study have sound operation applicability under low light intensities.

Through the curve fitting of the  $J$ - $V$  characteristics of the SWNT/Si solar cells measured under dark current, the dark saturation current  $I_0$  could be obtained. For an actual  $p$ - $n$  diode solar cell, the model of the  $J$ - $V$  characteristics under dark condition is given as

$$I = I_0 \left( e^{\frac{qV}{nkT}} - 1 \right) \quad (3-4)$$

where  $kT/q$  is the thermal voltage which is a constant with the value of 25.85 mV at room temperature;  $n$  is the ideality factor; and  $I_0$  is the dark saturation current. In this research, this  $p$ - $n$  diode equation was utilized to calculate  $I_0$ . The obtained  $I_0$  for the SWNT-Si solar cells using the TCF70, TCF80 and TCF90 films are calculated as  $6.35 \times 10^{-10}$  A,  $1.44 \times 10^{-10}$  A and  $8.47 \times 10^{-10}$  A, respectively.

To further investigate the effects of  $R_S$  and  $R_{SH}$ , the equivalent circuit model was also used to fit the  $J$ - $V$  curves of the fabricated SWNT/Si solar cells measured under different light intensities, aiming at extracting the  $R_S$  and  $R_{SH}$ . As shown in **Figure 3- 7 (b)**, the  $J$ - $V$  curves of the SWNT/Si solar cell using the TCF90 film under different light intensities were all well fitted by the  $p$ - $n$  diode solar cell model of Equation (3-1). The obtained  $R_S$  and  $R_{SH}$  of the solar cell using the TCF90 film were calculated as 33.8  $\Omega$  and more than 20 k $\Omega$ , respectively. The curve fitting results of the  $J$ - $V$  characteristics of the SWNT/Si solar cells with the TCF70 and TCF80 films are also shown in **Figure 3- 7 (c)**. The calculated  $R_S$  for the SWNT/Si solar cells using the TCF70 and TCF80 films have the same value of 27.5  $\Omega$ . The obtained  $R_{SH}$  for these two solar cell samples were also more than 20 k $\Omega$ . The obtained  $R_S$ ,  $R_{SH}$  and  $I_0$  for the



SWNT/Si solar cells using the TCF70, TCF80 and TCF90 films are listed in Table 3-2.

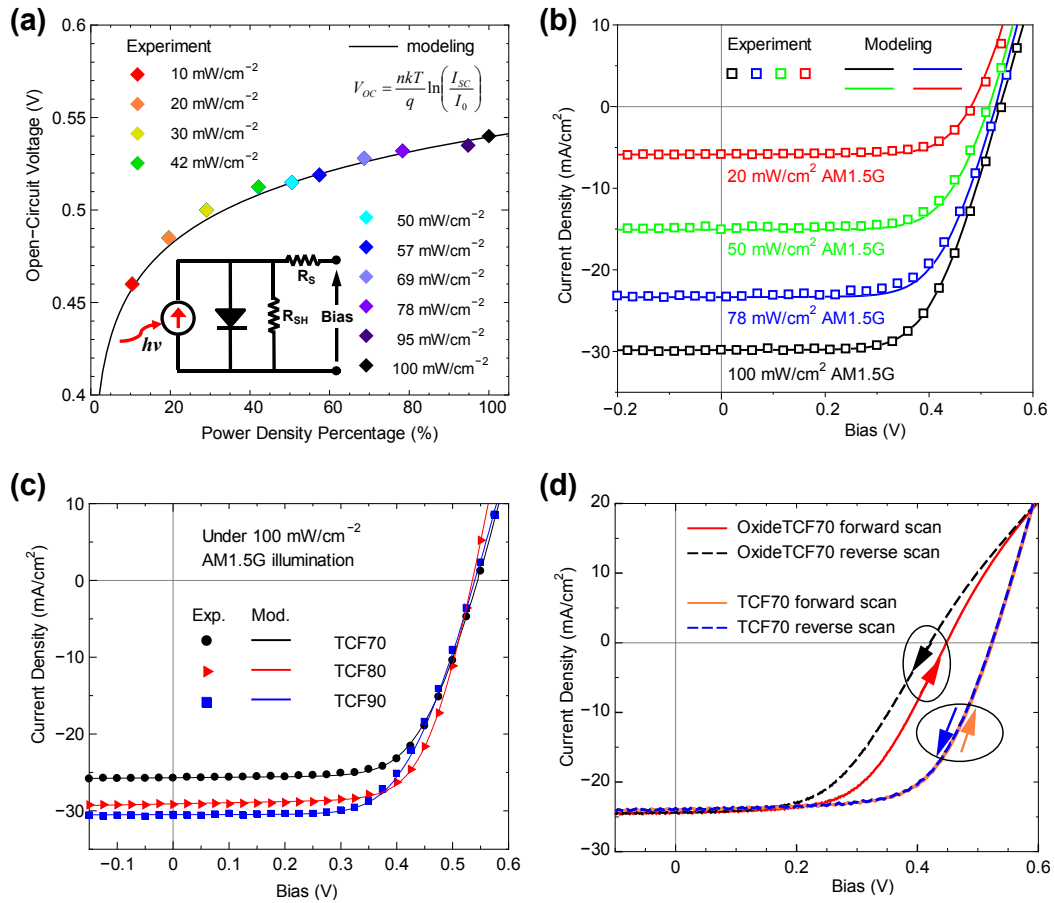


**Figure 3- 7 (a)** The dependency of open-circuit voltage on light intensity. The line is the modeling result of this dependency. The inset is the equivalent circuit of the SWNT/Si solar cells. **(b)**  $J$ - $V$  characteristics of the SWNT/Si solar cells under different light intensities. The symbols denote the experimental results, while the lines represent the modeling results by the  $p$ - $n$  diode equation. **(c)** The curve fitting of the  $J$ - $V$  characteristics of the SWNT/Si solar cells using the TCF70, TCF80 and TCF90 films. **(d)** Hysteresis of the forward and reverse scans for the OxideTCF70 and TCF70 samples which respectively have the oxide layers with the thicknesses of around 15 Å and 7 Å between the SWNT film and Si substrate.

The  $R_s$  and  $R_{SH}$  determine the quality of a solar cell, *i.e.*, FF, which is one of the three parameters characterizing solar cell performance along with  $J_{sc}$  and  $V_{oc}$ . The FF

values for the SWNT/Si solar cells using the TCF70, TCF80 and TCF90 films were 68%, 68% and 61%, respectively. As discussed above, the effect of  $R_{SH}$  on the performance of the solar cells is ignorable. The  $R_S$  is composed of four factors, *i.e.*, the SWNT film-electrode contact, the sheet resistance of the SWNT film, the resistance of Si substrate and the resistance of electrode. Except for the sheet resistance of the SWNT film, the three factors are inherent and can be considered the same in one fabrication batch. As the TCF90 has the highest sheet resistance among all the films, the solar cell using the TCF90 film has lower FF. However, the SWNT/Si solar cells with the TCF70 and TCF80 films have the same  $R_S$  and FF, although the sheet resistance of the TCF70 film is lower than that of the TCF80 film. This suggests that when the sheet resistance of the SWNT film is as low as  $100 \Omega/\text{sq.}$ , the inherent resistance of the solar cell architecture becomes dominant. The FFs of all the solar cell samples using the randomly oriented films in this study were limited to 68%. Previously, we have reported a record-high FF up to 72% using a microhoneycomb-networked SWNTs [41], in which the micro-grids made of dense SWNT walls significantly reduced the carrier diffusion length from millimeter-scale to micrometer-scale. It is expected that applying a special-designed three-dimensional structure to the SWNT films could further increase the FF values.

### 3.4.2 Impact of Interfacial Oxide Layer

We further investigate the effect of interfacial oxide layer on the performance of the SWNT/Si solar cells. The possible mechanisms for the SWNT-Si solar cell are shown in **Figure 3- 8 (a) and (b)**. For the Schottky-barrier Si solar cells, it has been well studied that inserting an oxide layer with the thickness of  $13 \sim 20 \text{ \AA}$  between the metal and semiconductor would improve the solar cell performance by eliminating the pinning of the Fermi level [42, 43]. This theory was used to partially explain the substantial increase of peak PCE by adding nitric acid or other strong oxidants to the SWNT/Si solar cells which were then considered as Schottky-barrier solar cells. In

this study, we designed an experiment to verify this hypothesis. The TCF70 SWNT films were used for fabricating two kinds of SWNT/Si solar cell with different interfacial oxide layer thicknesses, as the TCF70 SWNT film possesses the highest electrical conductivity among all the TCF films used in this research, which could best simulate the metal part in a Schottky solar cell. The two Si substrates with different thicknesses of oxide layers were prepared by varying the treatment time of RCA2 cleaning. The Si substrate treated by the RCA2 solution for 5 s was utilized for the fabrication of the TCF70 solar cell sample which has the above-mentioned performance (**Figure 3- 3 (a) and (b)**), while the Si substrate treated for 3 min was used for the OxideTCF70 solar cell sample (dashed curves in **Figure 3- 7 (d)**). According to the Si 2p XPS spectrum (**Figure 3- 9**), the oxide thickness of the Si substrate for the TCF70 solar cell sample was calculated as 6.9 Å which was approximately the limit of the native oxide layer grown in air [44-46]. In the case of the Si substrate for the OxideTCF70 solar cell sample, the 3-min RCA2 cleaning would leave an oxide layer with the thickness of 13 ~ 15 Å, which has been thoroughly investigated in the previous literatures [42, 43]. As shown in **Figure 3- 7 (d)**, the PCE, FF and  $V_{oc}$  of the OxideTCF70 solar cell sample were significantly lower than those of the TCF70 solar cell sample. The photocurrent degradation near the  $V_{oc}$  is attributed to the increase of series resistance between the SWNT film and Si substrate. Moreover, in the case of the OxideTCF70 solar cell, the thick oxide layer between the SWNT film and the Si substrate serves as a dielectric capacitor. The hysteresis between the forward and reverse scans of OxideTCF70 solar cell sample results from the charging and discharging of the dielectric layer. This experimental result serves as an indirect evidence of the insufficiency of the MIS mechanism for the SWNT/Si solar cells fabricated in this research. The SWNT/Si solar cell is different from the conventional metal-insulator-semiconductor (MIS) junction.

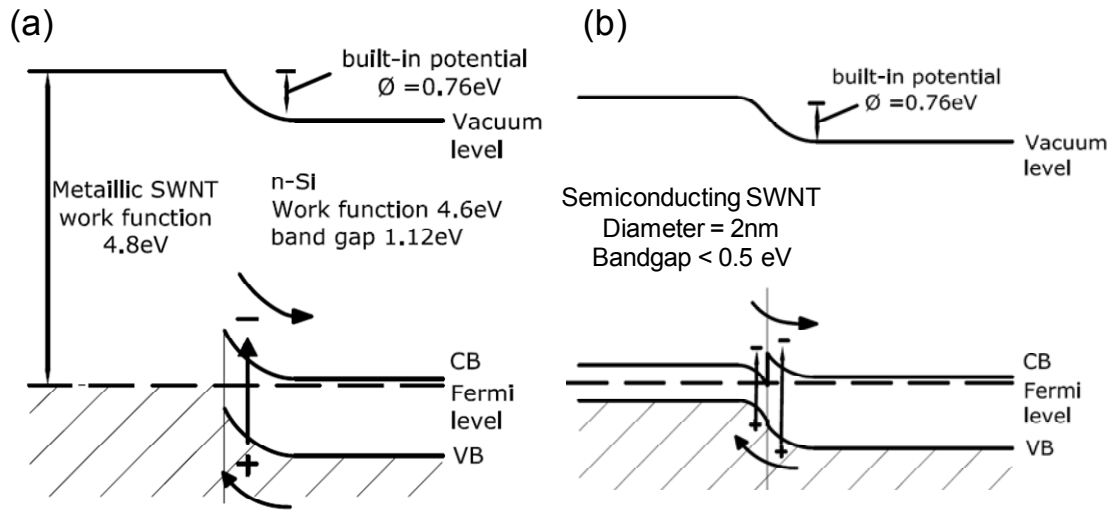


**Figure 3- 8 Possible mechanisms for the SWNT-Si solar cell: (a) metallic SWNTs and (b) semiconducting SWNTs.**

X-ray photoelectron spectroscopy was employed to characterize the oxide thickness of the Si substrate used in the SWNT/Si solar cells. **Figure 3- 9** shows the Si 2p spectrum. The thickness of the oxide layer  $d_{ox}$  could be precisely calculated as

$$d_{ox} = \lambda_{ox} \sin \theta \ln \left( \frac{I_{ox}}{\beta I_{Si}} + 1 \right) \quad (5)$$

where  $\lambda_{ox}$  is the attenuation length of the Si 2p photoelectrons in  $\text{SiO}_2$ ,  $\theta$  is the photoelectron take-off angle,  $\beta$  is the Si 2p intensity ratio of infinitely thick  $\text{SiO}_2$  and Si ( $I_{oxide}^{\infty} / I_{Si}^{\infty}$ ), and  $I_{ox} / I_{Si}$  is the intensity ratio of the measured  $\text{SiO}_2$  layer and the Si substrate.<sup>S1</sup> In this research, the photoelectron take-off angle  $\theta$  is  $\pi/4$ ,  $\lambda_{ox}$  and  $\beta$  are well-studied constants and referred from Ref. [44]. The calculated thickness of the oxide layer is 6.9 Å. This oxide layer is slightly thinner than the native oxide grown in air.

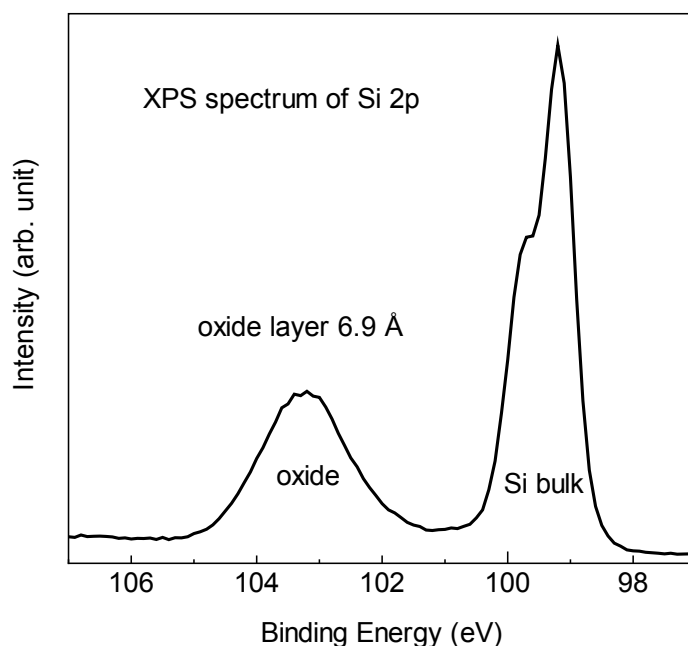


Figure 3- 9 X-ray photoelectron spectrum of the Si substrate used in the SWNT/Si solar cell.

Table 3- 2 The power conversion efficiency (PCE), fill factor (FF), short-circuit current ( $J_{sc}$ ) and open-circuit voltage ( $V_{oc}$ ) of the SWNT/Si solar cells with the TCF70, TCF80 and TCF90 films measured immediately after fabrication, and those of the solar cell with TCF90 film measured 10 months after fabrication, as well as the series resistance ( $R_S$ ), the shunt resistance ( $R_{SH}$ ) and dark saturation current ( $I_0$ ) through  $p$ - $n$  diode equation modeling.

Films	Experimental Results					Modeling Results		
	Time of Measurement	PCE (%)	FF (-)	$J_{sc}$ (mA/cm <sup>2</sup> )	$V_{oc}$ (mV)	$R_S$ ( $\Omega$ )	$R_{SH}$ (k $\Omega$ )	$I_0$ (pA)
TCF70		9.3	0.68	25.7	535	27.5	>20	635
A	Immediately	10.6	0.68	29.3	535	-	-	-
B		10.7	0.67	29.6	535	-	-	-
C		10.8	0.68	29.7	535	27.5	>20	144
D		10.6	0.67	29.6	535	-	-	-
TCF90		10.1	0.61	30.9	535	33.8	>20	847
	10 Months	10.2	0.62	30.3	549	-	-	-

### 3.5 Summary

We have demonstrated the air-stable SWNT/Si solar cells with PCE approaching 11% for the first time. The PCE of the solar cell slightly increases after 10-month ambient exposure. Compared with previously reported results, the fabricated solar cells show a significantly higher stability. The experimental results are well fitted by the  $p$ - $n$  diode equation model and the mechanisms of the improved performance of the SWNT/Si solar cells are discussed accordingly. We believe that the full exploitation of the superior electrical, optical and chemical properties of SWNTs is very promising for the next generation photovoltaic devices.

## **Chapter 4**

# **Microstructure Control of SWNTs for Solar Cell Applications**

SWNT is one-dimensional material of which the lattices extend only along one axis. This characteristic exerts quantum confinement on the radial direction, making individual SWNTs quantum wires. Therefore, SWNTs are featured with outstanding electronic, optical, mechanical and thermal properties at the nanometer scale and are powerful building block for next-generation electronic and photonic devices. However, unlike the conventional semiconducting or metallic materials, such as Si, GaAs or *etc.*, of which the lattices could naturally grow in three dimensions to macroscale monolithic, a single SWNT molecule cannot become a bulk. Therefore, the reasonable construction of SWNTs is necessary for device applications.

In fact, the properties of SWNTs degraded orders of magnitude when SWNTs aggregated in lumps without any structure control. For example, the individual SWNT is one of materials that have the highest thermal conductivity [14, 47-49] theoretically, however, the thermal conductivities of random-built three-dimensional CNT bulks are only one-thousandth of their theoretical values, which is simply calculated by the product of the thermal conductivity of an individual CNT with their volume fraction [50]. The CNTs are excellent thermal conductor at the nanoscale, however, they become an insulator after being randomly built into three dimensions. The same phenomenon applies for electrical conductivity. Moreover, for the application of transparent conductive films, there is always a trade-off between the transparency (transmittance at 550 nm wavelength, which is the strongest intensity among the solar irradiance) and the sheet resistance (electrical conductivity). The higher transparency means less SWNTs are connected together, hence the larger resistance. The most common morphology for the SWNT film is random-oriented network, with the state-of-the-art sheet resistance much higher than ITO at 90% transparency. Carefully designed morphology of SWNTs provides an alternative to efficiently organize the charge generation, separation and transport at solar-cell interfaces.

This chapter will discuss the structure control of SWNTs at the micrometer scale. The microstructure control will build a bridge connecting the excellent nanoscale properties and practical applications. A broader background would be provided first, followed by the newly proposed water vapor treatment in this project. The difference in terms of electrical and optical properties resulted from the structure control would also be examined. Finally, the SWNT/Si solar cell were fabricated and characterized to compare their performance with randomly oriented films.



## 4.1 Research Background and Literature Review

The research of the assembly of nanomaterial came along together with the advent of nanoscience and nanotechnology. Intensive investigations have been focused on the macroscopic architecture of the one-dimensional building block, *e.g.* nanowires, nanopillars, metal oxide nanotubes, MWNT, SWNT, *etc.* Self-assembly is a low-cost and efficient method that builds low-dimensional materials into three-dimensional micro/macro-architectures with various morphologies. Capillary forces have been used to direct the self-assembling of patterned arrays of nanowires [51], nanopillars [52] and multi-walled carbon nanotubes (MWNTs) [53-58] into hierarchical networks. As shown in **Figure 4- 1**, the polymeric nanobristle is self-assembled from patterned arrays by the evaporation induced capillary forces.

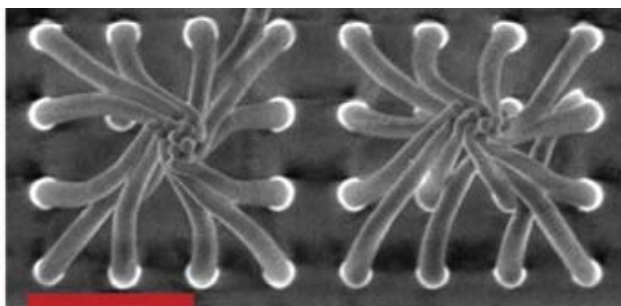


**Figure 4- 1** SEM image of self-assembled polymeric nanobristle by evaporating liquid. From Ref. [52]. Reprinted with permission from AAAS.

The evaporation induced capillary force has been used to direct the self-organization of MWNT since 2004 [58, 59]. MWNTs are somewhat hydrophilic with the water contact angle of 86 °C which is close to graphite [60]. The surface tension of both water and other organic liquid, *e.g.*, ethanol, acetone, IPA *etc.*, during their evaporating process could drive the air in the void of VA-MWNTs away, wet the MWNTs and finally assemble MWNTs together. Assisted with lithographic patterning, various three-dimensional architectures could be realized as shown in **Figure 4- 2**.

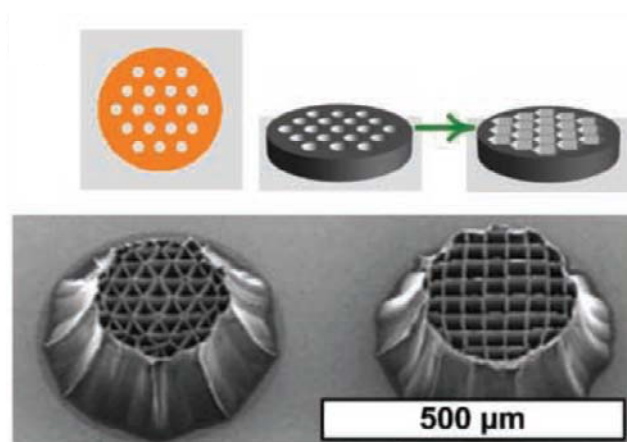


**Figure 4- 2 Mechanism and SEM images of self-assembled multiwalled carbon nanotubes induced by capillary forces. Copyright © 2010 WILEY-VCH Verlag GmbH & Co. KGaA, Weinheim.**

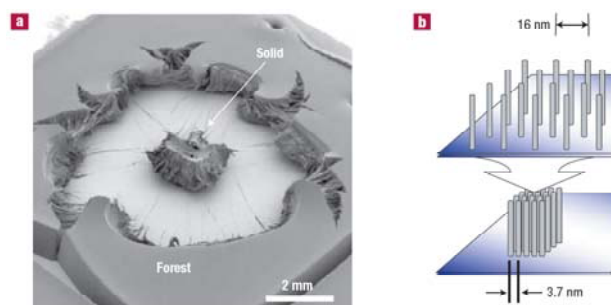


**Figure 4- 3 SEM image (a) and mechanism (b) of collapsing VA-SWNTs induced by capillary forces. Reprinted by permission from Macmillan Publishers Ltd: Nature Materials [57], copyright (2006)**

However, owing to the hydrophobicity and significantly smaller diameter of SWNTs, wetting vertically aligned SWNTs (VA-SWNTs) results in a high-density bulk with millimeter-scale cracks rather than the hierarchical honeycomb-like network formed by MWNT arrays, as shown in **Figure 4- 3**. So far, such a honeycomb structure of SWNTs has been achieved only by film-casting anionic shortened SWNTs–cationic ammonium lipid conjugates in organic solution, of which the complicated solution preparation induces defects and degradation of SWNTs.

## 4.2 Self-Assembly of Vertically Aligned SWNTs

### 4.2.1 CVD Growth of Vertically Aligned SWNTs

VA-SWNTs were synthesized by the standard alcohol-catalytic CVD (ACCVD) method with Co/Mo dip-coated on quartz or Si/SiO<sub>2</sub> substrate [7, 61, 62]. The schematics of ACCVD system is shown in **Figure 4- 4**. The substrate loaded with Co/Mo bimetallic nanoparticle catalyst was placed in a quartz tube surrounded by the electric furnace after the dip-coating process and heated in a reduction environment gradually to 800 °C in 30 min. Then, the substrate was kept at 800 °C for 10 min before ethanol feedstock was introduced with flow rate of 450 sccm at 1.3 kPa. The growth process of VA-SWNTs can be monitored by in-situ laser absorption technique [63, 64] for quartz substrate. The growth process of VA-SWNT on quartz is given in **Figure 4- 5 (a)**. The SEM image of the corresponding VA-SWNTs grown on quartz is shown in **Figure 4- 5 (b)**. The thickness of the VA-SWNT obtained from the in-situ laser absorption technique is consistent to that from the SEM cross-section measurement. With the controlled growth technique, we grow SWNTs on Si/SiO<sub>2</sub> substrate with the length of 5 μm. Moreover, the VA-SWNT films can easily transferred onto any substrate by the hot-water method [65].

By modifying the concentration of Co/Mo acetate solution and carbon stock, as well as substrate and CVD conditions, both the nanoscale and microscale of SWNTs could be controlled to a certain degree, respectively. On the nanoscale, the diameter of SWNTs could be tuned from 2.2 nm to 1.4 nm [66], which could change the band gap of semiconducting SWNTs from 0.5 to 0.8 eV. Through the addition of a certain amount of acetonitrile to ethanol in the carbon stock, the diameter of nanotube could be drastically changed from 2.1 nm to 0.7 nm, respectively [67, 68]. On the other hand, on the microscale, high-precision patterned growth of VA-SWNTs could be realized through tuning surface hydrophobicity of the substrate by the formation and

removal of self-assembled monolayer [69].

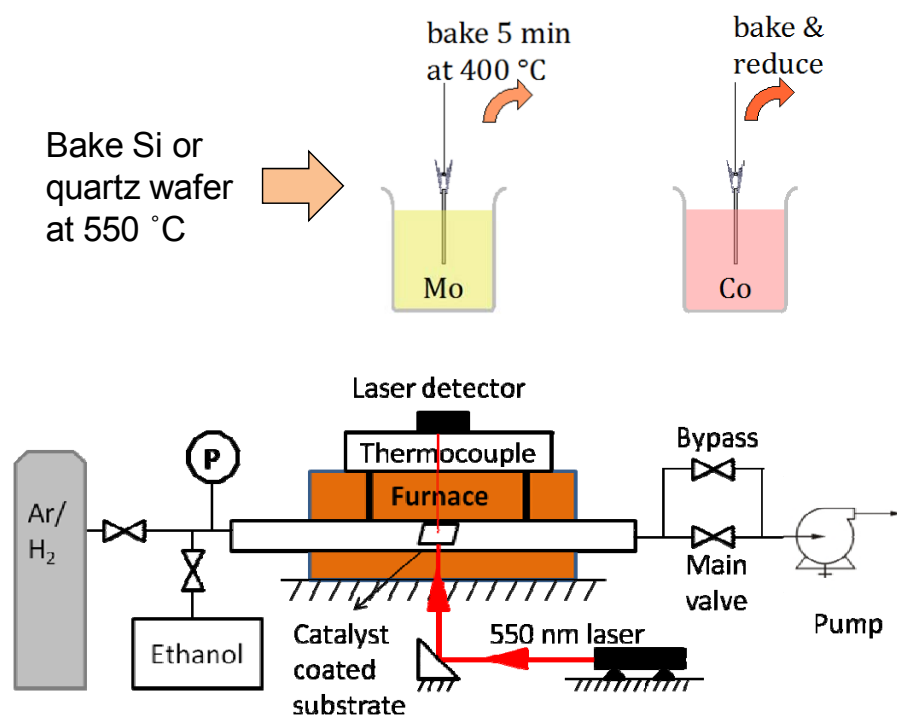


Figure 4- 4 Protocol of CVD growth of vertically aligned SWNTs from alcohol on substrate.

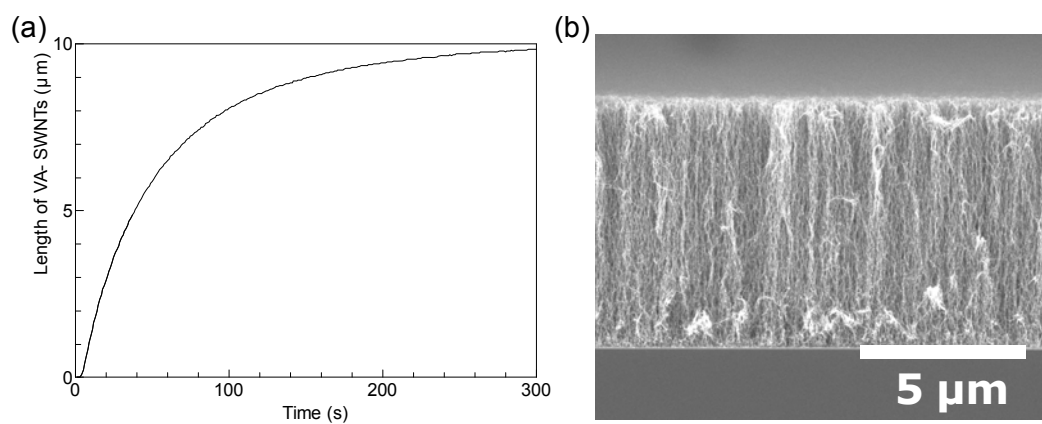


Figure 4- 5 (a) Growth curve of the VA-SWNTs in the ACCVD process by the in-situ laser absorption technique. (b) SEM image of the corresponding VA-SWNTs.

#### 4.2.2 Formation of Micro-Honeycomb Networked SWNT Film

After ACCVD synthesis, the water vapor treatment includes two steps as shown in **Figure 4- 6 (a)**: (1) expose the VA-SWNT array to vapor from a hot water reservoir, and (2) turn the substrate over and dry the array in the ambient environment. The uniform VA-SWNT array (**Figure 4- 6 (b)** and **Figure 4- 7 (a)**) was aggregated into hexagonal frames (intermediate stage shown in **Figure 4- 6 (b)**), after the first water vapor treatment. By repeating this treatment the VA-SWNT array evolved into a  $\mu$ -HN (**Figure 4- 6 (e)** and **Figure 4- 7 (c)**) after 20 to 30 iterations. The liquid-solid interaction induced by the condensation and subsequent evaporation of water is the building tool used to engineer the morphology of VA-SWNTs into a self-assembled  $\mu$ -HN. The  $\mu$ -HN is a hierarchical hexagonal-shaped three-dimensional network (**Figure 4- 6 (c)**) that consists of vertical SWNT walls and a randomly networked SWNT bottom (**Figure 4- 7 (d)**). Each wall is a cross-linked high-density SWNT agglomeration (**Figure 4- 6 (d)**) and the bottom of each honeycomb cell is a randomly oriented buckypaper, which results from the collapse of SWNT alignment. The schematic of  $\mu$ -HN is shown in **Figure 4- 6 (c)**. The most energetically favorable outcome is a honeycomb network because it uniformly divides the region into cells having minimal perimeter, *i.e.*, allows the largest number of SWNTs to collapse.

#### 4.2.3 Cell Size Control of the Micro-Honeycomb Networked SWNT Film

Varying the water reservoir temperature and vapor exposure time of water vapor treatment results in different morphologies. Three typical self-assembled SWNT structures could be obtained,  $\mu$ -HN, collapsed HN and porous HN. The  $\mu$ -HN is obtained by the exposure to vapor from an 80 °C reservoir for 5 s. Extending the exposure time from 5 s to 15 s at the same reservoir temperature would result in the collapse of the walls, hence larger cell sizes. When the exposure time is more than 15

s, nearly all the wall structures disappear and the whole film becomes a collapsed HN. The porous HN is obtained from 5 s vapor exposure to a water reservoir at 70 °C.

The water reservoir temperature and the vapor exposure time are the two dominant factors determining the  $\mu$ -HN formation. As the control, a 10  $\mu$ L water droplet was dropped onto the top surface of a VA-SWNT film at room temperature. After evaporation of the water, the SWNTs had aggregated into a highly condensed bulk and generated many 100  $\mu$ m-scale gaps (**Figure 4- 8 (a)** and **(b)**), which is in agreement with the report by Futaba *et al.* [57]. A similar phenomenon was observed for an ethanol droplet and an 80 °C water droplet. In the case of water vapor treatment, when the water reservoir temperature was increased to 50 °C, the length of the gaps decreased to  $\sim$ 50  $\mu$ m and honeycomb cells started to form (**Figure 4- 9 (a)**). Further increase of the water reservoir temperature to 70 °C significantly reduced the size of the gaps to approximately 5  $\mu$ m, and the size of honeycomb cells became more uniform (**Figure 4- 9 (b)**). A well-formed  $\mu$ -HN was obtained when the water reservoir temperature reached 80 °C (**Figure 4- 9 (c)**). The vapor exposure time for the structures shown in Figures S3a, S3b and S3c was 5 s in all cases.

The effect of vapor exposure time on the morphology was investigated using a constant water reservoir temperature of 80 °C. Extending the exposure time from 2 s to 5 s resulted in an increase in micro-honeycomb cell size from  $\sim$ 2.5  $\mu$ m (**Figure 4- 10 (a)**) to  $\sim$ 12  $\mu$ m (**Figure 4- 10 (b)**). When the exposure time was longer than 15 s, the walls of the cells nearly disappeared, as most of the VA-SWNTs had collapsed as shown in **Figure 4- 10 (c)**. Compared with direct immersion or direct wetting (water droplet) [55, 59], water vapor treatment is a more delicate, controllable method.

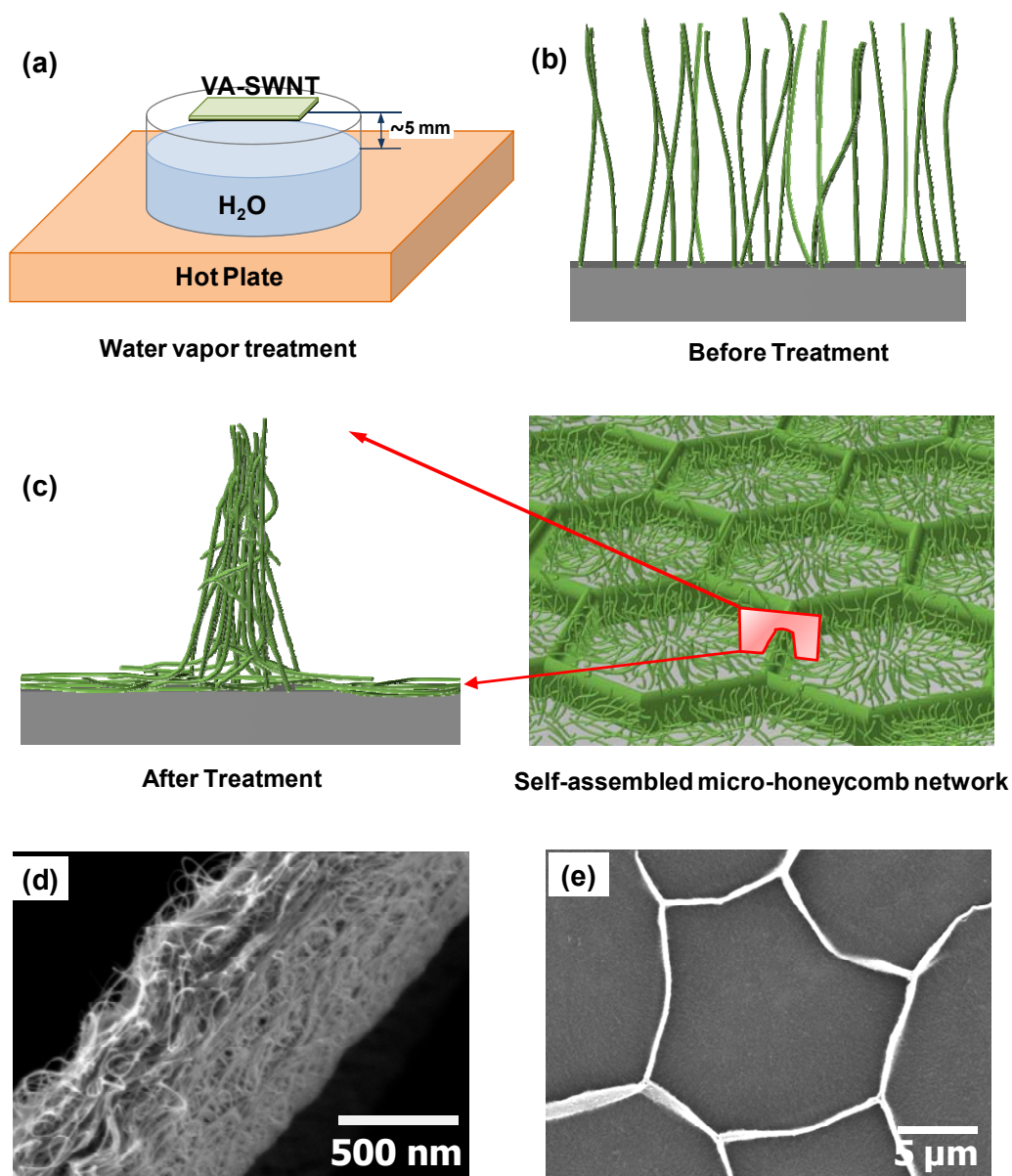
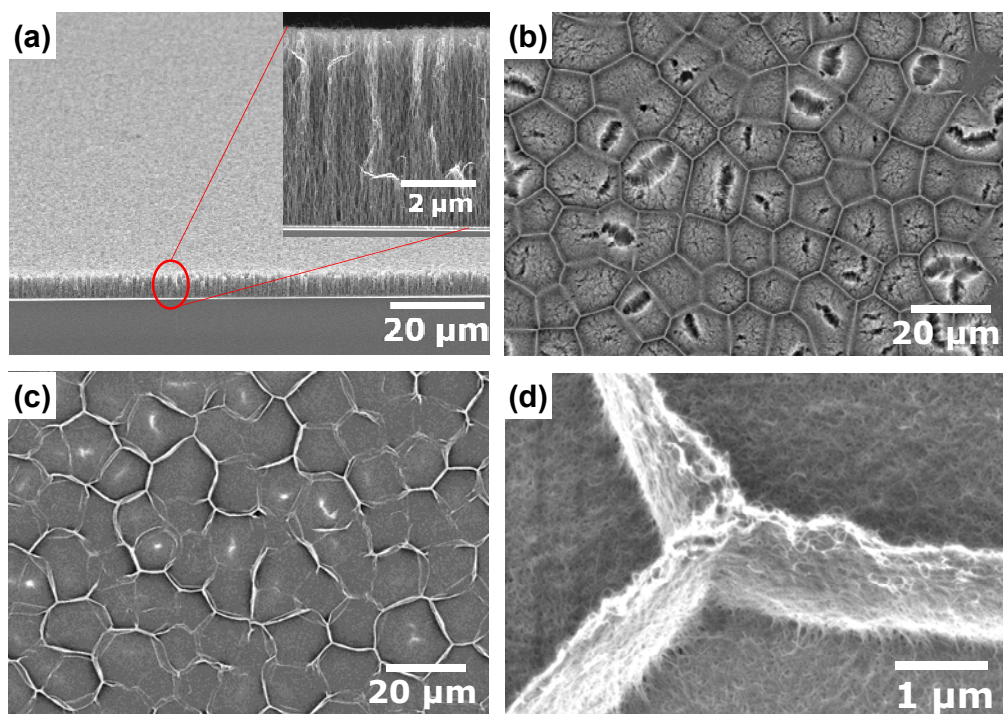
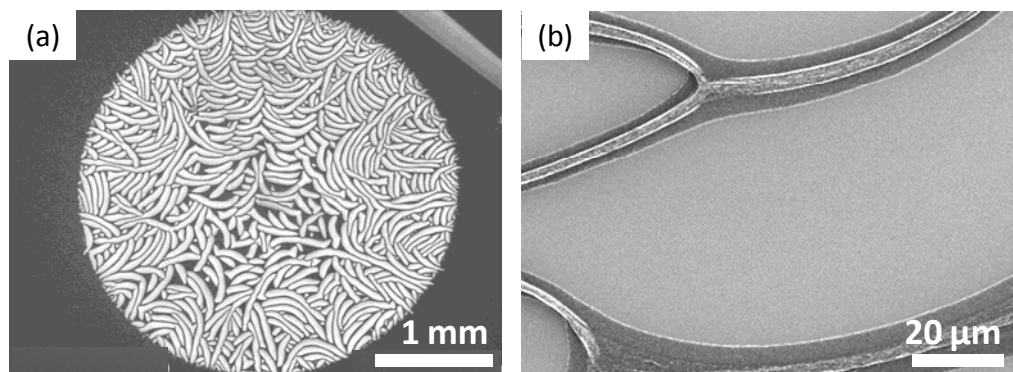


Figure 4- 6 (a) The schematic of the water vapor treatment. (b) The schematic of the as-synthesized uniform VA-SWNT array before water vapor treatment. (c) The schematic of the stable  $\mu$ -HN formed after 20 ~ 30 iterations of the water vapor treatment. (d) The SEM image of a dense SWNT wall of an individual honeycomb cell. (e) The magnified image of the three-dimensional hierarchical  $\mu$ -HN with dense SWNT wall and randomly oriented bottom.



**Figure 4- 7** Water vapor treatment of the VA-SWNT array into a  $\mu$ -HN. (a) Schematic of the water vapor treatment process. (b) As-synthesized high-quality VA-SWNT with a uniform top surface. (c) Intermediate stage of the  $\mu$ -HN formation after the first iteration. (d) Stable  $\mu$ -HN formed after 30 times iteration of the water vapor treatment.



**Figure 4- 8** 100  $\mu$ m-scale gaps obtained by applying a 10  $\mu$ L water droplet to the surface at RT under (a) low magnification and (b) high magnification.



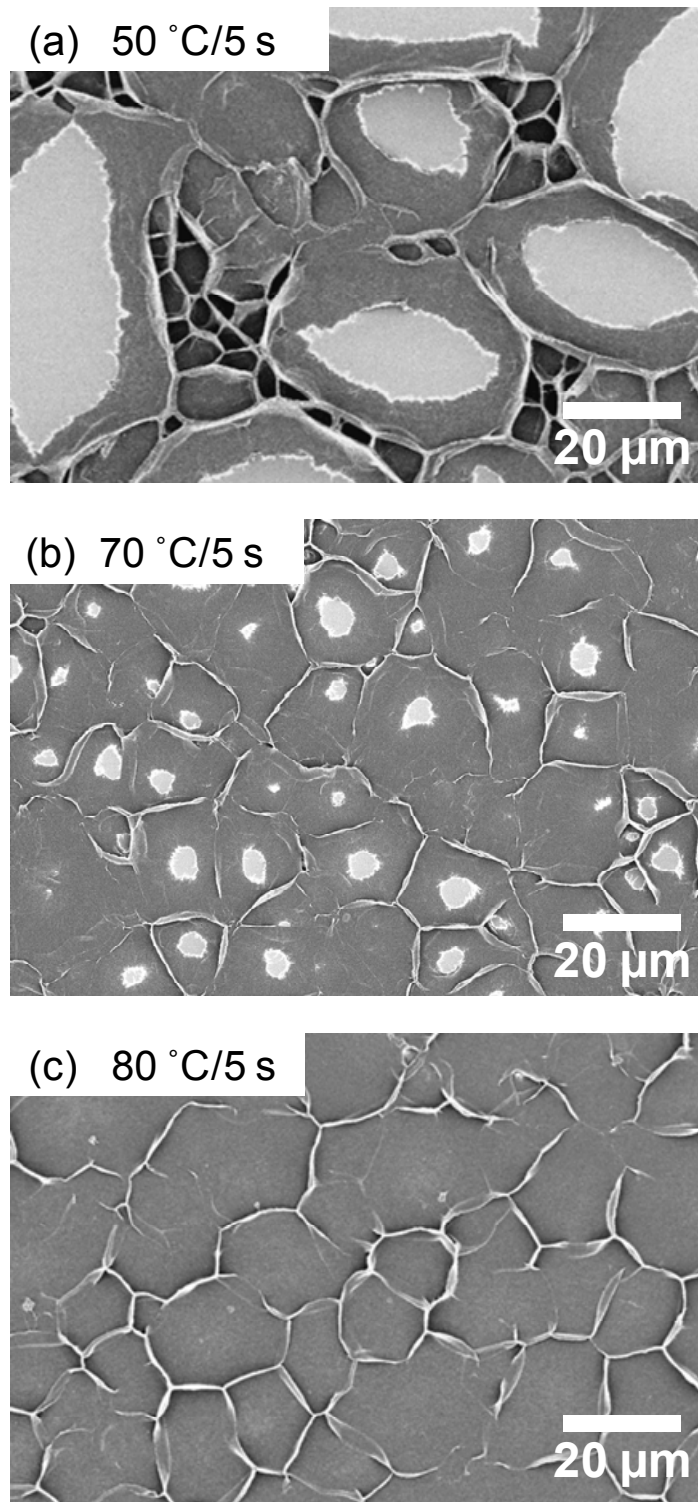


**Figure 4-9 (a-c) Morphologies obtained by exposure to 50 °C, 70 °C and 80 °C water reservoirs, respectively. The vapor exposure time for each vapor treatment step is 5 s.**

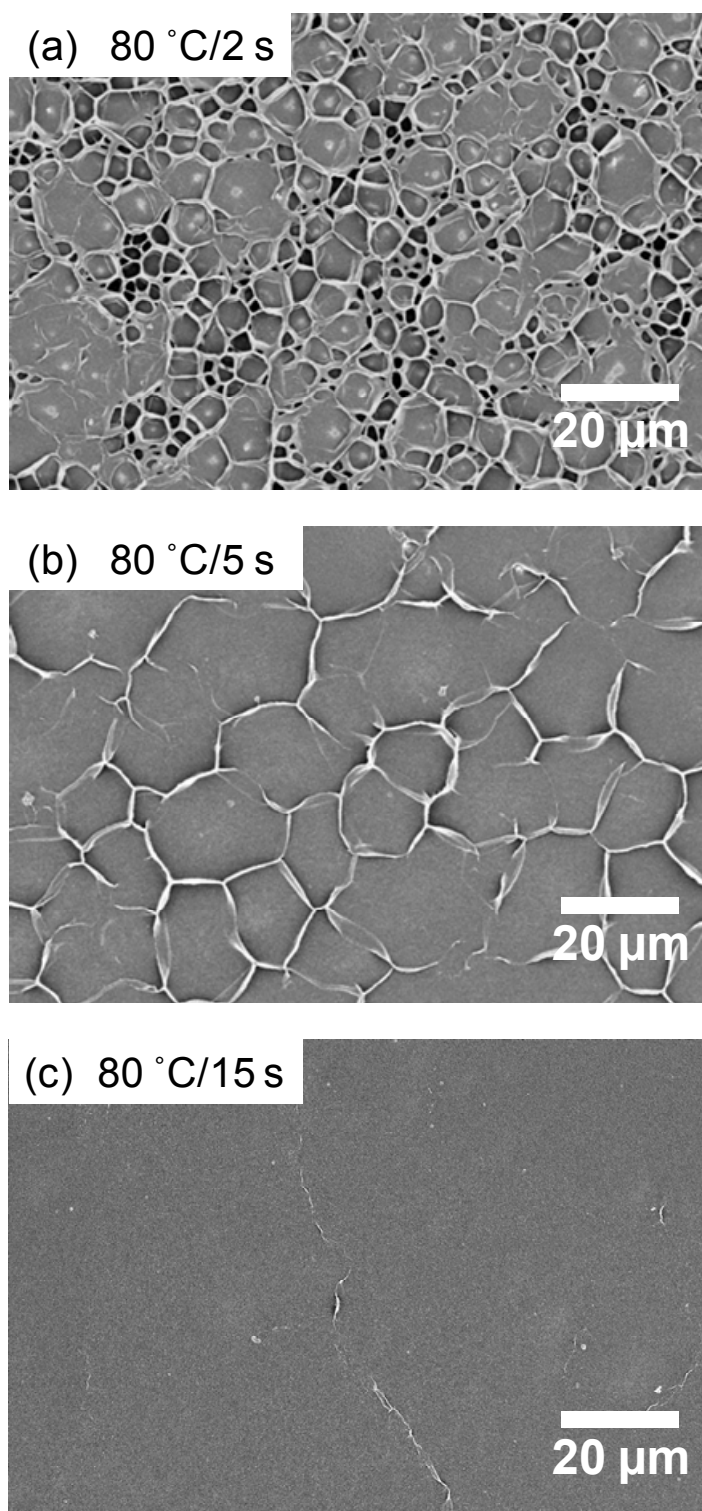


**Figure 4- 10 (a-c) Morphologies obtained with vapor exposure times of 2 s, 5 s and 15 s for each iteration, respectively. Reservoir temperature was 80 °C.**

#### 4.2.4 Breath Figure Mechanism of the Micro-Honeycomb Network

To investigate the mechanism of the formation of the microhoneycomb structure, the ex-situ SEM observation is employed, as shown in **Figure 4- 11**. The samples were dried in air for 20 min after each water vapor treatment to make sure the extra water molecules fully removed. The evolution of the honeycomb is recorded.

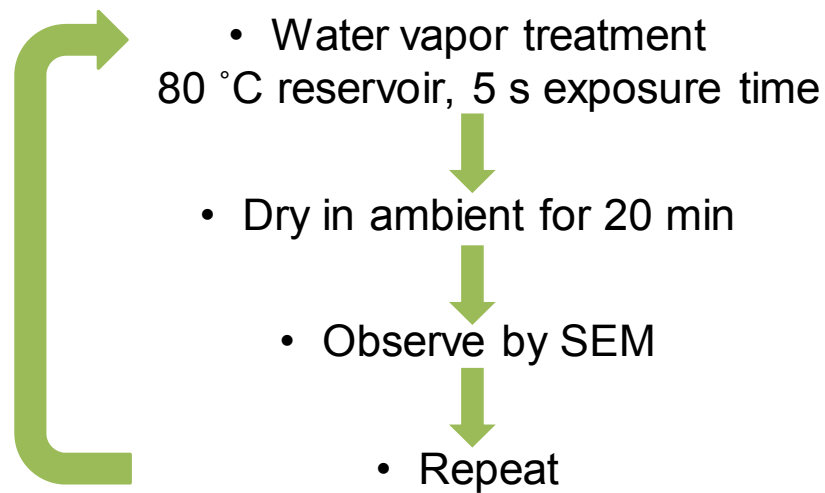


**Figure 4- 11** Flow chart of ex-situ SEM observation of the honeycomb formation process.

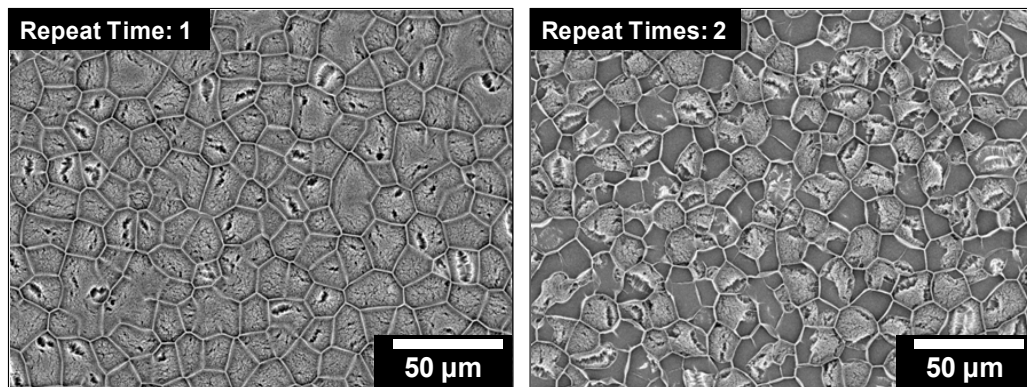


**Figure 4- 12** ex-situ observation of the evolution of the honeycomb structure formation. The left-hand side is the morphology of SWNTs after the first repeat of water vapor treatment and the right-hand side is the morphology of the SWNTs after the second repeat of water vapor treatment.

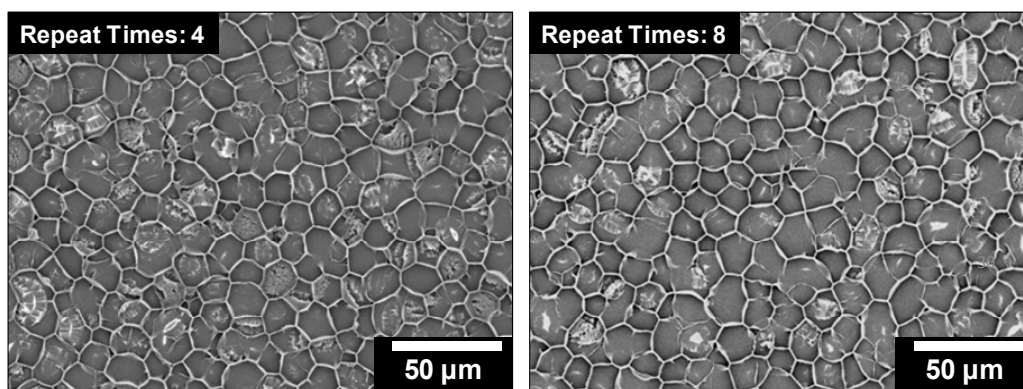


**Figure 4- 13** ex-situ observation of the evolution of the honeycomb structure formation. The left-hand side is the morphology of SWNTs after the four-time repeat of water vapor treatment and the right-hand side is the morphology of the SWNTs after the eight-time repeat of water vapor treatment.

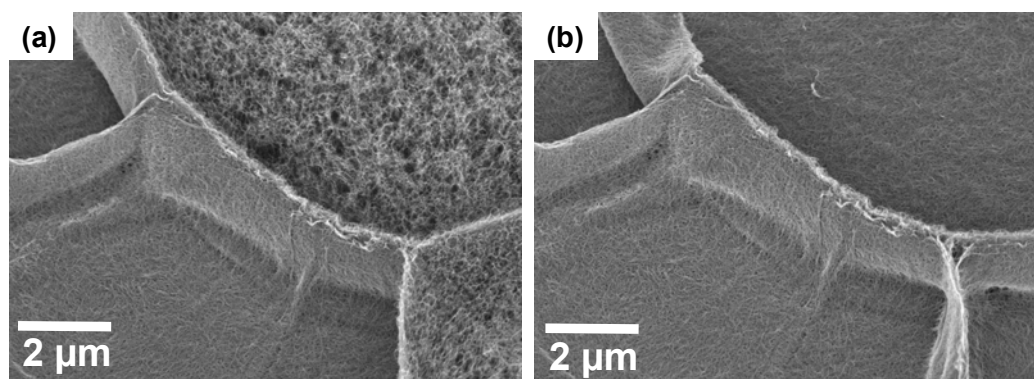


**Figure 4- 14** The captured stochastic process of the formation of microhoneycomb structure, which is resulted from the capillary force of water vapor.

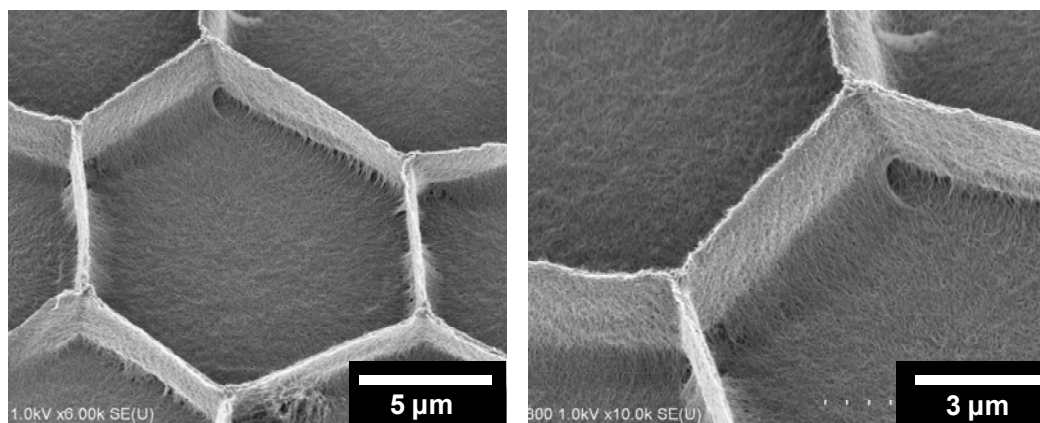


**Figure 4- 15** Magnified SEM image of the hexagonal structure of SWNTs formed by water vapor treatment.

As shown in **Figure 4- 12**, the frame of the honeycomb is formed after the first evaporation. This is very different from the MWNTs which collapsed immediately after any liquid condensation and evaporation. After the second iteration, some SWNTs within the honeycomb frames have been pushed down to the substrate randomly, as shown in **Figure 4- 13**. As the SWNTs synthesized in this research has very high quality and thus high hydrophobicity, the condensation of the water molecules on the surface of VA-SWNTs would result in a breath figure pattern. The breath figure pattern was first discovered by Lord Rayleigh [70], which is originated from the pattern formed when humans breath on the cold surface. Until now the breath figure is still very complicated and interesting subject investigated by physicist [71-73] and chemist [74-76]. In the perspective of physics, the evolution and stability of droplet condensation is critical to enhance the heat transfer efficiency, while in the perspective of chemistry, breath figure could be used to direct the formation of honeycomb structure of polymers which can be used in different applications. In this research, the water vapor condensates on SWNTs surface, which is composed of large amount of flexible, hydrophobic one-dimensional nanomaterials.

Further repeat of this water vapor treatment would result in more SWNTs pushed to the substrate. Essentially, as far as the 5  $\mu$ m thick VA-SWNT is considered, after eight times repeat of water vapor treatment, most of the SWNTs inside the honeycomb cell have been pushed down to the substrate by the breath figure. However, this process is random. Part of the SWNTs happen to be caught under the SEM that the four cells were pushed down after different times of water vapor treatment, as shown in **Figure 4- 14**. The magnified complete honeycomb structure is given in **Figure 4- 15**.

### 4.3 Spectroscopy Characterization of Micro-Honeycomb Networked SWNT Film

#### 4.3.1 Raman Spectroscopy of the Micro-Honeycomb Networked SWNT Film

Raman spectra were measured to characterize and compare the SWNT assemblies before and after water vapor treatment. Spectrum 1 in **Figure 4- 16** corresponds to as-synthesized VA-SWNTs, whereas spectra 2 and 3 were obtained from the highly condensed walls and buckypaper bottom, respectively. Spectrum 1 shows that the D-band is negligible for the as-synthesized VA-SWNTs, indicating the high quality and high purity of as-synthesized VA-SWNTs. Furthermore, the relative D-band intensity was nearly unchanged after water vapor treatment. This illustrates that the water vapor treatment did not induce defects in SWNTs. In the radial breathing mode (RBM) region (the inset of **Figure 4- 16**), spectrum 1 has the characteristic of free-standing SWNTs, with strong peaks appearing at 160 and 181  $\text{cm}^{-1}$ . The two characteristic peaks became much weaker after the water vapor treatment (spectra 2 and 3), owing to the bundling of SWNTs. The reduction in peak intensity was more pronounced in the bottom of the honeycomb cell.

The micro-honeycomb film after nitric acid doping process was also characterized by Raman spectroscopy. The 40  $\mu\text{L}$  diluted nitric acid droplet with 10 M concentration was placed on the surface of the micro-honeycomb SWNT film. Raman spectra in **Figure 4- 17** show a 21  $\text{cm}^{-1}$  upshift in both the G band and the G' band as well as a significant increase in D band intensity. The Raman spectra further prove that the SWNTs samples are heavily *p*-doped [77].

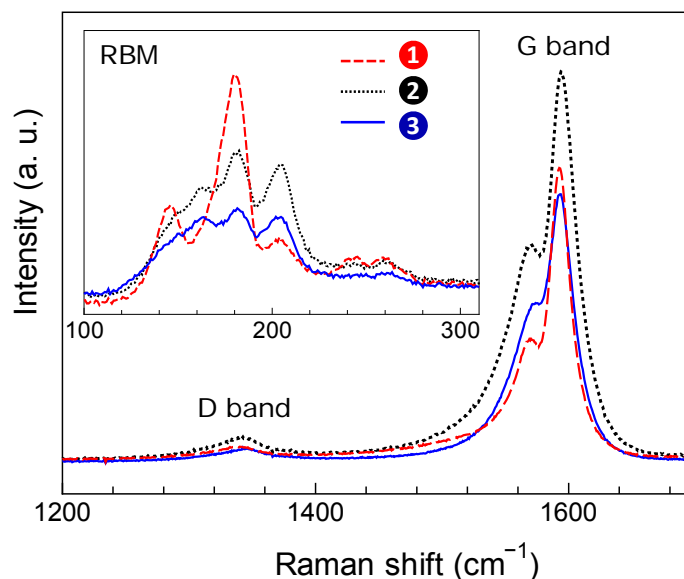


**Figure 4- 16** Resonance Raman spectra of SWNTs before and after water vapor treatment: spectrum 1 corresponds to as-synthesized VA-SWNTs. Spectra 2 and 3 correspond to the wall and bottom of the micro-honeycomb structure, respectively. All spectra were measured with a 488 nm excitation laser incident normal to the substrate.

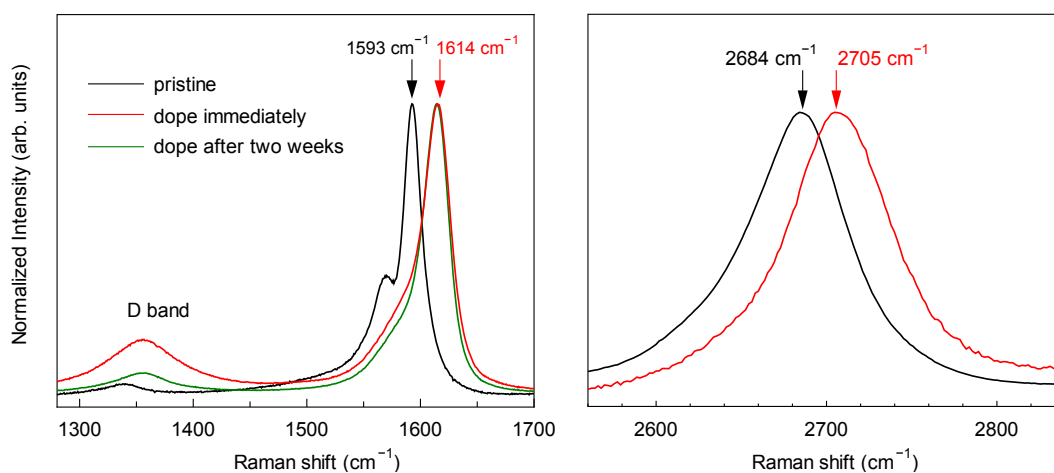


**Figure 4- 17** Raman spectra of pristine and nitric acid treated samples. Spectra of the treated samples were measured immediately after the samples were completely dried.

### 4.3.2 UV-vis-NIR Spectroscopy of the Micro-Honeycomb Networked SWNT Film

The UV-vis-NIR spectra of the microhoneycomb networked SWNTs before and after acid doping are shown in **Figure 4- 18 (a)**. In addition to the charge transfer and the suppressed  $E_{11}$  and  $E_{22}$ , a clear attenuation in the spectra is located at around 1000 nm wavelength, which is not correspond to the van Hove singularities. This phenomenon cannot be observed from the spectra of the randomly oriented SWNT films shown in **Figure 4- 18 (b)**.

The acid doping effect on the VA-SWNTs was investigated to track the origin of the absorption attenuation near 1000 nm. It was found out that attenuation peak was red-shifted with increased doping times (**Figure 4- 19**). The similar but not as pronounced red-shift and attenuation has been reported in [78], as shown in **Figure 4- 20**. The attenuation peak may be attributed to the structure related features.

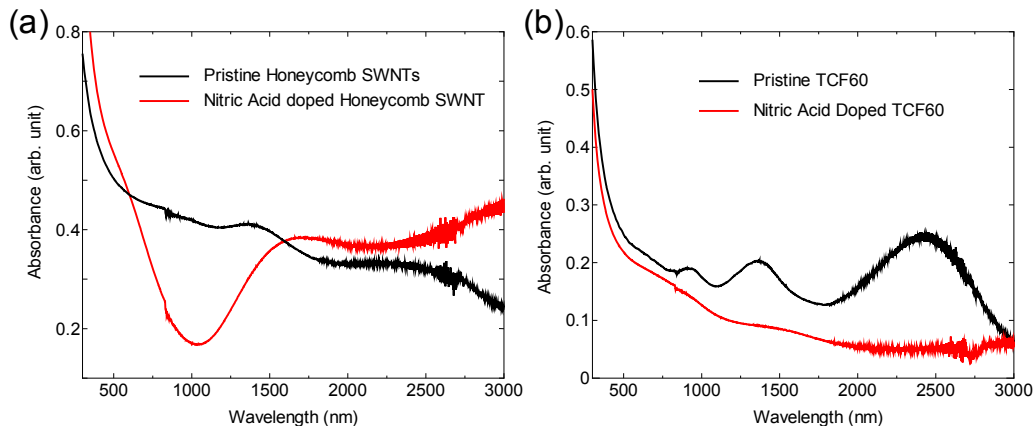


**Figure 4- 18 (a)** UV-vis-NIR absorption spectra of pristine and nitric acid doped SWNTs with micro-honeycomb networked structure. **(b)** UV-vis-NIR absorption spectra of pristine and nitric acid doped random-oriented SWNTs.



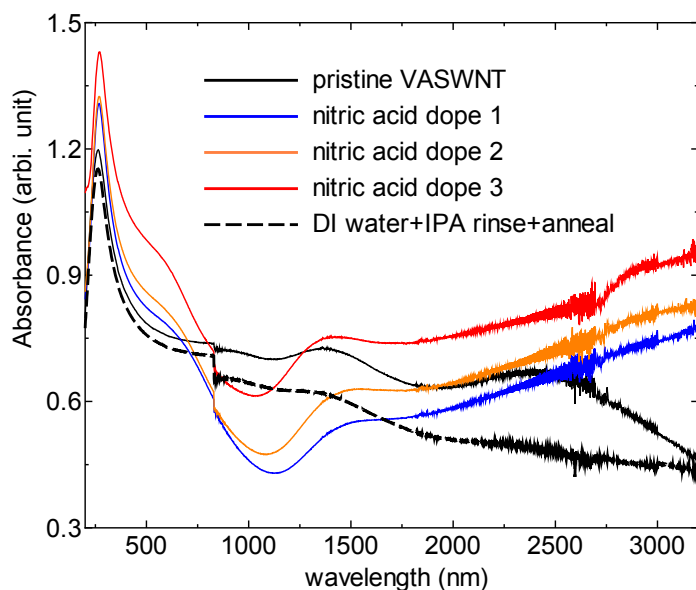


Figure 4- 19 UV-vis-NIR absorption spectra of pristine VASWNT and its change after different times of nitric acid treatment. The absorption spectrum of VASWNT is restored after DI water and IPA rinse followed by Ar anneal.

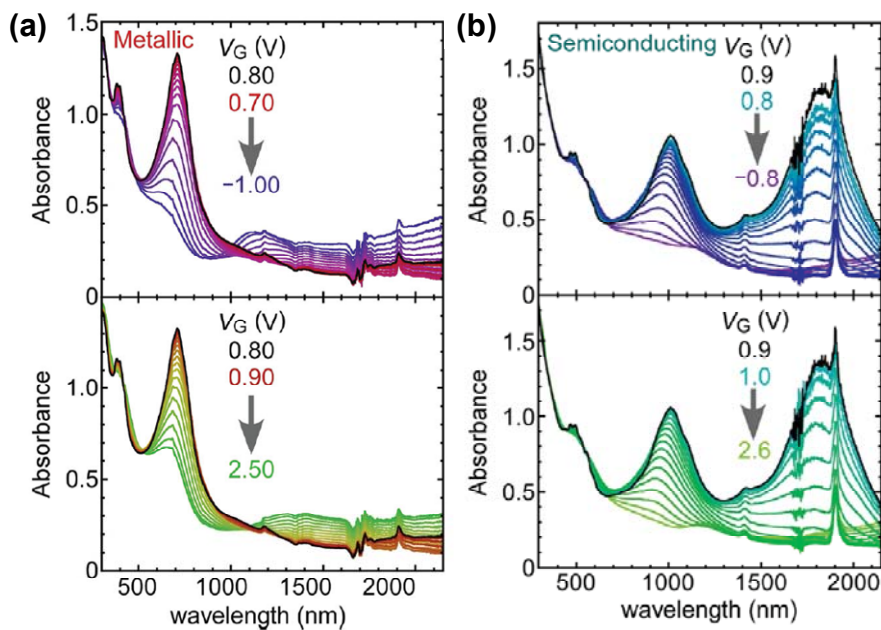


Figure 4- 20 Absorption spectra measured at different gate voltage for (a) metallic SWNTs and (b) semiconducting SWNTs. © 2014 WILEY-VCH Verlag GmbH & Co. KGaA, Weinheim

## 4.4 Micro-Honeycomb Networked SWNT Film for Solar Cells

### 4.4.1 Performance Characterization of Pristine SWNT/Si Solar Cells

The fabrication process of the Si substrate has been introduced in Chapter 3.2.2. After preparation of the Si substrate, the SWNT film was transferred onto the top surface of the Si substrate after the removal of the 3 mm × 3 mm physical masks through a hot water thermocapillary method (Figure 4- 21). The photos of the fabricated solar cells are shown in Figure 4- 22. Four kinds of SWNT films, *i.e.*, the micro-honeycomb network ( $\mu$ -HN, Figure Figure 4- 23b), the collapsed honeycomb network (collapsed HN, Figure 4- 23c), the porous honeycomb network (porous HN, Figure 4- 23d) are employed for fabricating SWNT-Si solar cells. The SWNT-Si diode was formed after the transfer.

The self-assembled SWNT films can be transferred onto arbitrary substrates by the hot-water thermocapillary method [65]. The SWNT-Si junction was formed after transferring the self-assembled SWNT film onto an n-type Si wafer (doping level  $\sim 10^{15} \text{ cm}^{-3}$ ) which has a 3 mm × 3 mm bare Si contact window in the center (Figure 4- 23 a). The current density–voltage ( $J$ - $V$ ) characteristics of the SWNT-Si solar cells fabricated with  $\mu$ -HN, collapsed HN and porous HN were obtained under 100 mA/cm<sup>2</sup> AM 1.5G illumination (Newport Co.) and dark conditions, as shown in Figure 4- 23e. The  $J_{sc}$ ,  $V_{oc}$  and FF are listed in Table 4-1. The pristine  $\mu$ -HN SWNT-Si solar cell exhibited the highest, stable FF of 72%, with an ideality factor of 1.71 over the 300 to 500 mV range (obtained from the slope of the quasi-linear part of the logarithmic scale J-V curve under dark condition). To our knowledge, this ideality factor is the lowest reported thus far (*i.e.*, closest to an ideal device). The PCE value of 5.91% was obtained immediately after the fabrication, and it gradually increased to 6.04% after three weeks in ambient conditions (Figure 4- 23e).

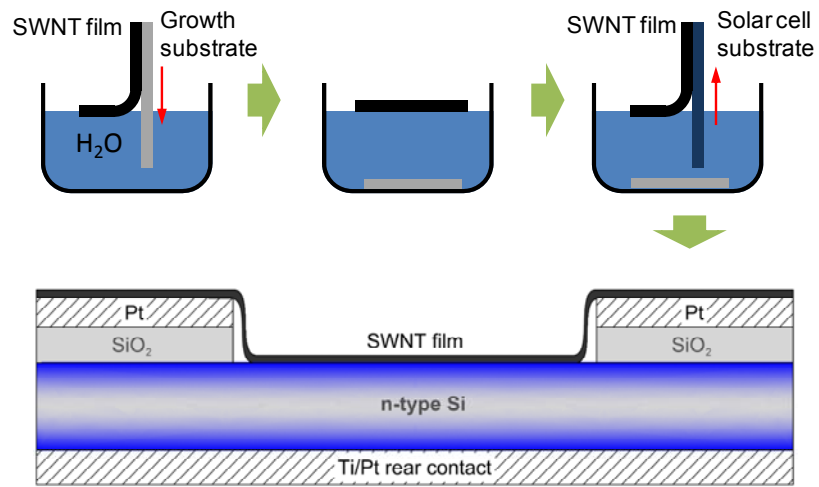


Figure 4- 21 Transfer process of the self-assembled SWNT films onto the Si substrate for the fabrication of SWNT-Si solar cells and schematic of the fabricated solar cell.

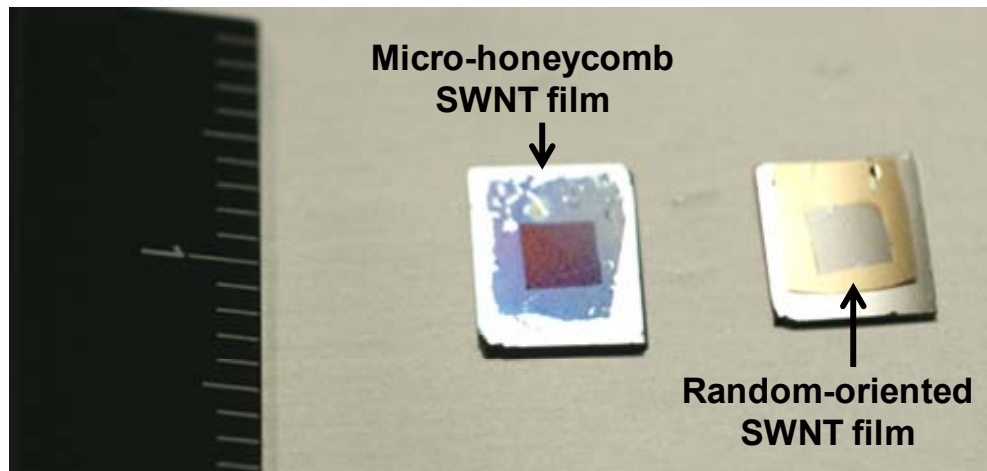


Figure 4- 22 Photos of fabricated SWNT-Si solar cells. The left one has microhoneycomb networked SWNT film on top and the right one has random-oriented SWNT film on top.

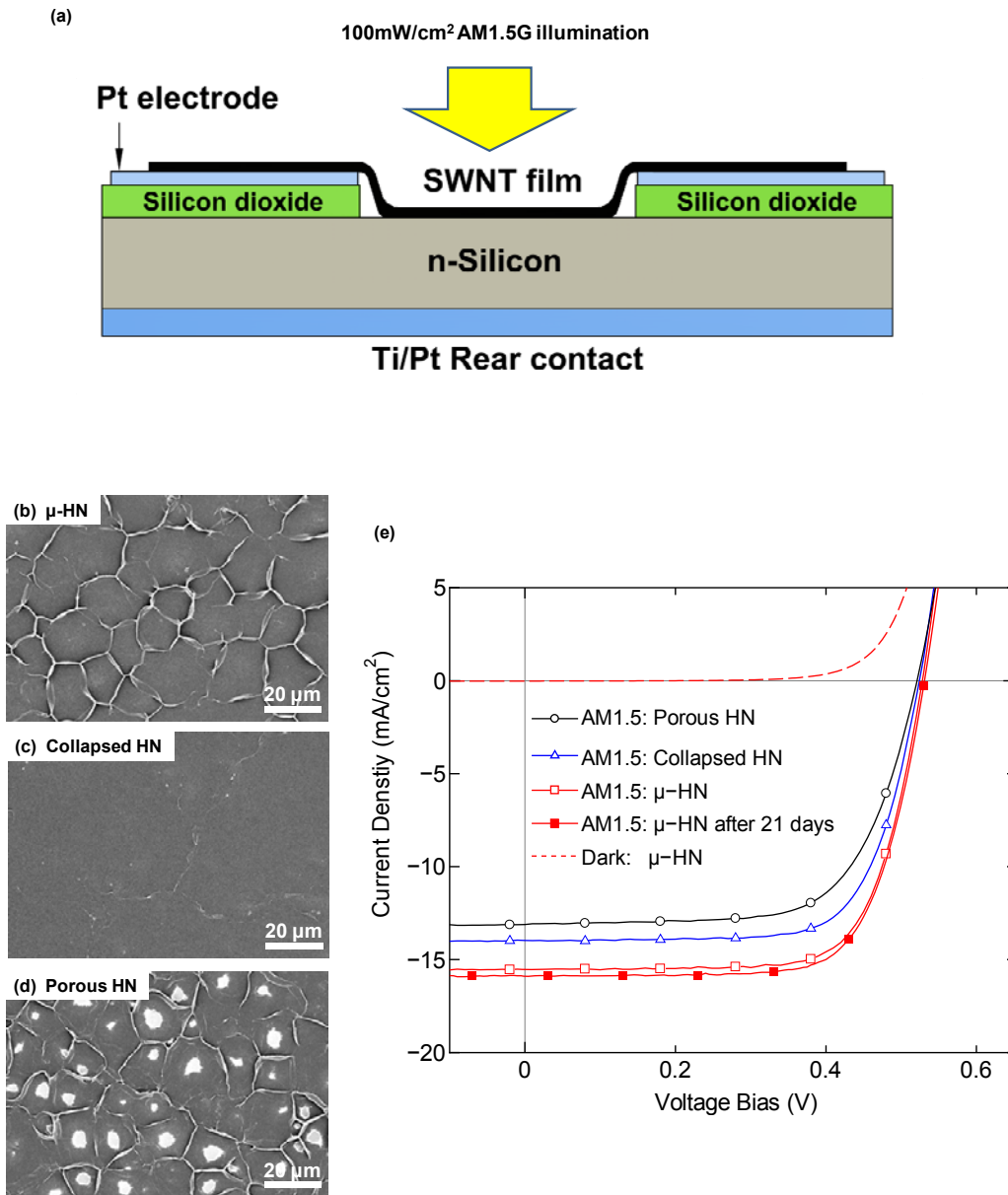
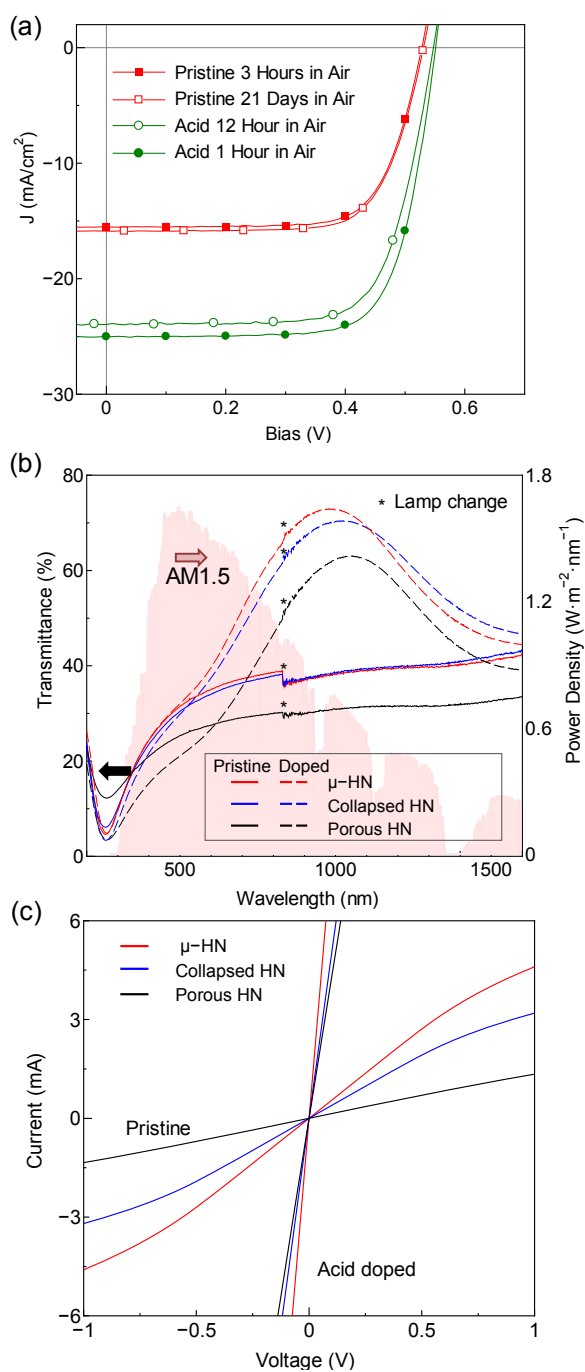


Figure 4- 23 (a) Schematic of SWNT-Si solar cell. (b-d) Three selected assemblies for the fabrication of solar cells and the photovoltaic performance of the fabricated solar cells. (b)  $\mu$ -HN. (c) Collapsed HN. (d) Porous HN. (e)  $J-V$  characteristics of SWNT-Si solar cells with  $\mu$ -HN, collapsed HN and porous HN measured under AM1.5G 100mW/cm<sup>2</sup>. The dashed line and solid line denote the  $J-V$  curve of the solar cells within three hours (immediate) and after three weeks after fabrication, respectively.



**Figure 4- 24 (a)  $J$ - $V$  characteristics of a micro-honeycomb structured SWNT-Si solar cell measured three hours and 21 days after device fabrication (shown in red), as well as 1 h and 12 h after dilute nitric acid doping (shown in green). (b) UV-vis-NIR transmittance spectra of  $\mu$ -HN, collapsed HN and porous HN for pristine (solid) and doped (dashed) conditions (left y axis) with AM1.5G spectrum (right y axis). (c) Sheet resistance of  $\mu$ -HN, collapsed HN and porous HN structures before and after acid doping.**

**Table 4- 1 Optical transmittance (over the AM1.5G spectrum) and average sheet resistance of  $\mu$ -HN, collapsed HN and porous HN, and the photovoltaic performance of the fabricated solar cells – FF, short-circuit current ( $J_{sc}$ ) and open-circuit voltage ( $V_{oc}$ ) – for SWNT-Si solar cells under AM1.5G and 100 mW/cm<sup>2</sup> illumination.**

*Within three hours of fabrication*

self-assembled morphology	solar cell performance				film properties	
	PCE (%)	FF (%)	$J_{sc}$ (mA/cm <sup>2</sup> )	$V_{oc}$ (mV)	$R_{sh}$ ( $\Omega$ /sq.)	$T_{AM1.5G}$ (%)
$\mu$ -HN	5.91	72	15.54	530	614	35.0
Collapsed HN	5.22	71	13.97	525	863	34.6
Porous HN	4.56	67	13.11	520	2397	28.1

*After three weeks in air*

self-assembled morphology	solar cell performance				film properties	
	PCE (%)	FF (%)	$J_{sc}$ (mA/cm <sup>2</sup> )	$V_{oc}$ (mV)	$R_{sh}$ ( $\Omega$ /sq.)	$T_{AM1.5G}$ (%)
$\mu$ -HN	6.04	72	15.90	530	-	-
Collapsed HN	5.32	70	14.41	525	-	-
Porous HN	4.71	68	13.27	520	-	-

*After nitric acid treatment*

self-assembled morphology	solar cell performance				film properties	
	PCE (%)	FF (%)	$J_{sc}$ (mA/cm <sup>2</sup> )	$V_{oc}$ (mV)	$R_{sh}$ ( $\Omega$ /sq.)	$T_{AM1.5G}$ (%)
-HN	10.02	73	25.01	550	105	48.5
Collapsed HN	8.35	73	20.68	550	120	46.3
Porous HN	8.30	69	21.86	550	139	37.0

The FF represents the quality of a solar cell, and is one of three parameters characterizing solar cell performance along with  $V_{oc}$  and  $J_{sc}$ . The significant improvement in FF and ideality factor over previously reported values [30] is attributed to the hierarchical  $\mu$ -HN, which simultaneously enhances carrier separation, collection and transport. The dense, cross-linked SWNT walls in the  $\mu$ -HN act as efficient conduction pathways, essentially serving as a micro-grid electrode to collect the charge carriers generated from the adjacent micro-honeycomb cells. The micro-grid configuration in the  $\mu$ -HN significantly shortens the minimum carrier diffusion path, resulting in more efficient photocurrent collection. In the solar cells

fabricated using collapsed HN and porous HN, the micro-grid configuration still exists, which leads to the quite high FFs.

The photocurrent generation mechanism of the carbon nanotube/n-Si solar cells is still not yet clear. Originally, it was regarded as *p-n* heterojunction solar cells, so SWNTs with larger band gap, such as (6,5) and (7,5) enriched SWNTs were used with the aim of increasing the built-in potential. However, as graphene could also work instead of carbon nanotubes, and the current result with larger-diameter SWNTs (average diameter of 2 nm) shows a better performance than (6,5) and (7,5) enriched samples. It can be inferred that SWNT film serve as a hole collector in carbon nanotube-Si solar cells.

The samples with three aforementioned morphologies were all divided into halves, with one half of each used for solar cell fabrication and the other half transferred onto quartz substrates in order to characterize the electrical and optical properties of the self-assembled SWNT structures. The sheet resistance was measured by the four-point probe method (analyzer: Agilent 4156C; probe bed: Kyowa Riken K89PS), while optical transmittance spectra were obtained by UV-vis-NIR spectroscopy (SHIMADZU UV-3150). As shown in Table 1, the sheet resistance of the  $\mu$ -HN was 28.9% and 74.4% lower than those of the collapsed HN and the porous HN, respectively. The  $\mu$ -HN also exhibited the highest transmittance over the AM1.5G spectrum ( $T_{AM1.5G} = 35.0\%$ ). The substantial decrease in the sheet resistance and the increase in the transmittance are realized only by the morphology manipulation of SWNTs. Moreover, as part of the SWNT array aggregates into the wall structures, fewer SWNTs end up collapsed on the bottom of the cell, thereby blocking less light from reaching the Si surface. Hence, the  $\mu$ -HN simultaneously shows higher transmittance and better conductivity than collapsed HN and porous HN structures.

#### 4.4.2 Performance Characterization of Acid-Doped SWNT/Si Solar Cells

A doping process was then carried out by dropping 120  $\mu\text{L}$  of 2.4 M nitric acid onto the device which was heated to 50  $^{\circ}\text{C}$  using a hot plate. The  $\mu\text{-HN}$  structure remains almost unchanged after the acid doping process (**Figures 4-25 (a) and (b)**). After drying, the PCE reached 10.02%, with an even higher FF of 73%. The  $J\text{-}V$  characteristics of the SWNT-Si solar cells after doping are shown in Figure 4-14a. The open-circuit voltage and short-circuit current after doping increased to 0.55V and 25.01  $\text{mA}/\text{cm}^2$ , respectively. The PCE value of the  $\mu\text{-HN}$  SWNT-Si solar cell decreased to 9.29% after 12 hours, which may be attributed to accelerated oxidation at the Si surface. The reduction of PCE after acid treatment has also been reported previously. A substantial increase in the transmittance spectrum from 600 nm to 1200 nm (**Figure 4- 24 (b)**) and a five-fold decrease in the sheet resistance (from 614  $\Omega/\text{sq.}$  to 105  $\Omega/\text{sq.}$ , as shown in **Figure 4- 24 (c)**) contribute to the increase of the PCE. The doping of the film also helps increase the charge collection efficiency. The dramatic changes in the electrical and the optical properties result from charge transfer from the SWNTs induced by the nitric acid. Depletion of electrons from the valence band results in a shift in the Fermi level and the attenuation of absorption peaks. The decrease of sheet resistance may be also attributed to further bundling of SWNTs.

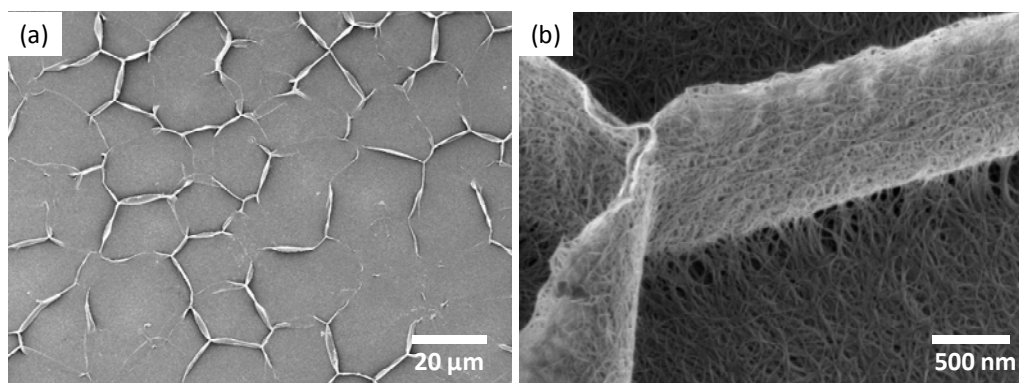


**Figure 4- 25** SEM images the  $\mu\text{-HN}$  after acid doping. (a) Long-range morphology. (b) Magnified image of the wall in the  $\mu\text{-HN}$ .



#### 4.4.3 Wavelength dependence of photocurrent generation

The spectrum responses (SM-250TF, Bunkoukeiki Co. Ltd) of both SWNT-Si solar cell and Si p-n junction solar cell (Si photodiode S1337, Hamamatsu Photonics K.K.) were obtained to discuss the wavelength dependence of the photocurrent generation. As shown in **Figure 4- 26**, there is almost no external quantum efficiency when the photon energy is smaller than the silicon band gap (~1100 nm) for the SWNT-Si solar cell. Moreover, the SWNT-Si solar cell showed a similar shape as the conventional Si *p-n* junction solar cell. No obvious correlation between the SWNT absorption and the SWNT-Si spectrum response was observed in the 300 nm ~ 1150 nm range. This may be attributed to that the diameter of the SWNTs used in this research is around 2 nm, so that the main absorption peak  $E_{11}$  is around 2400 nm wavelength in the infrared region. This result further supports that the SWNT-Si solar cell is inversion type solar cell.

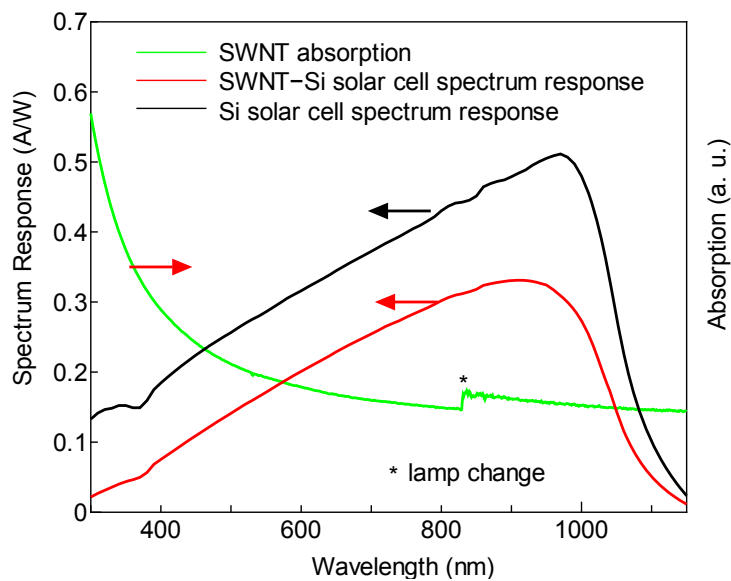


**Figure 4- 26** External quantum efficiency of the SWNT-Si solar cell and Si solar cell (left y axis), as well as the absorption spectrum of the SWNT therein (right y axis)

## 4.5 Mechanism of Performance Improvement by Micro-Honeycomb Network

The fill factor (FF) determines the quality of a solar cell, which is one of the three criteria characterizing the solar cell performance along with short-circuit current ( $J_{sc}$ ) and open-circuit voltage ( $V_{oc}$ ). In this study, the FFs of the SWNT-Si solar cells using the pristine  $\mu$ -HN, the collapsed HN, the porous HN and the TCF90 films were 72%, 70%, 68% and 61%, respectively. The pristine  $\mu$ -HN SWNT-Si solar cell exhibited the highest and stable FF with an ideality factor of 1.71 over the 300 to 500 mV bias range. To our knowledge, this ideality factor is the lowest reported so far. The highest FF of the pristine  $\mu$ -HN SWNT-Si solar cell demonstrated that the SWNT films with the three-dimensional  $\mu$ -HN could organize the charge separation, collection and transport in a more efficient way [41].

The modeling and curve fitting to the experimental  $J$ - $V$  curve is an insightful method for the in-depth investigation of the solar cell performance. Here, the diode equation was utilized to model the operation of SWNT/Si solar cells,

$$I = I_{sc} - I_0 \exp\left[\frac{q(V + IR_s)}{nkT}\right] - \frac{V + IR_s}{R_{sh}} \quad (1)$$

where  $n$  is the ideality factor,  $I_0$  is the dark saturation current,  $kT/q$  is the thermal voltage,  $I_{sc}$  is the short-circuit current,  $R_s$  and  $R_{sh}$  are series and shunt resistance of the equivalent circuit, respectively. As shown in **Figure 4- 28**, the experimental  $J$ - $V$  curves were well-fitted by the diode equation model. Through the curving fitting of the  $J$ - $V$  characteristics, the values of  $R_s$  and  $R_{sh}$  can be extracted. For all the solar cell samples, the extracted  $R_{sh}$  are over 20 k $\Omega$ , which makes them applicable for the operation under 100 mW/cm<sup>2</sup>. The extracted  $R_s$  for the  $\mu$ -HN, collapsed HN and porous HN, as well as the nitric-acid doped  $\mu$ -HN are calculated as 15  $\Omega$ , 16  $\Omega$ , 18  $\Omega$  and 11  $\Omega$ , respectively, while the extracted  $R_s$  for the TCF90 sample is 33.8  $\Omega$ .

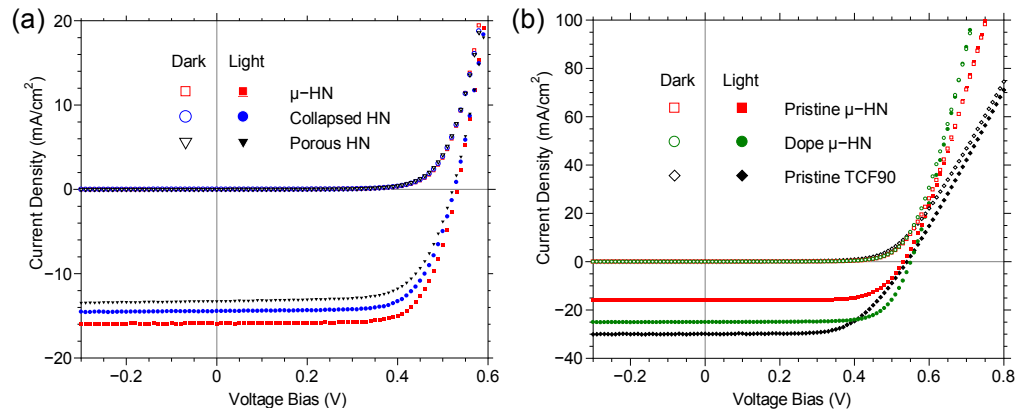


**Figure 4- 27 (a)  $J$ - $V$  characteristics of the SWNT-Si solar cells with the  $\mu$ -HN, collapsed HN and porous HN SWNT films measured under dark and light conditions. (b)  $J$ - $V$  characteristics of the SWNT-Si solar cells with the pristine  $\mu$ -HN, doped  $\mu$ -HN and pristine TCF90 films measured under dark and light conditions.**

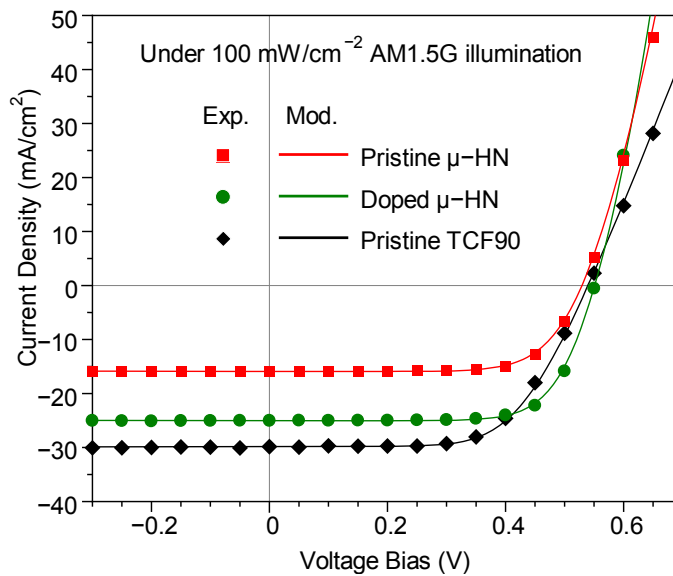


**Figure 4- 28 Experimental and modeling results of the  $J$ - $V$  characteristics of the SWNT-Si solar cells with the pristine  $\mu$ -HN, the doped  $\mu$ -HN and the pristine TCF90 films.**

The  $R_s$  and  $R_{sh}$  could be used to evaluate the quality of a solar cell and are closely related with FF. In this research, the effect of  $R_{sh}$  could be ignored, owing to the very high  $R_{sh}$  resulted from the  $\text{SiO}_2$  insulating layer with the thickness of 200 nm. Therefore, the discussion is focused on the relationship between  $R_s$  and FF. Besides of the five solar cell samples discussed in **Figure 4- 27**, another six SWNT-Si solar cells with ill-formed honeycomb networked SWNT films and randomly oriented SWNT

films with 70% (TCF70) and 80% (TCF80) transparency were also compared. The relationship between the  $R_s$  and FF of the eleven solar cell samples is given in **Figure 4- 29**. The FF values for the SWNT-Si solar cells using  $\mu$ -HN, collapsed HN and porous HN, as well as the nitric-acid doped HN were 72%, 70%, 68% and 73%, respectively. The FF value for the SWNT/Si solar cell using the TCF90 film is 61%. As shown in **Figure 4- 29**, the  $R_s$  and FF is linearly related. The FF increases with the decrease of  $R_s$ . The significant improvement in terms of the FF of the hierarchical  $\mu$ -HN compared with that of the TCF90 is attributed to simultaneously enhanced carrier separation, collection and transport. The dense, cross-linked SWNT walls in the  $\mu$ -HN act as efficient conduction pathways, essentially serving as a micro-grid electrode to collect the charge carriers generated from the adjacent micro-honeycomb cells. The micro-grid configuration in the  $\mu$ -HN significantly shortens the minimum carrier diffusion path, resulting in more efficient photocurrent collection. In the solar cells fabricated using the collapsed HN and porous HN, the micro-grid configuration still exists, which leads to their quite high FFs.

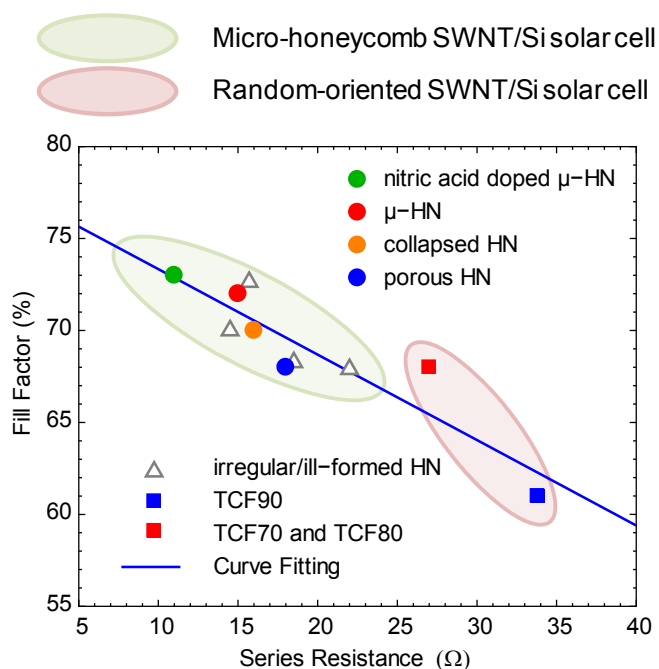


**Figure 4- 29** The relationship between the  $R_s$  and FF of the eleven solar cell samples: pristine and doped  $\mu$ -HN, collapsed HN, porous HN, four ill-formed honeycomb networked SWNT films and randomly oriented SWNT films with 70% (TCF70), 80% (TCF80) and 90% (TCF90) transparency.

## 4.6 Summary

In this study, a simple water vapor treatment to engineer the structure of VA-SWNTs into a micro-honeycomb network was proposed and used for the SWNT-Si solar cells. The hierarchical  $\mu$ -HN consists of dense walls and a buckypaper bottom, which simultaneously increases the optical transmittance and decreases the sheet resistance. Applying  $\mu$ -HN to the SWNT-Si solar cell results in both high PCE and high FF. Moreover, the state-of-the-art randomly oriented SWNT film was also used for SWNT-Si solar cells, demonstrating a high PCE. The hierarchical  $\mu$ -HN is very promising for the applications of SWNT-Si solar cells. The full exploitation of the superior electrical, optical and chemical properties of SWNTs is very promising for the next generation photovoltaic devices.



## **Chapter 5**

# **CVD Controlled Growth of SWNT films for Solar Cell Applications**

The rich variety of SWNT chirality provides the possibility for many promising applications or even multi-purpose applications. The atomic scale difference in the SWNT structure leads to the band gap spectrum ranging from 0.5 to 2 eV. However, this variety is also a problem for SWNTs: it is very difficult to obtain high-quality SWNT assemblies with single chirality. The most critical obstacle hindering the widespread application of SWNTs is the production of monochiral SWNTs. Since the discovery of SWNTs more than 20 years by Dr. Iijima [5], many researchers over the world have been investigating the production of monochiral SWNTs. Although certain

advancement and understanding have been obtained, it is still not possible to synthesize SWNT assemblies with controlled chiralities. Many researchers started to look at the post-processing technique, *e.g.* separation of SWNTs [79], removal of certain SWNTs [80]. The separation technique for SWNTs has been developed to a relatively mature level in terms of both the high-purity chirality [81, 82] and large-scale production [83]. However, the monochiral SWNTs obtained by the separation technique have more defects and shorter length, which resulted in low performance for device applications. The direct synthesis of SWNTs is of high necessity.

This chapter will start with the brief history and literature review of the synthesis of SWNTs, discussing the strategies and roadmap of further development in the perspective of the Author, as well as the state of the art of CVD growth of SWNTs. The growth of sub-nanometer scale vertical-aligned SWNT arrays which is achieved for the first time will be then discussed. The thermodynamic effect on the growth of SWNTs would be characterized by Raman spectroscopy, scanning electron microscopy (SEM) and absorption spectroscopy.

## **5.1 State of the Art of CVD Growth Control of SWNTs**

In the early years of SWNT research, the arc discharge method, laser oven methods, etc. have been developed for the synthesis of SWNTs. But it is not until Hongjie Dai in 1996 who was then working at Smalley Group at Rice University and colleagues developed a method to synthesize SWNTs by chemical vapor deposition (CVD) that the growth control of SWNTs became possible [84]. Essentially, the CVD process is the adsorption of the gas-phase carbon precursor on the metallic catalyst followed by the precipitation of carbon as carbon nanotubes. Scientists would expect to control the diameter or even the chirality of the SWNTs through tuning the



properties of the metallic catalysts, *e.g.* nanoparticle size and facet, catalytic properties, carbon solubility in metal particles as well as inter-metallic solutions, *etc.* The CVD is also believed as a controllable process as the temperature, pressure and the supply of carbon precursor. It seemed that all needs to be done is the parametric analysis of the above-mentioned factors and the diameter/chirality controlled growth seemed to be only a matter of time. However, after an intensive worldwide research, up to date, the chirality control of SWNTs is still not yet achieved. The CVD process is actually much more complicated than scientists expected. But certain knowledge and insight have been obtained which serve as the base for further studies. In this section, an extensive literature review will be given at first, followed by the progress achieved so far in this laboratory, both of which provide great inspiration for the Author.

Generally, there are three directions of the SWNT synthesis: growth on support particles (P-CVD), growth on substrate (S-CVD) and growth on floating catalysts (FC-CVD), as shown in **Table 5- 1**. For the P-CVD, the metallic catalysts are loaded on mesoporous particles, *e.g.* zeolite [7, 85], MgO [86-88], mesoporous silica [89-93], *etc.* The supporting mesoporous particles confine the metallic catalysts in all three dimensions, by which the catalysts are prevented from being aggregated together, *i.e.* the so-called Oswald ripening. The very small size of the catalysts would produce SWNTs with small diameters with relatively narrow diameter distribution (this is not always true although). The GSP has been developed to a quite mature stage. The most famous commercialized product/method is CoMoCAT [94] which has more than 90% (6,5) and (7,5) tubes. The CoMoCAT process use Co-Mo binary metallic catalysts supported by silica and CO as carbon precursor. The absorption spectrum of dispersed commercially available CoMoCAT sample is shown in **Figure 5- 1**. The major absorption peak is from the  $E_{11}$  of (6,5) SWNT. Prior to the successful CoMoCAT, our laboratory has done a groundbreaking work on the CVD growth, the so-called

ACCVD process, which is also commercialized. The ACCVD process and its derivatives will be introduced in the next section. Both the CoMoCAT and ACCVD papers have been cited by more than 500 times so far. Despite the excellent controllability, the as-synthesized SWNTs by P-CVD cannot be easily used for devices directly. To obtain certain morphology of SWNTs and remove the supporting particles, it is necessary to use the dispersion and separation techniques which induce defects to SWNTs and significantly shorten the tube length. This is one reason that the devices using CoMoCAT SWNTs have relatively low performance. To sum up, the P-CVD is an excellent strategy for the discussion of growth mechanism and spectroscopy investigations, but not necessarily suitable for the device applications.

**Table 5- 1 Strategic directions of the growth control of SWNTs**

<b>Strategic Directions</b>		
<b>Growth with Support</b>	<b>Growth on Substrate</b>	<b>Floating Catalyst</b>
Three-Dimensional Confinement on Catalysts	One-Dimensional Confinement on Catalysts	No Confinement on Catalysts
Small Diameter	Relative Large Diameter	Large Diameter
Particles	Vertically Aligned Horizontally Aligned Random Oriented	Random Oriented
Diameter > 0.7 nm	Diameter > 1 nm	Diameter > 1.3 nm
Good For Mechanism Bad For Application	Not Easy For Mechanism Good For Application	Not Easy For Mechanism Good For Application

On the contrary, in the FC-CVD process, the metallic catalysts are able to move in all three dimensions. With the increase of the possibility of catalysts collision, the resulting diameter of the SWNTs are usually larger than that of that by the P-CVD process. The as-synthesized SWNTs in the CVD reactor are usually collected by a

low-adhesion filter paper [15, 16, 95]. The morphology of the SWNTs is always randomly oriented, although it is possible to collect the nanotubes with a pattern to obtain certain three-dimensional structure. The collected random-oriented SWNTs films can be easily transferred to other substrate by using the difference of the adhesion force between the SWNT films and substrate.

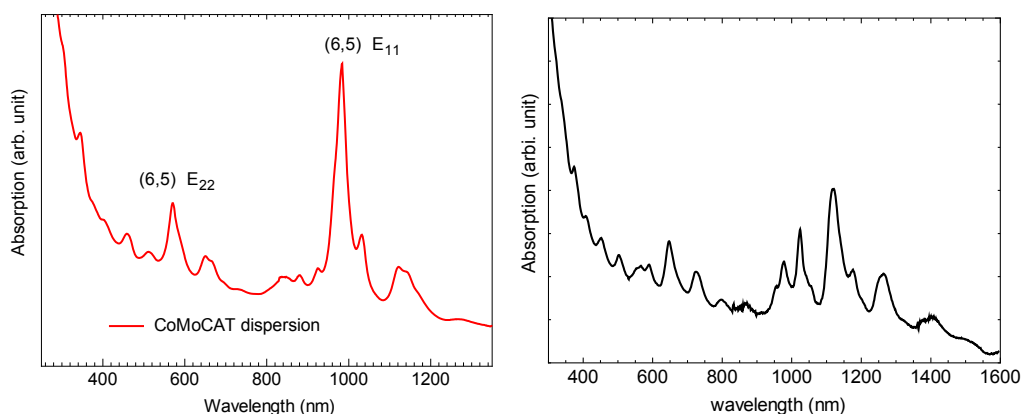


**Figure 5- 1 Absorption spectrum of dispersed commercial CoMoCAT SWNT (left) and commercial ACCVD SWNT samples.**

For the S-CVD direction, the SWNTs are grown directly on a substrate without supporting particles. Therefore, the metallic catalysts are able to move in two dimensions. At high temperature which is needed for the SWNT growth, the metallic catalysts would grow to larger size due to the Oswald ripening effect. The resulting diameter of the SWNTs by S-CVD are not necessarily smaller than that of the SWNTs produced in the FC-CVD process considering the large space of the CVD reactor in the FC-CVD. The diameters of the SWNTs synthesized in this direction are usually from 1.3 nm to larger than 3 nm, with wide diameter distribution. Although the nanoscale properties of SWNTs including the diameter and chirality are not well controlled in the S-CVD direction, the microscale morphology can be tuned at a relatively mature level, which guarantees the as-synthesized SWNTs by GSub can be used directly for device applications. So far, the horizontally aligned SWNTs with tunable tube density [96-99], the vertically aligned SWNTs [61, 64, 66, 100, 101] with

tunable thickness and randomly oriented SWNTs [62] have been achieved. It is possible to fabricate a device directly from the as-synthesized SWNTs and substrate. There are also various methods to transfer the as-synthesized SWNTs to other substrate. The controllability of the SWNT morphology makes the S-CVD the most promising among the three strategies, with the greatest challenge for the S-CVD as chirality control of the SWNTs.

## **5.2 Literature Review**

### **5.2.1 Alcohol Catalytic Chemical Vapor Deposition**

In 2002, ethanol was used for the first time as carbon precursor for the synthesis of high-purity small-diameter SWNTs by Prof. Shigeo Maruyama [7]. The process was named as alcohol catalytic chemical vapor deposition, the so-called ACCVD. Compared with the then commercialized SWNTs, HiPCO, ACCVD SWNTs has much smaller diameter and narrower distribution. Moreover, ethanol is much safer and greener than carbon monoxide. The ethanol soon became the most popular carbon precursor for SWNT growth. The paper published by Prof. Maruyama has been cited for more than 500 times. The ACCVD SWNTs are also commercialized with the collaboration of Toray Industries K.K. In a typical ACCVD process, the metal catalysts are prepared by dissolving iron acetate (2.5 wt%) and cobalt acetate (2.5 wt%) in ethanol mixed with Y-type zeolite powder (HSZ-390HUA). After drying, the zeolite loaded with metal catalysts are annealed to a typical 600 ~ 800 °C in 200 sccm Ar flow environment. Then the ethanol is flowed at 5 Torr after the evacuation of Ar.

The ACCVD was then investigated towards the direct growth on substrate. Owing to the high electrical and thermal conductivities, using SWNTs as thermal

interface materials is of great interest then. A possible design is the vertically aligned SWNTs mat, which is able to connect two interfaces by millions of SWNTs. The VA-SWNT mats on quartz substrates using ethanol was successfully achieved by Y. Murakami who was then a graduate student at this group [61, 62]. This pioneering result was also published on Chemical Physical Letters, a then high impact journal, and has been cited for more than 300 times. In the typical ACCVD for VA-SWNT process, the metal catalysts are prepared by dip-coating cobalt and molybdenum from the corresponding ethanol solution on quartz or Si/SiO<sub>2</sub> substrates. After drying of the ethanol, the dip-coating process will leave a uniform layer of Co and Mo. The substrate loaded with the metal catalysts are then calcinated in the ambient at 400 degree Celsius for 5 min. The substrates are annealed in Ar/H<sub>2</sub> (3%) environment to a typical 800 degree Celsius in 30 min. After the annealing process, the ethanol is flowed at 450 sccm at 1 Torr to grow SWNTs. The thickness of the as-synthesized VA-SWNT mat usually ranges from several  $\mu\text{m}$  to 20  $\mu\text{m}$ . Figure 5- 2 shows the typical as-synthesized VA-SWNT mat through 2 min CVD growth, with the thickness of 12  $\mu\text{m}$ .

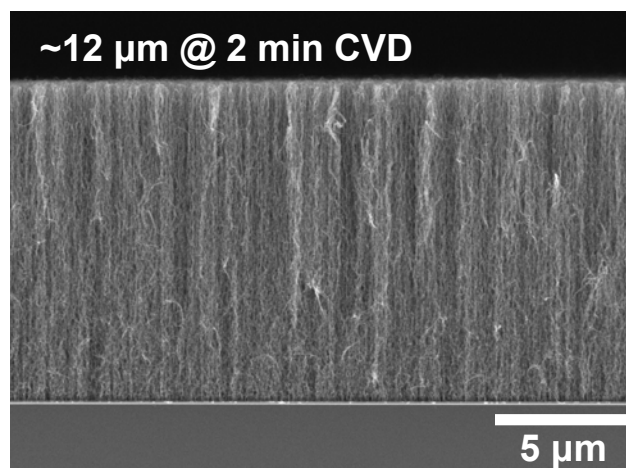


**Figure 5- 2 SEM image of the cross-sectional view of the as-synthesized VA-SWNT mat by ACCVD process. The 2 min CVD process yield 12  $\mu\text{m}$ -thick VA-SWNT mat.**

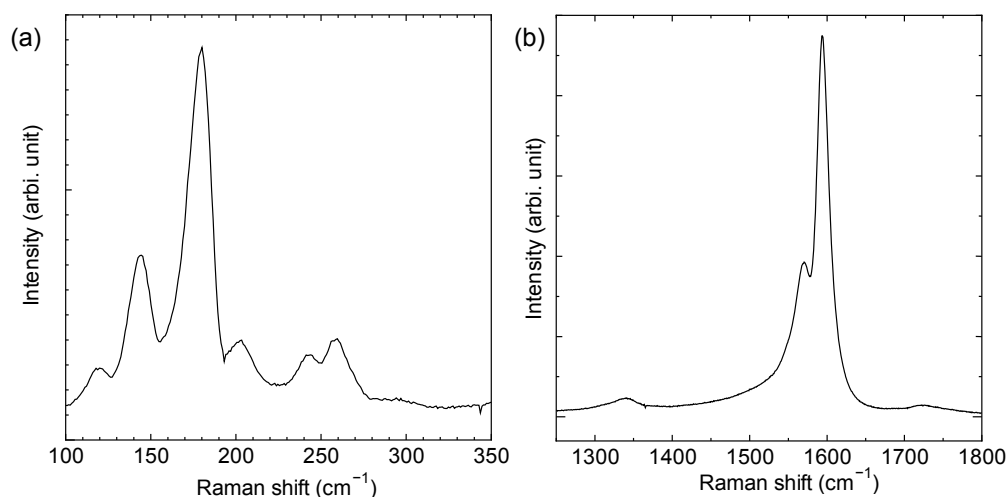


**Figure 5- 3 Raman spectroscopy of the as-synthesized VA-SWNT mat by ACCVD proces. (a) RBM and (b) G band and D band.**

The researchers who continued the work of ACCVD growth are Erik Einarsson, Rong Xiang and Theerapol Thurakitseree. Dr. Einarsson developed a method to monitor the growth process of SWNTs through a laser absorption method and investigate the number of SWNTs per bundle [64]. Dr. Xiang discussed the growth mechanism and successfully realized the diameter modulation of VA-SWNTs [66]. By changing the ratio of Co and Mo catalysts, the average diameter of the SWNTs can be tuned from 1.4 nm to 2.5 nm, which is still the smallest average diameter of pristine VA-SWNTs achieved so far. Instead of using ethanol as carbon stock, Dr. Thurakitseree used acetonitrile (CH<sub>3</sub>CN) and successfully grew the nitrogen-incorporated SWNTs with a very small average diameter of 0.7 nm [102]. It is very interesting that the nitrogen molecules are found inside the SWNTs.

There are several ideas that could be drawn from the above work: (1) the functionalized group in the carbon precursor actually play an important role in SWNT growth. The -OH radicals could etch the amorphous carbon and defects in SWNTs, which results in the high-quality of SWNTs with relative low yield compared with methane. The -N could limit the growth rate and hence a very small diameter. However, without -OH radicals, the quality of SWNT would be relatively low. (2)

The choice of catalysts could be very important. The combination of Co and Mo used in ACCVD VA-SWNTs is the same with that in CoMoCAT. Generally speaking, binary metallic alloy would provide more control on the status of the catalysts. (3) It is highly necessary to grow SWNTs on substrate with further diameter control, while at the same time retaining the well control of microscale morphology.

### 5.2.2 CVD Growth on Cu-based Catalysts

In this section, a thorough literature review of the CVD growth on Cu-based catalysts is given as a knowledge pool for the further investigations of this chapter. The discussion of the CVD growth on Cu is very important as the carbon-cu interaction and the carbon-Fe, -Co and -Ni interaction is different in terms of both the carbon solubility and catalytic activity.

The first paper realized efficient SWNT growth on Cu nanoparticle catalysts was reported by Yan Li group at Peking University in 2006 [103]. At that time, it was very popular to explore all possible catalysts for carbon nanotube growth. Other noble metals, *e.g.* Au, Pt [104], Ag *etc.*, or even non-metals [105-108] have been utilized for carbon nanotube growth. Most of these papers were published on Journal of the American Chemical Society, Nano Letters, *etc.*, which are high-impact journals in the field of chemistry and nanotechnology. And Ref. [103] was one of frontier results back then [77]. Cu stands out among all the possible catalysts and has been used for the growth of horizontally aligned SWNTs in the following years. Interesting results include the growth of the horizontally aligned semiconducting-enriched (95%) SWNTs by Cu monometallic catalysts [109] and dense horizontally aligned SWNTs arrays by Fe-Cu bimetallic catalysts [110], both of which were published in 2009.

Afterwards, the idea of Cu used as catalysts for carbon nanotube growth was adopted by Esko Kauppinen group at Aalto University in Finland. Instead of using Cu

on the substrate, He *et al* deposited Fe/Cu bimetallic catalysts on MgO support and used carbon monoxide as precursor. At 600 °C CVD temperature, ratio of (6,5) SWNTs as high as CoMoCAT has been obtained [88]. The mechanism was explained as Cu assisted reduction of Fe at low temperature (600 °C) which significantly limit the possible varieties of the SWNT caps [87]. Later on in 2013, the effect of different ratios of Fe and Cu on the chiralities of SWNTs was investigated [86]. The Co/Cu bimetallic catalysts were also used and the resulting SWNTs possessed larger diameter and wider diameter distribution compared with the Fe/Cu catalysts. Generally speaking, the Fe/Cu bimetallic catalysts are not as effective on SWNT chirality control as Co/Mo bimetallic catalysts in the roadmap of GSP-CVD. However, the growth on the Cu-based catalysts is very inspiring for future work.

## **5.3 Synthesis of Sub-Nanometer-Diameter SWNT Films directly on Surface**

### **5.3.1 Experimental Design**

Iron, cobalt and nickel are usually considered as the core catalysts for carbon nanotubes growth, owing to their relative high catalytic activity and carbon solubility. According to the molecular dynamics simulation, the diameter of the SWNTs is related with the particle size of the catalysts, although they are not always equal [111]. The growth of carbon nanotubes in the CVD process can be generally considered as the adsorption of gas-phase carbon precursor until saturation, followed by the precipitation of the carbon. The caps of SWNTs are formed first and further precipitation results in the carbon nanotubes. Usually, to form a cap with a small diameter, two strategies are used: lowering the growth temperature and confine the



catalysts from Oswald ripening or aggregation. This is why GSP-CVD (three-dimensional confinement as discussed before) at low temperature leads to (6,5)-enriched SWNTs. One the good case of the second strategy is using tungsten-cobalt bimetallic catalysts. Recently, Yan Li group at Peking University reported near quasi-monochiral SWNT growth by tungsten-cobalt bimetallic catalysts at Guadalupe Meeting in Texas, and already published on Nature [112]. The idea of using tungsten is to utilize much higher melting temperature and at normal SWNT growth temperature, the catalysts are more fixed.

To use the low temperature strategy, certain catalytic activity needs to be guaranteed at such low temperature. Therefore, metals with lower temperature are preferred. The Cu-based catalysts will be adopted in the ACCVD process developed in this laboratory. Only  $\text{Mo}(\text{Ac})_4$  will be replaced with  $\text{Cu}(\text{Ac})_2$  with the same concentration. The detailed process is described as follows:

- (1) Dip-coat Cu on the Si/SiO<sub>2</sub> substrate. Bake in air at 400 °C for 5 min.
- (2) Dip-coat Co on the Si/SiO<sub>2</sub> substrate. Bake in air at 400 °C for 5 min.
- (3) Anneal the Si/SiO<sub>2</sub> substrate loaded with Co/Cu catalysts in the Ar/H<sub>2</sub> (3%) environment for 30 min until 650 °C in a quartz tube.
- (4) Evacuate Ar/H<sub>2</sub> and flow ethanol at 50 sccm for 2 min.
- (5) Cool the furnace in ambient environment and protect the sample with Ar flow.

The schematic of the process has been shown in Figure 4-1.

### 5.3.2 Low-Temperature ACCVD Synthesis of SWNTs with sub-nm Diameter

The SWNTs are synthesized by ACCVD process under three different parameters: catalyst Co/Cu at 650 °C CVD temperature (CoCu@650), conventional catalyst Co/Mo at 650 °C CVD temperature (CoMo@650) as a comparison and conventional catalyst Co/Mo at 800 °C CVD temperature (CoMo@800) as a reference material. The morphology of the CoCu@650 and CoMo@650 is random-oriented SWNT film, while the morphology of CoMo@800 is vertical-aligned SWNT film.

The Raman spectra of the as-synthesized SWNTs under the laser excitation energy of 2.54 eV, 2.33 eV, 1.96 eV and 1.58 eV are shown in **Figure 5- 4**, **Figure 5- 5**, **Figure 5- 6** and **Figure 5- 7**, respectively. It is very clear from the RBM that the CoCu@650 demonstrated a much smaller diameter and narrow diameter distribution for all the excitation energies. The diameter could be roughly estimated [8] as by

$$\omega = \frac{A}{d_t} + B \quad (5-1)$$

where  $\omega$  is the Raman shift and  $d_t$  is the diameter of the SWNTs. For SWNTs with diameter around 1.5 nm in bundles, A and B are constant and reported as  $A = 234 \text{ cm}^{-1}$  and  $B = 10 \text{ cm}^{-1}$  in Ref. [113]. The diameter of the conventional CoMo@800 conventional VA-SWNTs is around 2 nm. For the CoMo@650, the average diameter is smaller than that of CoMo@800, although with a wider diameter distribution. A obvious cleavage between the  $G^+$  and  $G^-$  is observed for the CoCu@650.

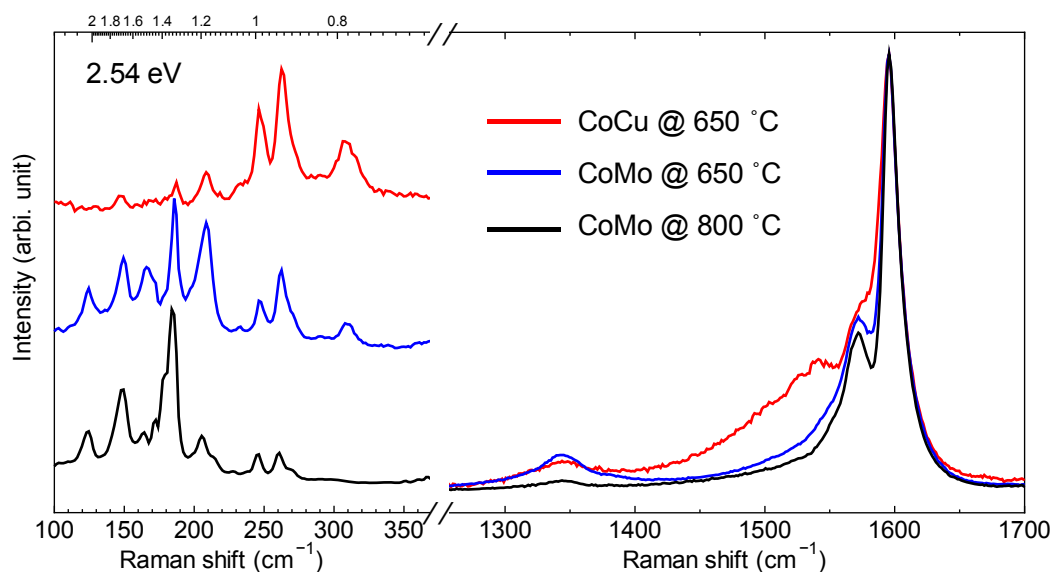


**Figure 5- 4 Comparison of Raman spectra of SWNTs synthesized from Co/Cu and Co/Mo at different temperatures. The laser excitation energy is 2.54 eV.**

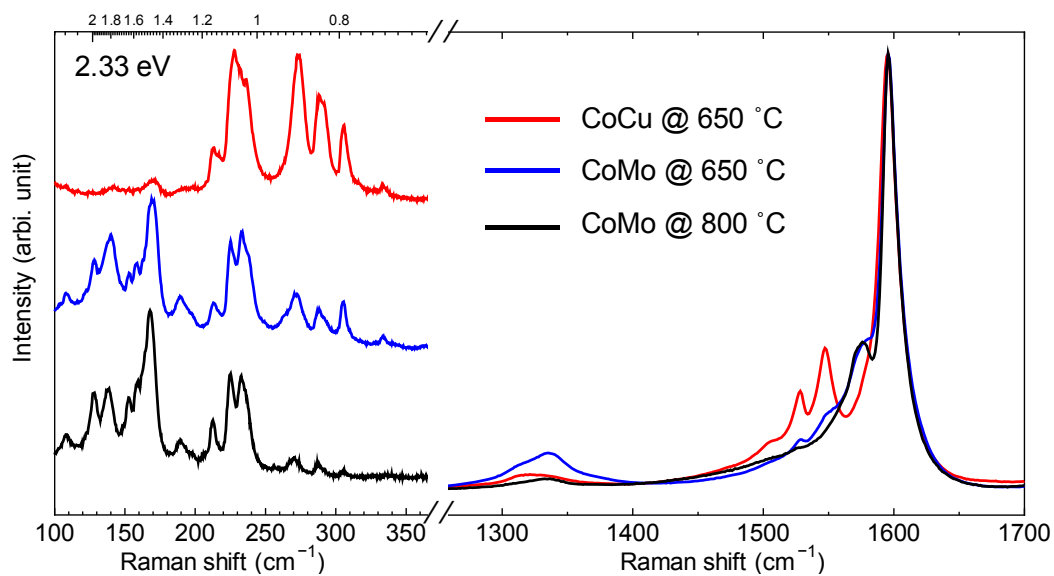


**Figure 5- 5 Comparison of Raman spectra of SWNTs synthesized from Co/Cu and Co/Mo at different temperatures. The laser excitation energy is 2.33 eV.**

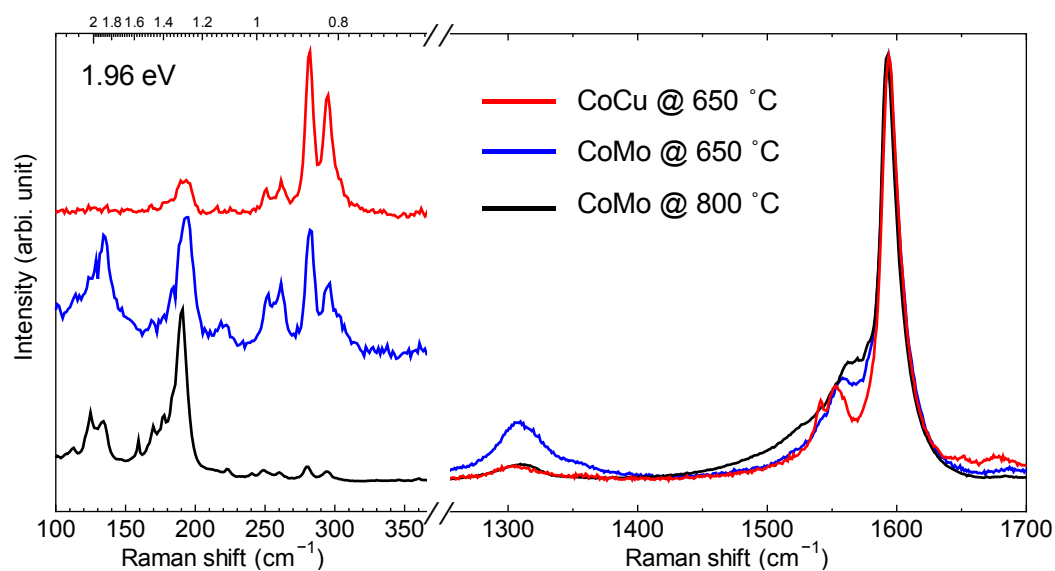


**Figure 5- 6 Comparison of Raman spectra of SWNTs synthesized from Co/Cu and Co/Mo at different temperatures. The laser excitation energy is 1.96 eV.**

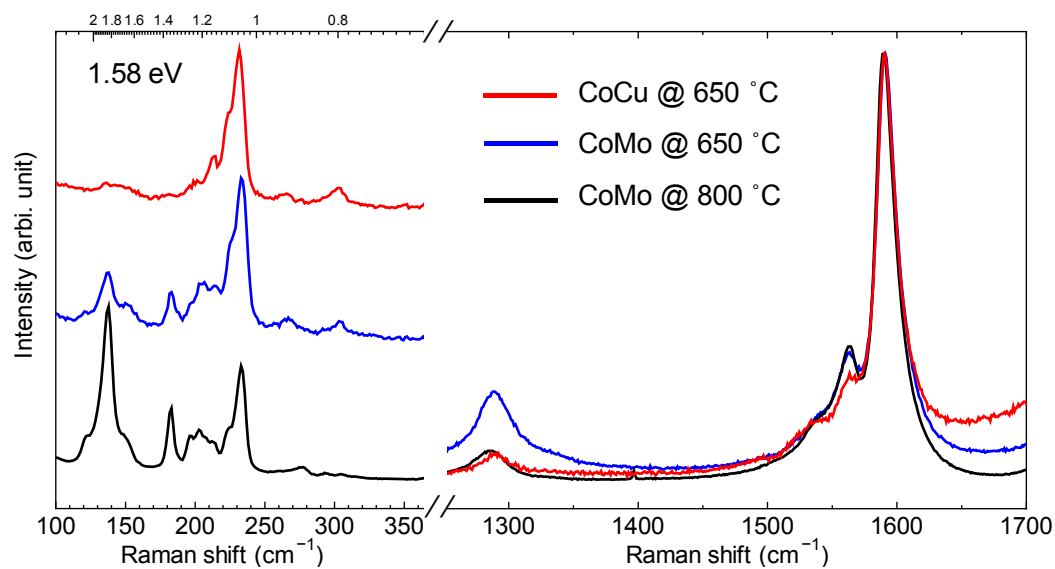


**Figure 5- 7 Comparison of Raman spectra of SWNTs synthesized from Co/Cu and Co/Mo at different temperatures. The laser excitation energy is 1.58 eV.**

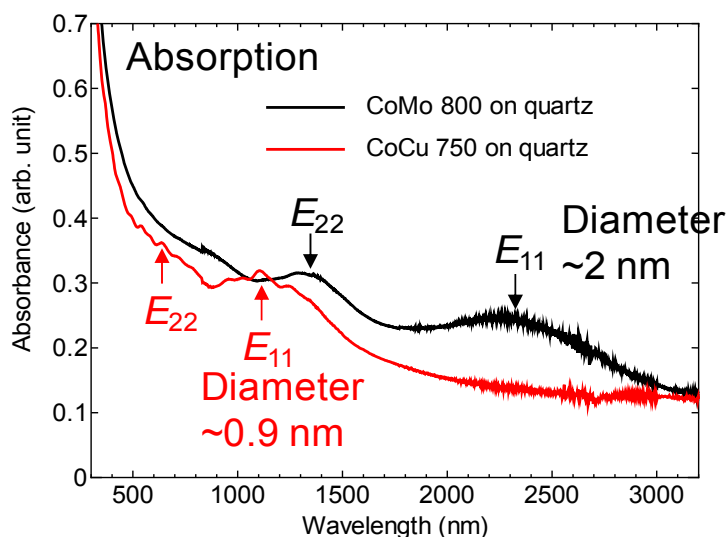


**Figure 5- 8** Comparison of absorption spectra of the conventional VA-SWNT synthesized by CoMo catalysts and 0.9-nm-diameter VA-SWNT synthesized by CoCu catalysts.

The absorption spectroscopy was carried out to examine the average diameter of the SWNTs synthesized by CoCu750 growth condition. The comparison of absorption spectra of the conventional CoMo800 condition and the CoCu750 condition is shown in **Figure 5- 8**. The  $E_{11}$  absorption peak was significantly shifted from 2400 nm to 1100 nm, which means the band gap of the SWNTs was increased from 0.5 eV to 1.1 eV. The diameter of the as-synthesized SWNTs could be confirmed by the TEM images shown in **Figure 5- 9**. The band gap of the SWNT synthesized by the CoCu750 condition is similar to that of Si. It becomes more and more possible to use the VA-SWNTs directly for the solar cell applications or some other devices.

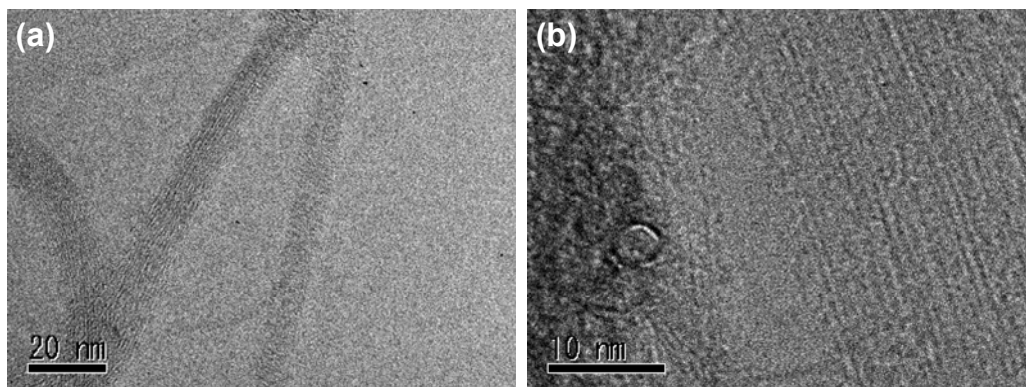


**Figure 5- 9** TEM images of SWNTs grown on Co/Cu catalysts.

## 5.4 Exploration of Thermodynamic Parameters for CVD

### Growth Control

#### 5.4.1 Effect of Temperature on Chiral Distribution of SWNTs

Although the initial idea to use Cu as a catalyst is to utilize their relatively high catalytic activity at low temperature such as 650 degree Celsius, after obtaining the SWNTs with very small diameters and narrow distribution at low temperature, we are very interesting to explore the growth with same catalyst combination at higher temperature. Therefore, with the same recipe, we tried the growth at 750 and 800 degree Celsius. Four experimental sets are designed as follows: (1) Co/Mo catalysts and 800 °C CVD temperature as a reference group (CoMo800); (2) Co/Cu catalysts and 800 °C CVD temperature (CoCu800); (3) Co/Cu catalysts and 750 °C CVD temperature (CoCu750); (4) to investigate the effect of the catalyst density, the Co was diluted to ten times, thus the concentration of the Co(Ac)<sub>2</sub> solution in ethanol is 0.01 wt%. The CVD temperature was kept at 800 °C. This group was named as Co0.1Cu750.

The Raman spectroscopy was conducted for the SWNTs grown on Co/Cu catalysts. As shown in **Figure 5- 10**, the diameter was further reduced to 0.85 nm for the CoCu650. The G- band became more prominent, indicating the enrichment of the small diameter SWNTs. Also for the 1.96 eV excitation laser as shown in **Figure 5- 11**, the G<sup>+</sup> and G<sup>-</sup> mode is separated at a very far distance. The D-band is almost negligible for SWNTs synthesized at all temperatures. To confirm the diameter distribution, we did the UV-vis-NIR absorption spectroscopy for the CoCu650, CoCu700 and CoCu750 samples. As shown in **Figure 5- 12**, the major chiralities of SWNTs grown by Co/Cu catalysts are (6,5) and (7,5) SWNTs, demonstrating the near-armchair chirality distribution. A further diameter reduction and narrower

chirality distribution is expected by changing the catalysts ratio.

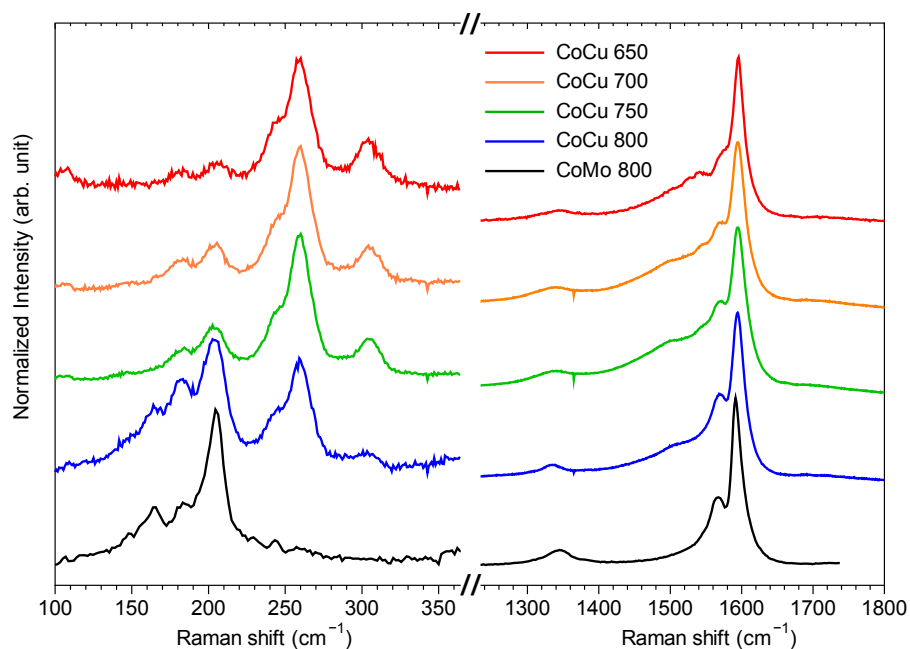


**Figure 5- 10 Raman spectra of the as-synthesized random-oriented SWNT films using Co/Cu catalysts under different CVD temperatures. The laser excitation energy is 2.54 eV.**

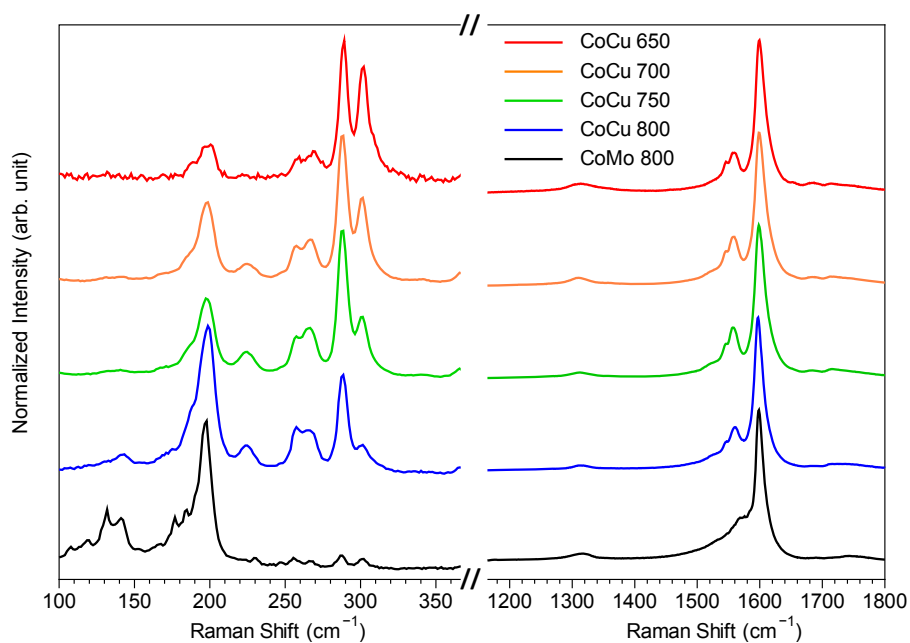


**Figure 5- 11 Raman spectra of the as-synthesized random-oriented SWNT films using Co/Cu catalysts under different CVD temperatures. The laser excitation energy is 1.96 eV.**

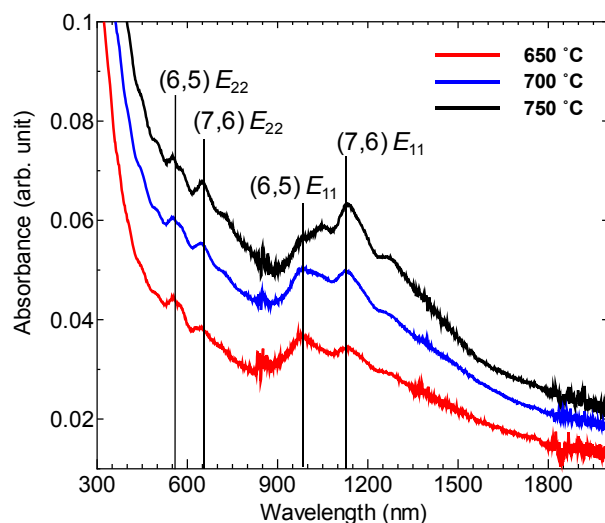


**Figure 5- 12** Absorption spectra of the as-synthesized random-oriented SWNT films using Co/Cu catalysts under different CVD temperatures.

### 5.4.2 Effect of Pressure on Chiral Distribution of SWNTs

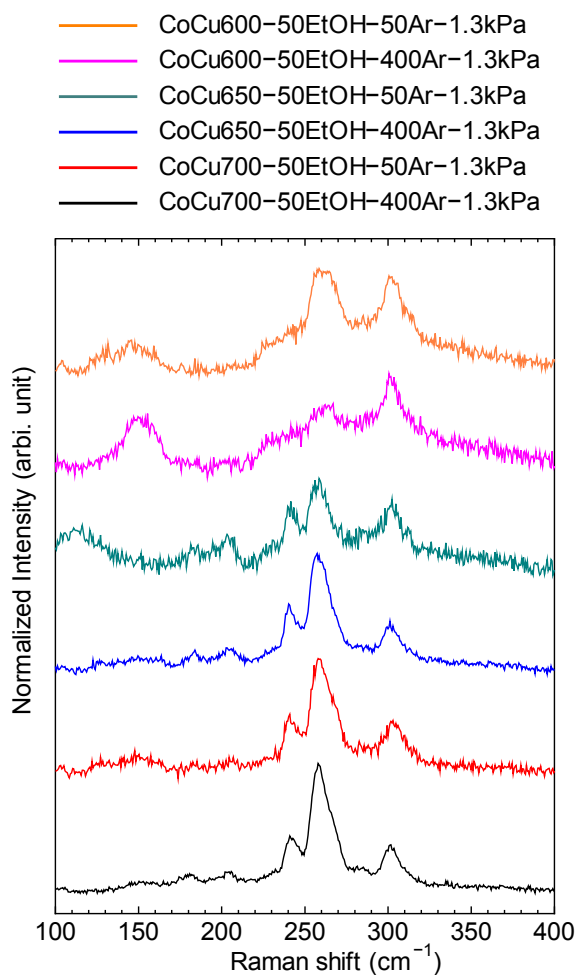
As discussed in the last section, temperature has critical impact on the chiral distribution of SWNTs. In thermodynamics, the temperature and pressure are related with each other. It can be expected that the pressure could also influence the growth of SWNTs. As far as pressure is concerned, both the total pressure and the partial pressure of ethanol may affect the growth of SWNTs. The discussion is firstly focused on the partial pressure, which means that the flow of ethanol is controlled at 50 sccm and diluted by Ar at different flow. The experiment is designed as shown in Table 5- 2.

As shown in **Figure 5- 13**, there is not very clear relationship between the partial pressure and chiral distribution. In fact, at lower temperature, SWNTs with larger diameters started to form. This is possibly because that at low temperature, such as 650 or 600 °C, the activity of the catalysts is much worse compared with that at 800 °C. The feed of carbon stock needs to be much slower and also the total pressure needs to be reduced. The effect of total pressure is further investigated with the condition of 650 °C CVD temperature and EtOH/Ar 50/400 sccm kept.



**Table 5- 2 Experimental design for the effect of pressure on chiral distribution**

Temperature (°C)	Total Pressure (kPa)	Ethanol Flow (sccm)	Argon Flow (sccm)
700	1.3	50	400
700	1.3	50	50
650	1.3	50	400
650	1.3	50	50
650	1.3	50	400
600	1.3	50	50

**Figure 5- 13 RBM of SWNTs grown on Co/Cu catalysts at different total pressure.**

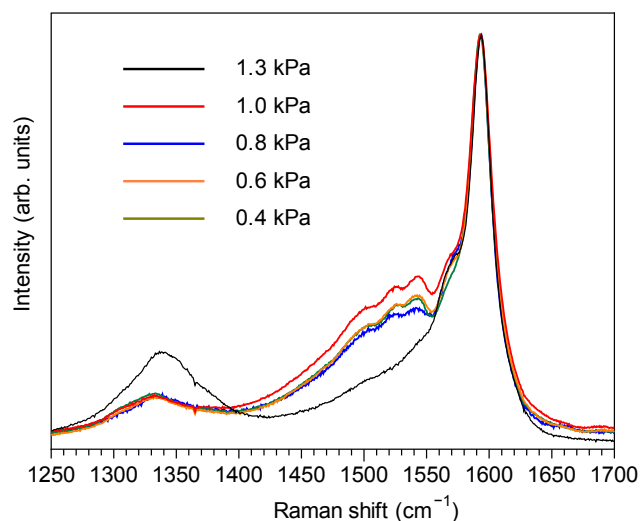


**Figure 5- 14** Raman spectra of SWNTs grown by Co/Cu catalysts at different total pressure.

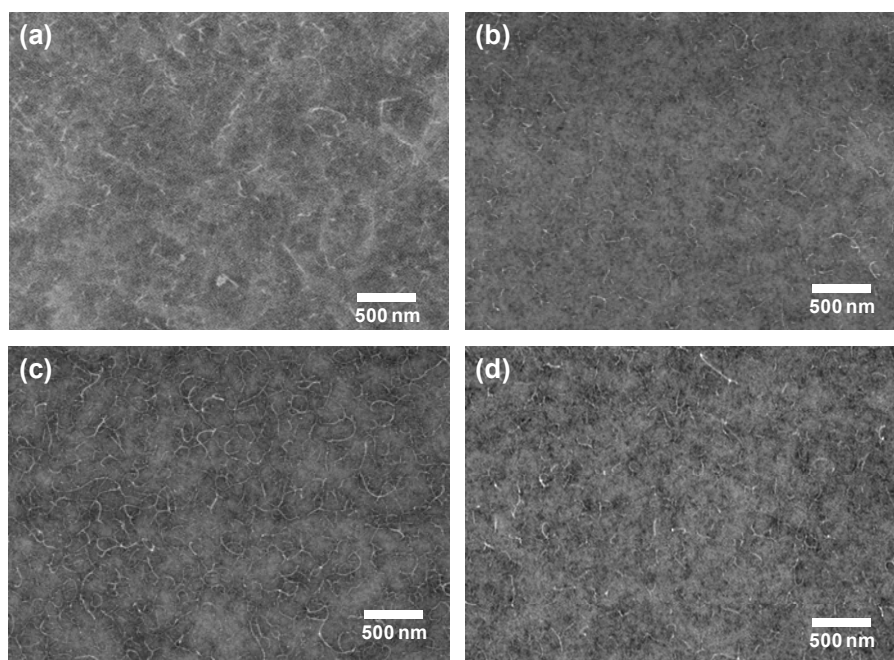


**Figure 5- 15** SEM images of SWNTs grown by Co/Cu catalysts at different total pressure.

As shown in **Figure 5- 14**, with the reduction of the total pressure, the G- band became more and more pronounced, demonstrating the increase of the ratio of smaller-diameter SWNTs. The D band is also significantly suppressed. The improvement in the quality of SWNTs can be reflected from the SEM images (**Figure 5- 15**), where the clean SWNT bundles can be observed clearly at lower pressure.

### 5.4.3 Effect of CVD Time on the Yield of SWNTs

The yield is another equally important issue for the application of SWNTs. Certain thickness and conductivity of the film need to be achieved for device applications. As was discussed in Chapter 4, the growth of VA-SWNTs would be saturated after a certain time. The saturation time is the key factor to control the ultimate thickness of the SWNT films, and may be affected by various experimental conditions, such as precursor flow rate and annealing condition. Besides, the new catalysts combination, Co/Cu, were introduced earlier this Chapter and their growth dynamics is not yet discussed previously.

Usually, the metal oxide rous are reduced in H<sub>2</sub> environment to metallic catalysts. However, as most carbon sources are capable of reducing metal oxide, it is also interesting to investigate the catalytic activity of the directly used metal oxide. The experimental parameter set were designed as: (1) conventional Co/Mo, annealed in vacuum, CVD temperature 800 °C (CoMo 800), flow rate 450 sccm, CVD time 2 min, 5 min and 10 min; (2) Co/Mo catalysts, annealed in H<sub>2</sub>, CVD temperature 800 °C, flow rate 450 sccm, CVD time 3s, 10 s, 30 s, 1 min, 2 min and 10 min; (3) Co/Mo catalysts, annealed in H<sub>2</sub>, CVD temperature 800 °C, flow rate 50 sccm, CVD time 10 min, 20 min; (4) Co/Cu, Co<sub>0.1</sub>/Cu, Co/Mo catalysts, annealed in H<sub>2</sub>, CVD temperature 800 °C, flow rate 50 sccm, CVD time 5 min; (5) Co/Cu catalysts, annealed in H<sub>2</sub>, CVD temperature 750 °C (CoCu750), 700 °C (CoCu700) and 650 °C (CoCu650).

The morphology of the obtained SWNTs is random-oriented film rather than vertical-aligned mat. As shown in the SEM images in **Figure 5- 16**, the SWNT film is well-percolated, with Y-junction as inter-tube connection and small bundles of SWNTs of several micrometers long. The SWNT films grown by 2, 5 and 10 min

ethanol flow are shown in **Figure 5- 16 (a), (b) and (c)**, respectively. With the increase of the CVD time, the SWNT films become thicker and thicker. The transparency of as-synthesized film was characterized by UV-vis-NIR absorption spectroscopy. The transmittances of the CoMo800 grown by 2, 5 and 10 min CVD at 550 nm wavelength, which has the strongest irradiance over the AM1.5G spectrum, are 93.8%, 90.6% and 86.9%. The transmittance is very useful for the application of transparent conductive film. It is highly expected with some mild and steady doping method, the as-grown random-oriented SWNT film is very promising for the application of thin film.

The Co/Mo catalysts control group was characterized first by Raman spectroscopy at 2.54 eV excitation laser. Compared with conventional VA-SWNTs grown by Co/Mo catalysts, the RBM mode of SWNT grown under Ar anneal condition is slightly blue-shifted, which means the average diameter is smaller. However, with the increase of the growth time, the diameter of the random-oriented SWNT film becomes larger and larger, and is almost the same with the VA-SWNT by CoMo800. It is worth mentioning that without the H<sub>2</sub> anneal, the quality of the as-synthesized SWNTs is lower with a relatively larger D-band.

Then the Co/Mo catalysts were annealed before the flow of ethanol. It can be observed that the thickness of VASWNT films could be well controlled from less than 1  $\mu\text{m}$  to around 20  $\mu\text{m}$ . The saturation time is approximately 2 min, as shown in **Figure 5- 19 (a) and (b)** that there was almost no change in the thickness of VA-SWNT grown for 2 min and 10 min. An interesting phenomenon is that the vertical alignment existed down to 700 nm thickness, as shown in **Figure 5- 19 (f) and (g)**.

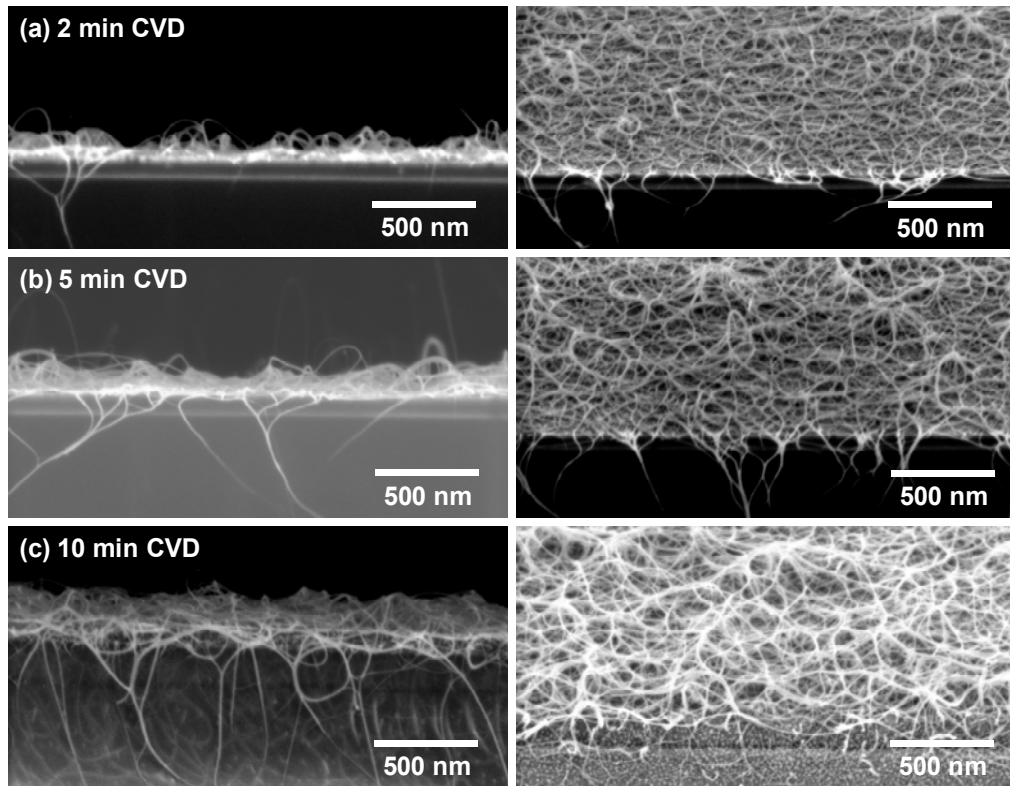


Figure 5- 16 Morphologies of the as-synthesized random-oriented SWNT films using Co/Mo catalysts by different CVD Time.

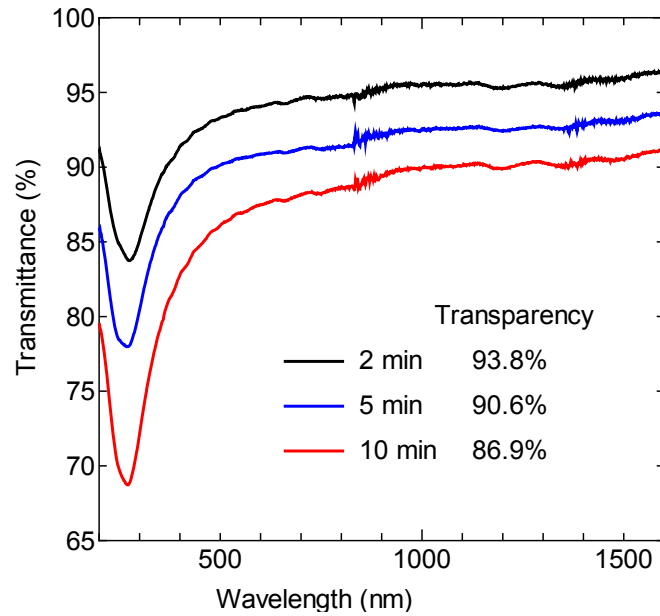
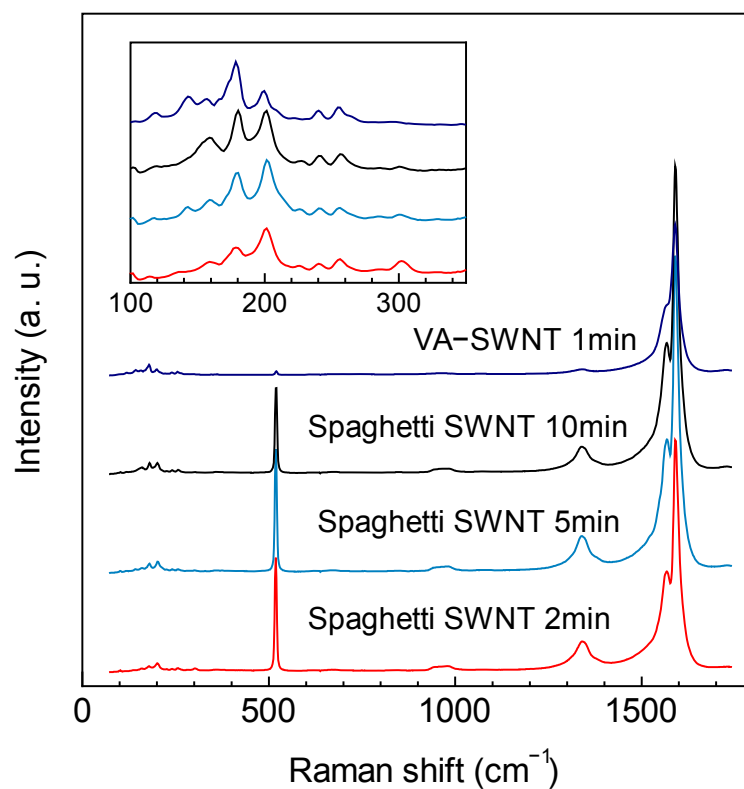
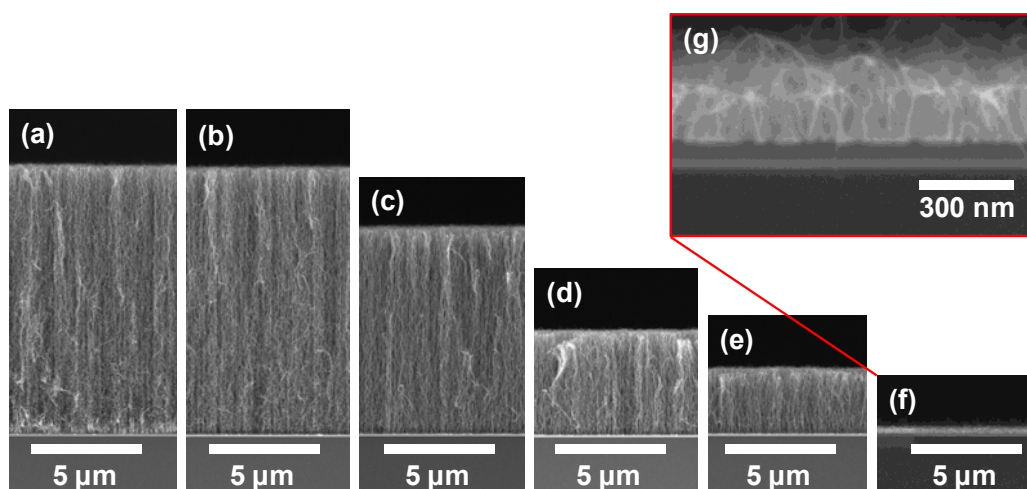


Figure 5- 17 Transmittance of as-synthesized random-oriented SWNT films using Co/Mo catalysts by different CVD Time.



**Figure 5- 18** Raman spectra of the as-synthesized random-oriented and vertical-aligned SWNT films using Co/Mo catalysts.



**Figure 5- 19** (a)-(f) Morphologies of the as-synthesized Vertically Aligned SWNT films using Co/Mo catalysts by different CVD Time. (g) Magnified SEM image of (f).

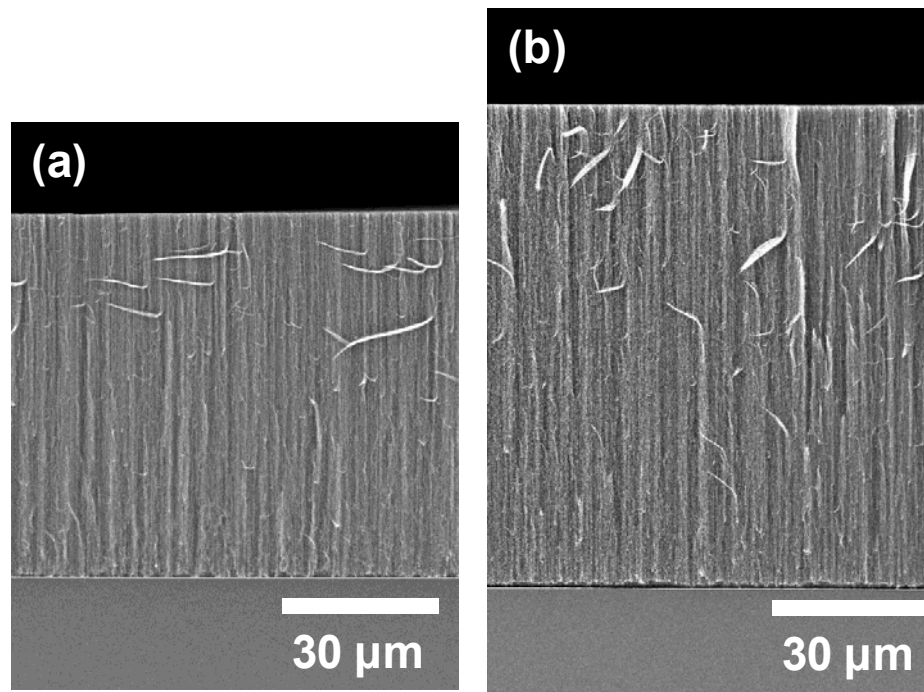


Figure 5- 20 Morphologies of the as-synthesized vertically aligned SWNT films using Co/Mo catalysts by different CVD Time with the ethanol flow rate of 50 sccm.

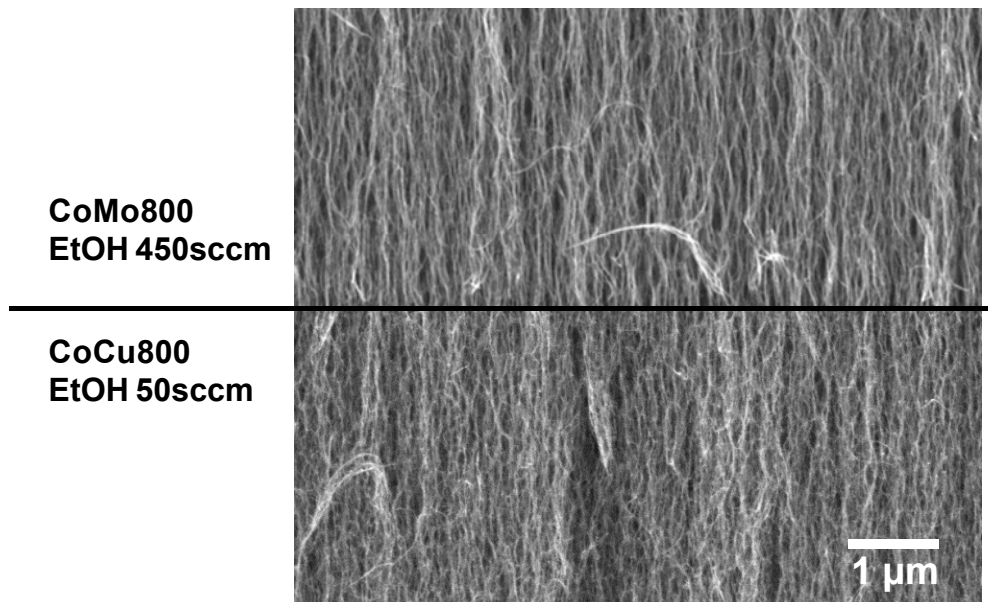


Figure 5- 21 Comparison of the morphology of the as-synthesized VA-SWNTs by different catalysts combination at the same temperature using SEM.

However, when the flow rate is decreased to 50 sccm, the saturation time was substantially elongated and the thickness of the VA-SWNT film was increased to 100  $\mu\text{m}$ . As shown in **Figure 5- 20**, with the same CVD time 10 min, the thickness of the VA-SWNTs by 50 sccm ethanol flow is 70  $\mu\text{m}$  compared with 12  $\mu\text{m}$  by 450 sccm. The growth of VA-SWNTs were slowed down afterwards but still reached 100  $\mu\text{m}$  when the CVD time is 20 min. This is the first time to achieve such a thick VA-SWNT film with high quality which is very promising for the spinning of SWNTs.

**Figure 5- 21** shows the SEM image of the comparison of the as-synthesized VA-SWNT by CoMo800 and CoCu800. The SWNTs synthesized by CoCu800 growth condition demonstrated very good vertical alignment. It can be observed that the SWNTs synthesized by CoCu800 growth condition is slightly ‘hairy’ than that by CoMo800 condition. The ‘hairy’ nanotube may be because of the smaller diameter, although further experimental proof is needed.

Raman spectroscopy was used to characterize the quality and the diameter of the SWNTs. As shown in the left panel of **Figure 5- 22**, it is very clear that the main RBM mode was shifted from 180  $\text{cm}^{-1}$  to 250  $\text{cm}^{-1}$ , which means the diameter was decreased to smaller than 1 nm. Using the above-discussed Equation (5-1), the average diameter of the SWNT synthesized by Co<sub>0.1</sub>Cu<sub>800</sub> growth condition can be calculated as 0.98 nm. This is the first experimental result reporting the VA-SWNTs with average diameter smaller than 1 nm. We expect further decrease of the diameter and narrower distribution of the chiralities of the as-synthesized VA-SWNTs by changing the catalysts concentration or varying the growth temperature. Elongation of the CVD time from 2 min to 10 min made it possible for a very thin VA-SWNT film with (6,5), (7,5) and (7,6)-enriched chiralities, as shown in **Figure 5- 23**.



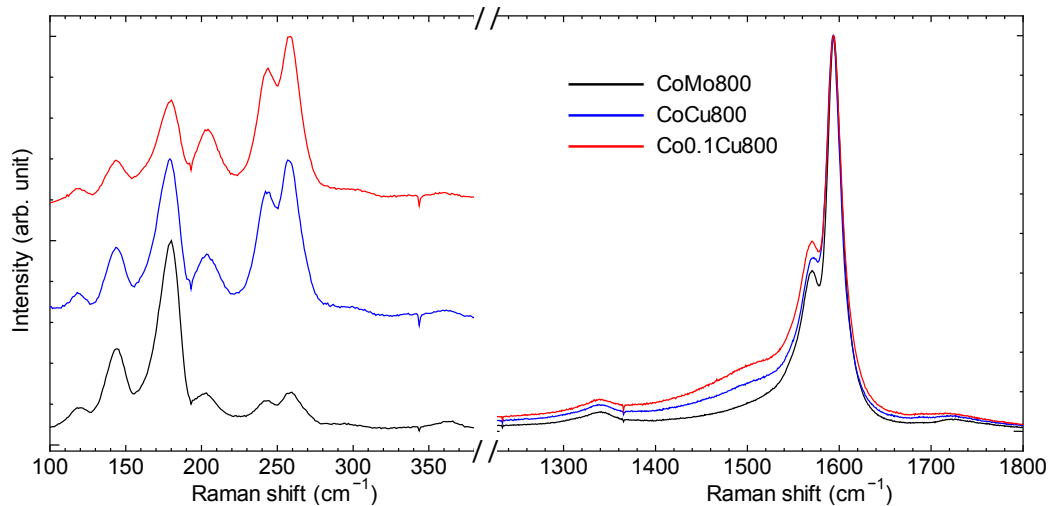


Figure 5- 22 Comparison of Raman spectra of SWNTs synthesized from Co/Cu, Co<sub>0.1</sub>/Cu and Co/Mo at different temperatures. The laser excitation energy is 2.54 eV.

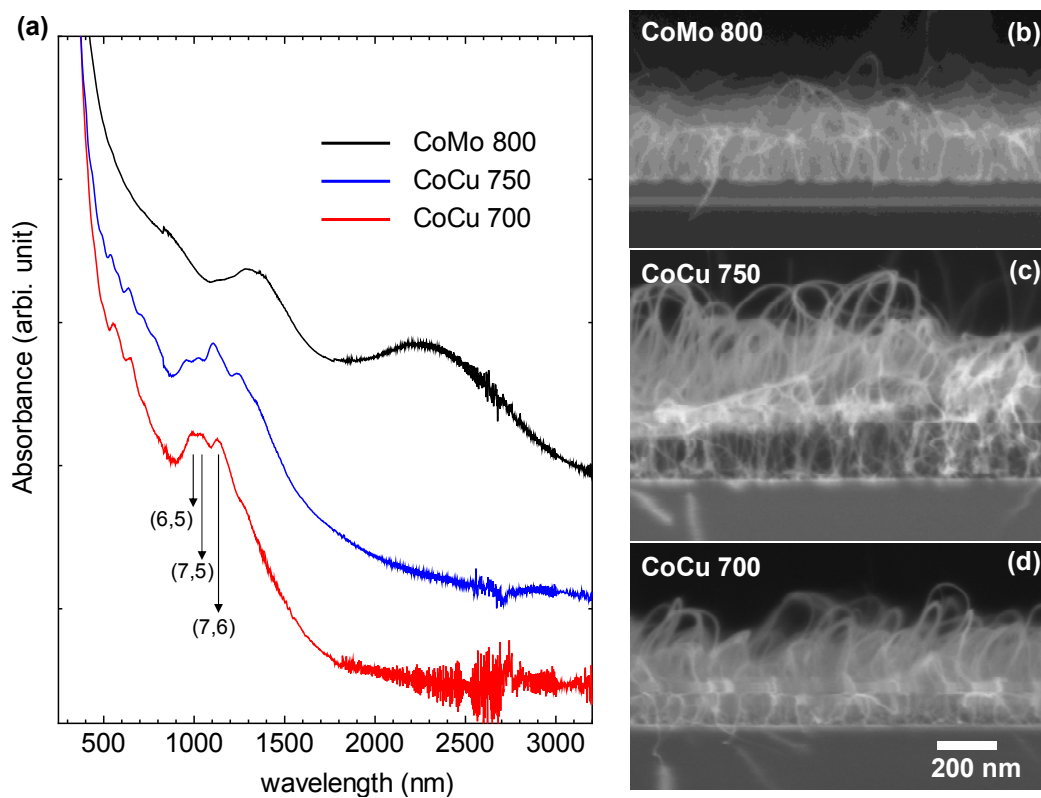


Figure 5- 23 (a) Absorption spectra of SWNTs synthesized by different catalysts and temperature. (b-d) SEM images of corresponding SWNTs.

Finally, the growth dynamics of the newly proposed catalysts are investigated. As shown in **Figure 5- 23**, the vertical alignment of sub-nanometer-diameter SWNTs was achieved for the first time. Although the thickness was only several tens of nanometers, the high-quality small-diameter VA-SWNTs were observed for the first time. Further experimental investigations like *in-situ* TEM were necessary to explain the growth dynamics.

## 5.5 Summary

By using Co-Cu catalysts, high-quality VA-SWNTs with average diameter smaller than 1 nm have been grown on the substrate for the first time. Moreover, by annealing Co-Cu catalysts in low-pressure Ar environment, high-quality random-oriented SWNTs with average diameter of 0.8 nm has been grown on the substrate for the first time. It is very promising if the diameter could be further reduced and the chiralities could be further narrowed down to (7,5) and (6,5). The yield of both the VA-SWNT and random-oriented SWNT films can be tuned by changing CVD time.

# Chapter 6

## Conclusions

Single-walled carbon nanotubes (SWNTs) possess excellent optical, electrical, mechanical and thermal properties as well as chemical stability. Specifically, for the light harvesting application, SWNTs have the superiorities in terms of the wide spectrum of absorption ranging from near-infrared to visible wavelength, high electrical conductivity at high transparency as well as the multiple exciton generation. Combined with earth abundance and chemical stability, the SWNT is supposed to be a very promising candidate for next-generation solar cell applications. However, three main challenges have hindering the full exploitation of SWNTs for the solar cell applications: (1) The SWNTs synthesized on substrates or by floating catalysts have too large diameter. The reduction of the diameter of SWNTs from 2 nm to 1 nm would lead to the increase of the band gap from 0.5 eV to 1.2 eV which is possible for the applications of solar cells. However, this has not been achieved so far. This is the challenge at the nanoscale. (2) The one-dimensional SWNTs do not grow into a

three-dimensional bulk like conventional semiconductors. The gap between the properties of SWNT assemblies and the individual SWNTs is the challenge at the microscale. (3) Before the first two challenges are solved, the technique of amounting SWNTs to photovoltaic devices needs further investigation and understanding, which could be categorized into the challenge at the macroscale. This doctoral thesis aims at controlling the structures and properties of single-walled carbon nanotube (SWNTs) at the macroscale, microscale and nanoscale level for the applications of high-performance solar cells.

## **6.1 Contributions to the Research of SWNTs at Macroscale Level**

The SWNT/Si solar cells are drawing emerging attentions owing to their simple and efficient structure. The power conversion efficiencies (PCEs) of SWNT/Si solar cells have been improved an order of magnitude during last five years. However, the so-far-reported peak PCEs of the SWNT/Si solar cells were all suffered from degradation, which is hindering their further applications. The SWNT/Si solar cells could lose almost 50% PCE after hours in air, and even with protection, the PCE still degraded by 20%. This could be attributed to that the peak PCEs were boosted by nitric acid or gold salt doping which were very instable. Another issue remained controversial is the working mechanism of the SWNT/Si solar cells. Initially, the SWNT/Si solar cell was proposed as a *p-n* heterojunction. Based on this hypothesis, (6,5) enriched SWNTs were used to further increase the built-in potential. However, the incident photon conversion efficiency (IPCE) spectrum of the SWNT/Si solar cells showed no obvious relationship with the SWNT absorption spectrum. In addition, the efficiency of graphene/Si solar cell became comparable with that of the SWNT/Si solar cell. The SWNT/Si solar cells were considered as a Schottky-barrier junction. One characteristic that could distinguish the *p-n* junction and the Schottky-barrier junction is the effect of the interfacial oxide layer. For a conventional Schottky-barrier

junction, inserting an interfacial oxide layer between the metal electrode and semiconductor would eliminate the pinning of Fermi level and thus improve the PCE, while the opposite case applies for a *p-n* junction. Until now, both significant improvement and degradation of the PCEs were obtained after the removal of the interfacial oxide layer. These contradictory results call for more solid experimental proof for the further understanding of the SWNT/Si solar cells. By using the excellent optical and electrical of the pristine SWNTs with long bundle length, we present the single-walled carbon nanotube/silicon (SWNT/Si) solar cells of 11% power conversion efficiency (PCE) without doping. The PCEs of the fabricated solar cells even slightly increased after 10-month ambient exposure without any external protection. The open-circuit voltage of the SWNT/Si solar cells under low light intensities down to 10 mW/cm<sup>2</sup> demonstrated characteristics of the ideal *p-n* junction model. The mechanism was discussed through the effect of varying the interfacial oxide layer thickness between the SWNTs and Si on the solar cell performance. The high efficiency and stability demonstrated in this study make SWNT/Si solar cells one of practical choices for next generation energy system. This part of work has been published on Journal of Materials Chemistry A: Materials for Energy and Sustainability, with TOC graphic shown in **Figure 6- 1**.

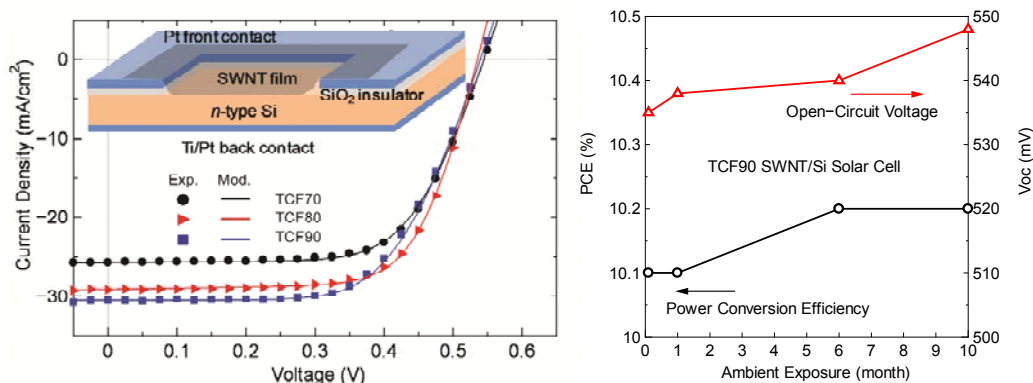


**Figure 6- 1** Air-stable high-efficiency solar cells with dry-transferred SWNTs

## 6.2 Contributions to the Research of SWNTs at Microscale Level

Self-assembly is a high-yield and low-cost method that builds low-dimensional materials into three-dimensional micro/macro-architectures with various morphologies. Capillary forces have been used to direct the self-assembling of patterned arrays of nanowires, nanopillars and multi-walled carbon nanotubes (MWNTs) into hierarchical networks. However, due to the hydrophobicity and significantly smaller diameter of SWNTs, wetting vertically aligned SWNTs (VA-SWNTs) results in a high-density bulk with millimeter-scale cracks rather than the hierarchical honeycomb-like network formed by MWNT arrays. So far, such a honeycomb structure of SWNTs has been achieved only by film-casting anionic shortened SWNTs–cationic ammonium lipid conjugates in organic solution, of which the complicated solution preparation induces defects and degradation of SWNTs. We propose a water vapor treatment to direct the formation of single-walled carbon nanotubes (SWNTs) into a self-assembled micro-honeycomb network ( $\mu$ -HN) for the application to SWNT-Si solar cells. The  $\mu$ -HN consists of vertical aggregated SWNT walls and a buckypaper bottom. This hierarchical structure is much easier to prepare and has competitive optical and electrical properties compared with buckypaper. Varying the water reservoir temperature and vapor exposure time of water vapor treatment results in different morphologies. The pristine  $\mu$ -HN SWNT-Si solar cell shows a record-high fill factor of 72% as well as a power conversion efficiency (PCE) of 6% without optimizing the diameter or height of the vertically aligned SWNTs. The FF represents the quality of a solar cell, and is one of three parameters characterizing solar cell performance along with  $V_{oc}$  and  $J_{sc}$ . The significant improvement in FF and ideality factor over previously reported values is attributed to the hierarchical  $\mu$ -HN, which simultaneously enhances carrier separation, collection and transport. The dense, cross-linked SWNT walls in the  $\mu$ -HN act as efficient conduction pathways, essentially serving as a micro-grid electrode to collect the

charge carriers generated from the adjacent micro-honeycomb cells. The micro-grid configuration in the  $\mu$ -HN significantly shortens the minimum carrier diffusion path, resulting in more efficient photocurrent collection. In the solar cells fabricated using collapsed HN and porous HN, the micro-grid configuration still exists, which leads to the quite high FFs. The PCE exceeding 10% is achieved in the dry state after dilute nitric acid treatment. The main part of work has been published on the Journal of Physical Chemistry Letters, with the TOC graphics shown in **Figure 6- 2**. And some of the results have been published on the Journal of Nanoscience and Nanotechnology, and the Proceedings of the 15<sup>th</sup> International Heat Transfer Conference.

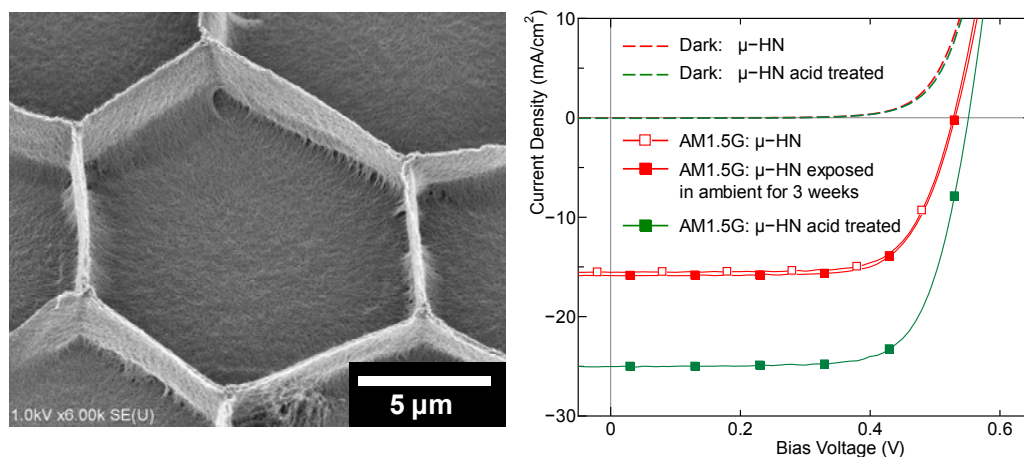


**Figure 6- 2** Self-assembled microhoneycomb network of SWNTs for solar cells

### 6.3 Contributions to the Research of SWNTs at Nanoscale Level

We synthesized the vertically aligned SWNT with average diameter as small as 0.9 nm directly on the substrate for the first time. The band gap of the 0.9 nm-diameter SWNTs is 1.1 eV, which is possible to be used for solar cell applications without post-processing techniques, such as separation and dispersion. The key to realize such a small diameter is by using cobalt and copper bimetallic nanoparticle

catalysts. When the CVD temperature is decreased to 650 °C, the majority of chiralities of the as-synthesized SWNTs is limited to (6,5) and (7,5), which are supposed to be the most useful SWNTs for solar cell applications. This part of work is still under preparation for the contribution to a peer-reviewed journal.

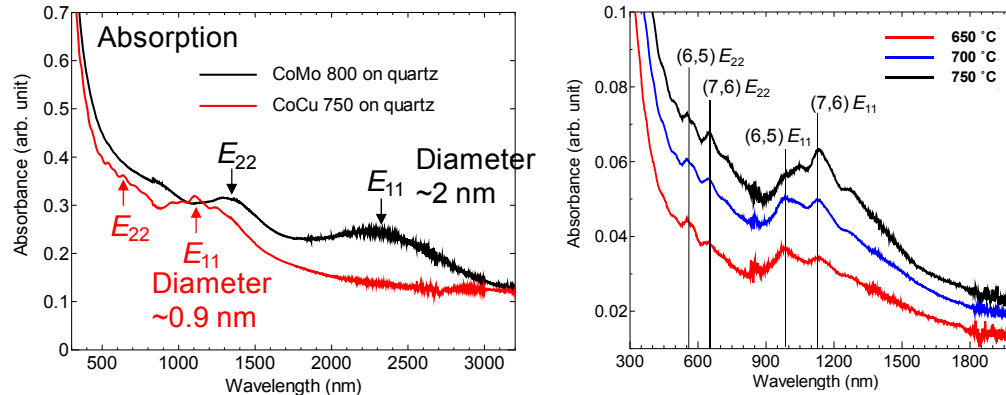


Figure 6- 3 Growth of sub-nanometer-diameter SWNTs films directly on substrate

## 6.4 Summary

To sum up, this doctoral thesis has made original contributions on controlling the structures and properties of single-walled carbon nanotube (SWNTs) at the macroscale, microscale and nanoscale level for the applications of high-performance solar cells: (1) Air-stable high-performance SWNT/Si solar cell with 11% efficiency has been realized for the first time; (2) The self-assembled microhoneycomb network of SWNTs has been proposed and realized for the first time; (3) The vertical-aligned and random-oriented SWNTs with the average diameter of 0.9 nm have realized for the first time.



# Bibliography

- [1] H. W. Kroto, J. R. Heath, S. C. O'Brien, R. F. Curl, and R. E. Smalley, "C<sub>60</sub>: Buckminsterfullerene," *Nature*, vol. 318, pp. 162-163, 1985.
- [2] A. K. Geim and K. S. Novoselov, "The rise of graphene," *Nature Materials*, vol. 6, pp. 183-191, 2007.
- [3] K. S. Novoselov, A. K. Geim, S. V. Morozov, D. Jiang, Y. Zhang, S. V. Dubonos, I. V. Grigorieva, and A. A. Firsov, "Electric Field Effect in Atomically Thin Carbon Films," *Science*, vol. 306, pp. 666-669, 2004.
- [4] S. Iijima, "Helical microtubules of graphitic carbon," *Nature*, vol. 354, pp. 56-58, 1991.
- [5] S. Iijima and T. Ichihashi, "Single-shell carbon nanotubes of 1-nm diameter," *Nature*, vol. 363, pp. 603-605, 1993.
- [6] S. Riichiro, G. Dresselhaus, and M. Dresselhaus, *Physical Properties of Carbon Nanotubes*: Imperial College Press, 1998.
- [7] S. Maruyama, R. Kojima, Y. Miyauchi, S. Chiashi, and M. Kohno, "Low-temperature synthesis of high-purity single-walled carbon nanotubes from alcohol," *Chemical Physics Letters*, vol. 360, pp. 229-234, 2002.
- [8] M. S. Dresselhaus, G. Dresselhaus, R. Saito, and A. Jorio, "Raman spectroscopy of carbon nanotubes," *Physics Reports*, vol. 409, pp. 47-99, 2005.
- [9] H. Telg, J. G. Duque, M. Staiger, X. Tu, F. Hennrich, M. M. Kappes, M. Zheng, J. Maultzsch, C. Thomsen, and S. K. Doorn, "Chiral Index Dependence of the G<sup>+</sup> and G<sup>-</sup> Raman Modes in Semiconducting Carbon Nanotubes," *ACS Nano*, vol. 6, pp. 904-911, 2011.
- [10] W. Shockley and H. J. Queisser, "Detailed Balance Limit of Efficiency of p - n Junction Solar Cells," *Journal of Applied Physics*, vol. 32, pp. 510-519, 1961.
- [11] M. S. Leite, R. L. Woo, J. N. Munday, W. D. Hong, S. Mesropian, D. C. Law, and H. A. Atwater, "Towards an optimized all lattice-matched InAlAs/InGaAsP/InGaAs multijunction solar cell with efficiency 50%," *Applied Physics Letters*, vol. 102, pp. -, 2013.
- [12] P. Avouris, M. Freitag, and V. Perebeinos, "Carbon-nanotube photonics and optoelectronics," *Nature Photonics*, vol. 2, pp. 341-350, 2008.
- [13] D. Jariwala, V. K. Sangwan, L. J. Lauhon, T. J. Marks, and M. C. Hersam, "Carbon nanomaterials for electronics, optoelectronics, photovoltaics, and sensing," *Chemical Society*

- Reviews*, vol. 42, pp. 2824-2860, 2013.
- [14] A. M. Marconnet, M. A. Panzer, and K. E. Goodson, "Thermal conduction phenomena in carbon nanotubes and related nanostructured materials," *Reviews of Modern Physics*, vol. 85, pp. 1295-1326, 2013.
- [15] A. G. Nasibulin, A. Kaskela, K. Mustonen, A. S. Anisimov, V. Ruiz, S. Kivistö, S. Rackauskas, M. Y. Timmermans, M. Pudas, B. Aitchison, M. Kauppinen, D. P. Brown, O. G. Okhotnikov, and E. I. Kauppinen, "Multifunctional Free-Standing Single-Walled Carbon Nanotube Films," *ACS Nano*, vol. 5, pp. 3214-3221, 2011.
- [16] A. Kaskela, A. G. Nasibulin, M. Y. Timmermans, B. Aitchison, A. Papadimitratos, Y. Tian, Z. Zhu, H. Jiang, D. P. Brown, A. Zakhidov, and E. I. Kauppinen, "Aerosol-Synthesized SWCNT Networks with Tunable Conductivity and Transparency by a Dry Transfer Technique," *Nano Letters*, vol. 10, pp. 4349-4355, 2010.
- [17] Z. Wu, Z. Chen, X. Du, J. M. Logan, J. Sippel, M. Nikolou, K. Kamaras, J. R. Reynolds, D. B. Tanner, A. F. Hebard, and A. G. Rinzler, "Transparent, Conductive Carbon Nanotube Films," *Science*, vol. 305, pp. 1273-1276, 2004.
- [18] N. M. Gabor, "Impact Excitation and Electron-Hole Multiplication in Graphene and Carbon Nanotubes," *Accounts of Chemical Research*, vol. 46, pp. 1348-1357, 2013.
- [19] N. M. Gabor, Z. Zhong, K. Bosnick, J. Park, and P. L. McEuen, "Extremely Efficient Multiple Electron-Hole Pair Generation in Carbon Nanotube Photodiodes," *Science*, vol. 325, pp. 1367-1371, 2009.
- [20] R. H. Baughman, A. A. Zakhidov, and W. A. de Heer, "Carbon Nanotubes--the Route Toward Applications," *Science*, vol. 297, pp. 787-792, 2002.
- [21] M. F. L. De Volder, S. H. Tawfik, R. H. Baughman, and A. J. Hart, "Carbon Nanotubes: Present and Future Commercial Applications," *Science*, vol. 339, pp. 535-539, 2013.
- [22] J. Wei, Y. Jia, Q. Shu, Z. Gu, K. Wang, D. Zhuang, G. Zhang, Z. Wang, J. Luo, A. Cao, and D. Wu, "Double-Walled Carbon Nanotube Solar Cells," *Nano Letters*, vol. 7, pp. 2317-2321, 2007.
- [23] Y. Jia, J. Wei, K. Wang, A. Cao, Q. Shu, X. Gui, Y. Zhu, D. Zhuang, G. Zhang, B. Ma, L. Wang, W. Liu, Z. Wang, J. Luo, and D. Wu, "Nanotube-Silicon Heterojunction Solar Cells," *Advanced Materials*, vol. 20, pp. 4594-4598, 2008.
- [24] O. Pang-Leen, B. E. William, and A. L. Igor, "Hybrid solar cells based on single-walled carbon nanotubes/Si heterojunctions," *Nanotechnology*, vol. 21, p. 105203, 2010.
- [25] Y. Jia, A. Cao, X. Bai, Z. Li, L. Zhang, N. Guo, J. Wei, K. Wang, H. Zhu, D. Wu, and P. M. Ajayan, "Achieving High Efficiency Silicon-Carbon Nanotube Heterojunction Solar Cells by Acid Doping," *Nano Letters*, vol. 11, pp. 1901-1905, 2011.
- [26] Y. Jia, P. Li, X. Gui, J. Wei, K. Wang, H. Zhu, D. Wu, L. Zhang, A. Cao, and Y. Xu, "Encapsulated carbon nanotube-oxide-silicon solar cells with stable 10% efficiency," *Applied*

- Physics Letters*, vol. 98, pp. 133115-3, 2011.
- [27] Y. Jung, X. Li, N. K. Rajan, A. D. Taylor, and M. A. Reed, "Record High Efficiency Single-Walled Carbon Nanotube/Silicon p-n Junction Solar Cells," *Nano Letters*, vol. 13, pp. 95-99, 2012.
- [28] D. Kozawa, K. Hiraoka, Y. Miyauchi, S. Mouri, and K. Matsuda, "Analysis of the Photovoltaic Properties of Single-Walled Carbon Nanotube/Silicon Heterojunction Solar Cells," *Applied Physics Express*, vol. 5, 2012.
- [29] E. Shi, L. Zhang, Z. Li, P. Li, Y. Shang, Y. Jia, J. Wei, K. Wang, H. Zhu, D. Wu, S. Zhang, and A. Cao, "TiO<sub>2</sub>-Coated Carbon Nanotube-Silicon Solar Cells with Efficiency of 15%," *Scientific Reports*, vol. 2, p. 884, 2012.
- [30] D. D. Tune, B. S. Flavel, R. Krupke, and J. G. Shapter, "Carbon Nanotube-Silicon Solar Cells," *Advanced Energy Materials*, vol. 2, pp. 1043-1055, 2012.
- [31] J. Di, Z. Yong, X. Zheng, B. Sun, and Q. Li, "Aligned Carbon Nanotubes for High-Efficiency Schottky Solar Cells," *Small*, vol. 9, pp. 1367-1372, 2013.
- [32] X. Li, Y. Jung, K. Sakimoto, T.-H. Goh, M. A. Reed, and A. D. Taylor, "Improved efficiency of smooth and aligned single walled carbon nanotube/silicon hybrid solar cells," *Energy & Environmental Science*, vol. 6, pp. 879-887, 2013.
- [33] D. Kozawa, K. Hiraoka, Y. Miyauchi, S. Mouri, and K. Matsuda, "Analysis of the Photovoltaic Properties of Single-Walled Carbon Nanotube/Silicon Heterojunction Solar Cells," *Applied Physics Express*, vol. 5, p. 042304, 2012.
- [34] E. Shi, H. Li, L. Yang, L. Zhang, Z. Li, P. Li, Y. Shang, S. Wu, X. Li, J. Wei, K. Wang, H. Zhu, D. Wu, Y. Fang, and A. Cao, "Colloidal Antireflection Coating Improves Graphene-Silicon Solar Cells," *Nano Letters*, vol. 13, pp. 1776-1781, 2013.
- [35] E. Shi, L. Zhang, Z. Li, P. Li, Y. Shang, Y. Jia, J. Wei, K. Wang, H. Zhu, D. Wu, S. Zhang, and A. Cao, "TiO<sub>2</sub>-Coated Carbon Nanotube-Silicon Solar Cells with Efficiency of 15%," *Scientific Reports*, vol. 2, 2012.
- [36] Y. Jia, A. Cao, F. Kang, P. Li, X. Gui, L. Zhang, E. Shi, J. Wei, K. Wang, H. Zhu, and D. Wu, "Strong and reversible modulation of carbon nanotube-silicon heterojunction solar cells by an interfacial oxide layer," *Physical Chemistry Chemical Physics*, vol. 14, pp. 8391-8396, 2012.
- [37] D.-m. Sun, M. Y. Timmermans, Y. Tian, A. G. Nasibulin, E. I. Kauppinen, S. Kishimoto, T. Mizutani, and Y. Ohno, "Flexible high-performance carbon nanotube integrated circuits," *Nat Nano*, vol. 6, pp. 156-161, 2011.
- [38] M. P. Ramuz, M. Vosgueritchian, P. Wei, C. Wang, Y. Gao, Y. Wu, Y. Chen, and Z. Bao, "Evaluation of Solution-Processable Carbon-Based Electrodes for All-Carbon Solar Cells," *ACS Nano*, vol. 6, pp. 10384-10395, 2012.
- [39] Y. Jia, P. Li, X. Gui, J. Wei, K. Wang, H. Zhu, D. Wu, L. Zhang, A. Cao, and Y. Xu, "Encapsulated carbon nanotube-oxide-silicon solar cells with stable 10% efficiency," *Applied*

## Bibliography

---

- Physics Letters*, vol. 98, pp. -, 2011.
- [40] P. Wadhwa, B. Liu, M. A. McCarthy, Z. Wu, and A. G. Rinzler, "Electronic Junction Control in a Nanotube-Semiconductor Schottky Junction Solar Cell," *Nano Letters*, vol. 10, pp. 5001-5005, 2010.
- [41] K. Cui, T. Chiba, S. Omiya, T. Thurakitserree, P. Zhao, S. Fujii, H. Kataura, E. Einarsson, S. Chiashi, and S. Maruyama, "Self-Assembled Microhoneycomb Network of Single-Walled Carbon Nanotubes for Solar Cells," *The Journal of Physical Chemistry Letters*, vol. 4, pp. 2571-2576, 2013.
- [42] D. R. Lillington and W. G. Townsend, "Effects of interfacial oxide layers on the performance of silicon Schottky - barrier solar cells," *Applied Physics Letters*, vol. 28, pp. 97-98, 1976.
- [43] J. Shewchun, R. Singh, and M. A. Green, "Theory of metal - insulator - semiconductor solar cells," *Journal of Applied Physics*, vol. 48, pp. 765-770, 1977.
- [44] M. Morita, T. Ohmi, E. Hasegawa, M. Kawakami, and M. Ohwada, "Growth of native oxide on a silicon surface," *Journal of Applied Physics*, vol. 68, pp. 1272-1281, 1990.
- [45] G. Mende, "Oxidation of etched silicon in air at room temperature," *Surface Science*, vol. 128, pp. 169-175, 1983.
- [46] T. Engel, "The interaction of molecular and atomic oxygen with Si(100) and Si(111)," *Surface Science Reports*, vol. 18, pp. 93-144, 1993.
- [47] A. A. Balandin, "Thermal properties of graphene and nanostructured carbon materials," *Nature Materials*, vol. 10, pp. 569-581, 2011.
- [48] S. Berber, Y.-K. Kwon, and D. Tománek, "Unusually High Thermal Conductivity of Carbon Nanotubes," *Physical Review Letters*, vol. 84, pp. 4613-4616, 2000.
- [49] S. Maruyama, "A molecular dynamics simulation of heat conduction in finite length SWNTs," *Physica B: Condensed Matter*, vol. 323, pp. 193-195, 2002.
- [50] R. S. Prasher, X. J. Hu, Y. Chalopin, N. Mingo, K. Lofgreen, S. Volz, F. Cleri, and P. Keblinski, "Turning Carbon Nanotubes from Exceptional Heat Conductors into Insulators," *Physical Review Letters*, vol. 102, p. 105901, 2009.
- [51] H. Duan and K. K. Berggren, "Directed Self-Assembly at the 10 nm Scale by Using Capillary Force-Induced Nanocoheion," *Nano Letters*, vol. 10, pp. 3710-3716, 2010.
- [52] B. Pokroy, S. H. Kang, L. Mahadevan, and J. Aizenberg, "Self-Organization of a Mesoscale Bristle into Ordered, Hierarchical Helical Assemblies," *Science*, vol. 323, pp. 237-240, 2009.
- [53] X. Lim, H. W. G. Foo, G. H. Chia, and C.-H. Sow, "Capillarity-Assisted Assembly of Carbon Nanotube Microstructures with Organized Initiations," *ACS Nano*, vol. 4, pp. 1067-1075, 2010.
- [54] M. De Volder, S. H. Tawfick, S. J. Park, D. Copic, Z. Zhao, W. Lu, and A. J. Hart, "Diverse 3D Microarchitectures Made by Capillary Forming of Carbon Nanotubes," *Advanced*

- Materials*, vol. 22, pp. 4384-4389, 2010.
- [55] M. De Volder and A. J. Hart, "Engineering Hierarchical Nanostructures by Elastocapillary Self-Assembly," *Angewandte Chemie International Edition*, vol. 52, pp. 2412-2425, 2013.
- [56] S. Tawfick, M. De Volder, and A. J. Hart, "Structurally Programmed Capillary Folding of Carbon Nanotube Assemblies," *Langmuir*, vol. 27, pp. 6389-6394, 2011.
- [57] D. N. Futaba, K. Hata, T. Yamada, T. Hiraoka, Y. Hayamizu, Y. Kakudate, O. Tanaike, H. Hatori, M. Yumura, and S. Iijima, "Shape-engineerable and highly densely packed single-walled carbon nanotubes and their application as super-capacitor electrodes," *Nature Materials*, vol. 5, pp. 987-994, 2006.
- [58] N. Chakrapani, B. Wei, A. Carrillo, P. M. Ajayan, and R. S. Kane, "Capillarity-driven assembly of two-dimensional cellular carbon nanotube foams," *Proceedings of the National Academy of Sciences*, vol. 101, pp. 4009-4012, 2004.
- [59] H. Liu, S. Li, J. Zhai, H. Li, Q. Zheng, L. Jiang, and D. Zhu, "Self-Assembly of Large-Scale Micropatterns on Aligned Carbon Nanotube Films," *Angewandte Chemie International Edition*, vol. 43, pp. 1146-1149, 2004.
- [60] A. W. Adamson and A. P. Gast, *Physical Chemistry of Surfaces*. New York: Wiley, 1997.
- [61] Y. Murakami, S. Chiashi, Y. Miyauchi, M. Hu, M. Ogura, T. Okubo, and S. Maruyama, "Growth of vertically aligned single-walled carbon nanotube films on quartz substrates and their optical anisotropy," *Chemical Physics Letters*, vol. 385, pp. 298-303, 2004.
- [62] Y. Murakami, Y. Miyauchi, S. Chiashi, and S. Maruyama, "Direct synthesis of high-quality single-walled carbon nanotubes on silicon and quartz substrates," *Chemical Physics Letters*, vol. 377, pp. 49-54, 2003.
- [63] E. Einarsson, Y. Murakami, M. Kadowaki, and S. Maruyama, "Growth dynamics of vertically aligned single-walled carbon nanotubes from in situ measurements," *Carbon*, vol. 46, pp. 923-930, 2008.
- [64] S. Maruyama, E. Einarsson, Y. Murakami, and T. Edamura, "Growth process of vertically aligned single-walled carbon nanotubes," *Chemical Physics Letters*, vol. 403, pp. 320-323, 2005.
- [65] Y. Murakami and S. Maruyama, "Detachment of vertically aligned single-walled carbon nanotube films from substrates and their re-attachment to arbitrary surfaces," *Chemical Physics Letters*, vol. 422, pp. 575-580, 2006.
- [66] R. Xiang, E. Einarsson, Y. Murakami, J. Shiomi, S. Chiashi, Z. Tang, and S. Maruyama, "Diameter Modulation of Vertically Aligned Single-Walled Carbon Nanotubes," *ACS Nano*, vol. 6, pp. 7472-7479, 2012.
- [67] T. Thurakitserree, C. Kramberger, P. Zhao, S. Aikawa, S. Harish, S. Chiashi, E. Einarsson, and S. Maruyama, "Diameter-controlled and nitrogen-doped vertically aligned single-walled carbon nanotubes," *Carbon*, vol. 50, pp. 2635-2640, 2012.

## Bibliography

---

- [68] T. Thurakitseeree, C. Kramberger, P. Zhao, S. Chiashi, E. Einarsson, and S. Maruyama, "Reduction of single-walled carbon nanotube diameter to sub-nm via feedstock," *physica status solidi (b)*, vol. 249, pp. 2404-2407, 2012.
- [69] R. Xiang, T. Wu, E. Einarsson, Y. Suzuki, Y. Murakami, J. Shiomi, and S. Maruyama, "High-Precision Selective Deposition of Catalyst for Facile Localized Growth of Single-Walled Carbon Nanotubes," *Journal of the American Chemical Society*, vol. 131, pp. 10344-10345, 2009.
- [70] Rayleigh, "Breath Figures," *Nature*, vol. 86, pp. 416-417, 1911.
- [71] D. Beysens and C. M. Knobler, "Growth of Breath Figures," *Physical Review Letters*, vol. 57, pp. 1433-1436, 1986.
- [72] J. Blaschke, T. Lapp, B. Hof, and J. Vollmer, "Breath Figures: Nucleation, Growth, Coalescence, and the Size Distribution of Droplets," *Physical Review Letters*, vol. 109, p. 068701, 2012.
- [73] H. Gau and S. Herminghaus, "Ripening of Ordered Breath Figures," *Physical Review Letters*, vol. 84, pp. 4156-4159, 2000.
- [74] A. Boker, Y. Lin, K. Chiapperini, R. Horowitz, M. Thompson, V. Carreon, T. Xu, C. Abetz, H. Skaff, A. D. Dinsmore, T. Emrick, and T. P. Russell, "Hierarchical nanoparticle assemblies formed by decorating breath figures," *Nature Materials*, vol. 3, pp. 302-306, 2004.
- [75] H. Bai, C. Du, A. Zhang, and L. Li, "Breath Figure Arrays: Unconventional Fabrications, Functionalizations, and Applications," *Angewandte Chemie International Edition*, vol. 52, pp. 12240-12255, 2013.
- [76] M. Hernandez-Guerrero and M. H. Stenzel, "Honeycomb structured polymer films via breath figures," *Polymer Chemistry*, vol. 3, pp. 563-577, 2012.
- [77] W. Zhou, J. Vavro, N. M. Nemes, J. E. Fischer, F. Borondics, K. Kamarás, and D. B. Tanner, "Charge transfer and Fermi level shift in p-doped single-walled carbon nanotubes," *Physical Review B*, vol. 71, p. 205423, 2005.
- [78] H. Shimotani, S. Tsuda, H. Yuan, Y. Yomogida, R. Moriya, T. Takenobu, K. Yanagi, and Y. Iwasa, "Continuous Band-Filling Control and One-Dimensional Transport in Metallic and Semiconducting Carbon Nanotube Tangled Films," *Advanced Functional Materials*, vol. 24, pp. 3305-3311, 2014.
- [79] M. S. Arnold, A. A. Green, J. F. Hulvat, S. I. Stupp, and M. C. Hersam, "Sorting carbon nanotubes by electronic structure using density differentiation," *Nature Nanotechnology*, vol. 1, pp. 60-65, 2006.
- [80] S. H. Jin, S. N. Dunham, J. Song, X. Xie, J.-h. Kim, C. Lu, A. Islam, F. Du, J. Kim, J. Felts, Y. Li, F. Xiong, M. A. Wahab, M. Menon, E. Cho, K. L. Grosse, D. J. Lee, H. U. Chung, E. Pop, M. A. Alam, W. P. King, Y. Huang, and J. A. Rogers, "Using nanoscale thermocapillary flows to create arrays of purely semiconducting single-walled carbon nanotubes," *Nature*

- Nanotechnology*, vol. 8, pp. 347-355, 2013.
- [81] M. C. Hersam, "Progress towards monodisperse single-walled carbon nanotubes," *Nature Nanotechnology*, vol. 3, pp. 387-394, 2008.
- [82] H. Liu, T. Tanaka, Y. Urabe, and H. Kataura, "High-Efficiency Single-Chirality Separation of Carbon Nanotubes Using Temperature-Controlled Gel Chromatography," *Nano Letters*, vol. 13, pp. 1996-2003, 2013.
- [83] H. Liu, D. Nishide, T. Tanaka, and H. Kataura, "Large-scale single-chirality separation of single-wall carbon nanotubes by simple gel chromatography," *Nature Communication*, vol. 2, p. 309, 2011.
- [84] H. Dai, A. G. Rinzler, P. Nikolaev, A. Thess, D. T. Colbert, and R. E. Smalley, "Single-wall nanotubes produced by metal-catalyzed disproportionation of carbon monoxide," *Chemical Physics Letters*, vol. 260, pp. 471-475, 1996.
- [85] Y. Miyauchi, S. Chiashi, Y. Murakami, Y. Hayashida, and S. Maruyama, "Fluorescence spectroscopy of single-walled carbon nanotubes synthesized from alcohol," *Chemical Physics Letters*, vol. 387, pp. 198-203, 2004.
- [86] M. He, A. I. Chernov, E. D. Obraztsova, H. Jiang, E. I. Kauppinen, and J. Lehtonen, "Synergistic effects in FeCu bimetallic catalyst for low temperature growth of single-walled carbon nanotubes," *Carbon*, vol. 52, pp. 590-594, 2013.
- [87] M. He, B. Liu, A. I. Chernov, E. D. Obraztsova, I. Kauppi, H. Jiang, I. Anoshkin, F. Cavalca, T. W. Hansen, J. B. Wagner, A. G. Nasibulin, E. I. Kauppinen, J. Linnekoski, M. Niemelä, and J. Lehtonen, "Growth Mechanism of Single-Walled Carbon Nanotubes on Iron–Copper Catalyst and Chirality Studies by Electron Diffraction," *Chemistry of Materials*, vol. 24, pp. 1796-1801, 2012.
- [88] M. He, A. I. Chernov, P. V. Fedotov, E. D. Obraztsova, J. Sainio, E. Rikkinen, H. Jiang, Z. Zhu, Y. Tian, E. I. Kauppinen, M. Niemelä, and A. O. I. Krause, "Predominant (6,5) Single-Walled Carbon Nanotube Growth on a Copper-Promoted Iron Catalyst," *Journal of the American Chemical Society*, vol. 132, pp. 13994-13996, 2010.
- [89] S. Lim, D. Ciuparu, C. Pak, F. Dobek, Y. Chen, D. Harding, L. Pfefferle, and G. Haller, "Synthesis and Characterization of Highly Ordered Co–MCM-41 for Production of Aligned Single Walled Carbon Nanotubes (SWNT)," *The Journal of Physical Chemistry B*, vol. 107, pp. 11048-11056, 2003.
- [90] S. Fan, M. G. Chapline, N. R. Franklin, T. W. Tombler, A. M. Cassell, and H. Dai, "Self-Oriented Regular Arrays of Carbon Nanotubes and Their Field Emission Properties," *Science*, vol. 283, pp. 512-514, 1999.
- [91] L. Huang, S. J. Wind, and S. P. O'Brien, "Controlled Growth of Single-Walled Carbon Nanotubes from an Ordered Mesoporous Silica Template," *Nano Letters*, vol. 3, pp. 299-303, 2003.

## Bibliography

---

- [92] D. Ciuparu, Y. Chen, S. Lim, G. L. Haller, and L. Pfefferle, "Uniform-Diameter Single-Walled Carbon Nanotubes Catalytically Grown in Cobalt-Incorporated MCM-41," *The Journal of Physical Chemistry B*, vol. 108, pp. 503-507, 2003.
- [93] P. Ramesh, N. Kishi, T. Sugai, and H. Shinohara, "High-Yield Synthesis of Single-Wall Carbon Nanotubes on MCM41 Using Catalytic Chemical Vapor Deposition of Acetylene," *The Journal of Physical Chemistry B*, vol. 110, pp. 130-135, 2005.
- [94] S. M. Bachilo, L. Balzano, J. E. Herrera, F. Pompeo, D. E. Resasco, and R. B. Weisman, "Narrow (n,m)-Distribution of Single-Walled Carbon Nanotubes Grown Using a Solid Supported Catalyst," *Journal of the American Chemical Society*, vol. 125, pp. 11186-11187, 2003.
- [95] Z. Li, Y. Jia, J. Wei, K. Wang, Q. Shu, X. Gui, H. Zhu, A. Cao, and D. Wu, "Large area, highly transparent carbon nanotube spiderwebs for energy harvesting," *Journal of Materials Chemistry*, vol. 20, pp. 7236-7240, 2010.
- [96] J. Li, K. Liu, S. Liang, W. Zhou, M. Pierce, F. Wang, L. Peng, and J. Liu, "Growth of High-Density-Aligned and Semiconducting-Enriched Single-Walled Carbon Nanotubes: Decoupling the Conflict between Density and Selectivity," *ACS Nano*, vol. 8, pp. 554-562, 2013.
- [97] S. Huang, X. Cai, and J. Liu, "Growth of Millimeter-Long and Horizontally Aligned Single-Walled Carbon Nanotubes on Flat Substrates," *Journal of the American Chemical Society*, vol. 125, pp. 5636-5637, 2003.
- [98] D. Yuan, L. Ding, H. Chu, Y. Feng, T. P. McNicholas, and J. Liu, "Horizontally Aligned Single-Walled Carbon Nanotube on Quartz from a Large Variety of Metal Catalysts," *Nano Letters*, vol. 8, pp. 2576-2579, 2008.
- [99] Q. Cao, S.-j. Han, G. S. Tulevski, Y. Zhu, D. D. Lu, and W. Haensch, "Arrays of single-walled carbon nanotubes with full surface coverage for high-performance electronics," *Nature Nanotechnology*, vol. 8, pp. 180-186, 2013.
- [100] K. Hata, D. N. Futaba, K. Mizuno, T. Namai, M. Yumura, and S. Iijima, "Water-Assisted Highly Efficient Synthesis of Impurity-Free Single-Walled Carbon Nanotubes," *Science*, vol. 306, pp. 1362-1364, 2004.
- [101] G. D. Nessim, A. J. Hart, J. S. Kim, D. Acquaviva, J. Oh, C. D. Morgan, M. Seita, J. S. Leib, and C. V. Thompson, "Tuning of Vertically-Aligned Carbon Nanotube Diameter and Areal Density through Catalyst Pre-Treatment," *Nano Letters*, vol. 8, pp. 3587-3593, 2008.
- [102] T. Thurakitseree, C. Kramberger, A. Kumamoto, S. Chiashi, E. Einarsson, and S. Maruyama, "Reversible Diameter Modulation of Single-Walled Carbon Nanotubes by Acetonitrile-Containing Feedstock," *ACS Nano*, vol. 7, pp. 2205-2211, 2013.
- [103] W. Zhou, Z. Han, J. Wang, Y. Zhang, Z. Jin, X. Sun, Y. Zhang, C. Yan, and Y. Li, "Copper Catalyzing Growth of Single-Walled Carbon Nanotubes on Substrates," *Nano Letters*, vol. 6, pp. 2987-2990, 2006.



## Bibliography

---

- [104] D. Takagi, Y. Homma, H. Hibino, S. Suzuki, and Y. Kobayashi, "Single-Walled Carbon Nanotube Growth from Highly Activated Metal Nanoparticles," *Nano Letters*, vol. 6, pp. 2642-2645, 2006.
- [105] D. Takagi, H. Hibino, S. Suzuki, Y. Kobayashi, and Y. Homma, "Carbon Nanotube Growth from Semiconductor Nanoparticles," *Nano Letters*, vol. 7, pp. 2272-2275, 2007.
- [106] B. Liu, W. Ren, L. Gao, S. Li, S. Pei, C. Liu, C. Jiang, and H.-M. Cheng, "Metal-Catalyst-Free Growth of Single-Walled Carbon Nanotubes," *Journal of the American Chemical Society*, vol. 131, pp. 2082-2083, 2009.
- [107] S. Huang, Q. Cai, J. Chen, Y. Qian, and L. Zhang, "Metal-Catalyst-Free Growth of Single-Walled Carbon Nanotubes on Substrates," *Journal of the American Chemical Society*, vol. 131, pp. 2094-2095, 2009.
- [108] D. Takagi, Y. Kobayashi, and Y. Homma, "Carbon Nanotube Growth from Diamond," *Journal of the American Chemical Society*, vol. 131, pp. 6922-6923, 2009.
- [109] L. Ding, A. Tselev, J. Wang, D. Yuan, H. Chu, T. P. McNicholas, Y. Li, and J. Liu, "Selective Growth of Well-Aligned Semiconducting Single-Walled Carbon Nanotubes," *Nano Letters*, vol. 9, pp. 800-805, 2009.
- [110] T. P. McNicholas, L. Ding, D. Yuan, and J. Liu, "Density Enhancement of Aligned Single-Walled Carbon Nanotube Thin Films on Quartz Substrates by Sulfur-Assisted Synthesis," *Nano Letters*, vol. 9, pp. 3646-3650, 2009.
- [111] Y. Shibuta and S. Maruyama, "Molecular dynamics simulation of formation process of single-walled carbon nanotubes by CCVD method," *Chemical Physics Letters*, vol. 382, pp. 381-386, 2003.
- [112] F. Yang, X. Wang, D. Zhang, J. Yang, LuoDa, Z. Xu, J. Wei, J.-Q. Wang, Z. Xu, F. Peng, X. Li, R. Li, Y. Li, M. Li, X. Bai, F. Ding, and Y. Li, "Chirality-specific growth of single-walled carbon nanotubes on solid alloy catalysts," *Nature*, vol. 510, pp. 522-524, 2014.
- [113] M. Milnera, J. Kürti, M. Hulman, and H. Kuzmany, "Periodic Resonance Excitation and Intertube Interaction from Quasicontinuous Distributed Helicities in Single-Wall Carbon Nanotubes," *Physical Review Letters*, vol. 84, pp. 1324-1327, 2000.



# Acknowledgement

The story of this Thesis starts from the winter of 2010 when Professor Maruyama replied ‘okey’ to my email asking to join his lab as a doctoral student. At that time, I knew nothing about carbon nanotubes but was incredibly amazed by the power of ‘nano’ through my research during the master’s degree. Now I am going to receive my doctoral degree because of carbon nanotube research. There is no doubt to whom I am most grateful. Maruyama sensei has taught me many things, among which the most important to me is the sense of a scientist. He also supported me a lot by always encouraging me, and introduced me into the community of carbon nanotube research.

I am also very grateful to all the members of Maruyama Laboratory. Chiashi-sensei is always helpful and very insightful on spectroscopy. Xiang Rong-sensei came just before I had my preliminary defense, but he gave me many insightful ideas. Dr. Erik Einarsson, Dr. Pei Zhao and Dr. Theerapol Thurakitserree were experienced researchers when I just came to the lab. We used to do experiments together, hang out together and discuss about everything together, through which I learned a lot from them. Inoue-san and Chiba-kun helped me a lot with many experiments. I also appreciate the support from Technician Watanabe-san, Secretaries Terao-san and Shimada-san.

I would like to thank my collaborators, Prof. Esko Kauppinen, Dr. Albert Nasibulin from Aalto University for providing excellent SWNT samples; Dr. Hiromichi Kataura and Dr. Shunji Fujii from AIST for the measurement of IPCE; Prof. Jun Kono and Xiaowei He for the discussion of OPA although it is still ongoing and not shown in this Thesis. I want to thank many researchers for helpful discussion, Prof. Kazunari Matsuda and Feijiu Wang from Kyoto University as well as Prof. Anyuan Cao and Enzheng Shi from Peking University, who are doing similar research; Prof. Riichiro Saito from Tohoku University for the discussion of

Raman; Prof. A. John Hart from MIT for the discussion of nanotube architecture; and Dr. Miao Zhong from Domen Lab at Chemical Engineering Department and Dr. Wang from RCAST at this University for the discussion of solar energy harvesting.

Last but definitely not the least, I want to thank my wife, Zhequn, who is also a doctoral student in this department. We have been through many tough days working and discussing together until late night. We share the joy of each other. I also want to thank my parents for their endless support and love.

# Curriculum Vitae

## Education Background

### October 2011-present

Ph. D. candidate, Mechanical Engineering, The University of Tokyo, Japan

Thesis: *CVD Growth Control and Solar Cell Applications of Single-Walled Carbon Nanotubes*

Advisor: Prof. Shigeo Maruyama

### September 2008 – July 2011

Master of Engineering, Engineering Thermophysics, Shandong University, China

Thesis: *Design, Synthesis and Characterization of Sintered Ni-Cu Porous Wicks for Loop Heat Pipes*

Advisor: Chang Jiang Distinguished Prof. Lin Cheng and Associate Prof. Gongming Xin

### September 2004 – July 2008

Bachelor of Engineering, Thermal Energy Engineering, Shandong University, China

## Honors and Awards

Year	Award	Organization
2014	Young Scientist Award	Fullerene, Nanotube and Graphene Society of Japan
2013	Best Poster Award	A3 Symposium of Nanomaterial for Energy and Electronics

## Professional Experience

### October, 2011 – present

Research Assistant, Global Center of Excellence for Mechanical System Innovation (GMSI Program), The University of Tokyo, Japan

### October, 2012 – February, 2013

Teaching Assistant, Global Center of Innovation in Engineering Education (GCIEE), Graduate School of Engineering, The University of Tokyo, Japan